Isothermal Fatigue, Damage Accumulation, and Life Prediction of a Woven PMC

Andrew L. Gyekenyesi
Cleveland State University, Cleveland, Ohio

National Aeronautics and
Space Administration

Lewis Research Center

March 1998

Acknowledgments

Available from

NASA Center for Aerospace Information	National Technical Information Service
800 Elkridge Landing Road	5287 Port Royal Road
Linthicum Heights, MD 21090-2934	Springfield, VA 22100
Price Code: A08	Price Code: A08

ISOTHERMAL FATIGUE, DAMAGE ACCUMULATION, AND LIFE PREDICTION OF A WOVEN PMC

ANDREW L. GYEKENYESI

ABSTRACT

This dissertation focuses on the characterization of the fully reversed fatigue behavior exhibited by a carbon fiber/polyimide resin, woven laminate at room and elevated temperatures. Nondestructive video edge view microscopy and destructive sectioning techniques were used to study the microscopic damage mechanisms that evolved. The elastic stiffness was monitored and recorded throughout the fatigue life of the coupon and later utilized as a damage variable for a phenomenological model. In addition, residual compressive strength tests were conducted on fatigue coupons with various degrees of damage as quantified by stiffness reduction. Experimental results indicated that the monotonic tensile properties were only minimally influenced by temperature, while the monotonic compressive and fully reversed fatigue properties displayed noticeable reductions due to the elevated temperature. The stiffness degradation, as a function of cycles, consisted of three stages; a short-lived high degradation period, a constant degradation rate segment composing the majority of life, and a final stage demonstrating an increasing rate of degradation up to failure. Concerning the residual compressive strength tests at room and elevated temperatures, the

elevated temperature coupons appeared much more sensitive to damage. At elevated temperatures, coupons experienced a much larger loss in compressive strength when compared to room temperature coupons with equivalent damage.

The fatigue damage accumulation law proposed for the model incorporates a scalar representation for damage, but admits a multiaxial, anisotropic evolutionary law. The model predicts the current damage (as quantified by current stiffness) and remnant life of a composite that has undergone a known load at temperature. The damage/life model is dependent on the applied multiaxial stress state and temperature. Comparisons between the damage/life model and data showed good predictive capabilities concerning stiffness degradation and cycles to failure. However, the data generated represents uniaxial loading applied at isothermal temperatures. Thus, a uniaxial formulation of the fatigue life model proposed in this study was characterized. Future work should encompass multiaxial testing and examine issues relating to thermomechanical fatigue in order to enhance the modeling effort presented here.

TABLE OF CONTENTS

LIST OF TABLES

LIST OF FIGURES

CHAPTER I

POLYMER MATRIX COMPOSITES

1.1 Introduction

At the present time polymer matrix composites (PMCs) are commonly utilized by design engineers in a wide variety of applications. These composites, when fabricated using continuous fibers in a two-dimensional form, can be loosely categorized as either a non-woven tape system, or as a woven system. Fiber reinforced laminated PMCs are supplanting conventional materials due to their improved fatigue resistance, high specific strength, and high specific stiffness. These multi-layered filamentary composites have replaced conventional superalloys in aerospace applications, deep submergence vessels, radomes, sporting goods, and other structures where their unique properties impart a commercial and/or structural advantage. Adopting a wide perspective and overviewing the market for PMCs in general, the unique flexibility of tailoring the material to effectively resist applied loads in an efficient manner (not to mention the enhanced mechanical properties associated with PMCs) has steadily increased the rate of utilization for this material group.

Current objectives common to the aerospace community call for advanced aircraft that produce greater payload delivery and increases in fuel efficiency. Of vital importance in the development of the propulsion systems for these aircraft is the utilization of cost effective materials. Bowles et al. (1996) pointed out that one of the prevailing philosophies driving

these programs is the utilization of lightweight PMCs in the hot sections of newer engines where elevated temperatures prevail. These materials will serve both as load bearing and non-load bearing components. Anticipated service environments include temperature regimes that reach and maintain levels of 300 °C (572 °F) or more. These future requirements impose service temperatures approaching the glass transition temperature (T_G) of the resin. Whether the anticipated service requirements are stringent (e.g., aerospace) or mundane (where commercial success is driving technology) a data base of pertinent engineering properties must be developed for legal and technical reasons. Therefore, one of the objectives of this dissertation is to add to the existing property data base by providing data relative to fatigue and damage accumulation. This data has been obtained under conditions approaching the service conditions found in turbine engines.

For PMC systems the reinforcing fibers serve as the primary load carrying component. The matrix provides structural integrity by serving as a load transfer medium. In addition, the matrix provides a certain amount of rigidity, and protects the fibers from exposure to unfavorable environments. The traditional, non-woven laminated composite systems are fabricated by stacking plies of unidirectional tapes. Stacking the individual plies at various orientations imparts a directional dependence to the strength and stiffness of the material which can be used advantageously by the design engineer. At present, most non-woven carbon fiber-reinforced polymer resin laminates are made from unidirectional, pre-impregnated sheets (i.e., prepregs). However, the composite industry has been expanding its use of planar (2-D) cloth plies in laminates. Curtis and Bishop (1984) indicated early on that increased use of cloth laminates is clearly tied to advances in the manufacturing quality of woven carbon fiber cloth. In a subsequent paper Curtis and Moore (1985) outlined the advantages associated with textile preforms. Today, steady improvement in weaving technology has increased the availability of a multitude of textile preforms. Advantages associated with textile preforms include ease of handling, the ability of the fabric to conform to complex shapes, improved residual strength after impact, and the fact that the fabric has more

isotropic in-plane properties relative to non-woven lay-ups. Fabrics reduce the cost of production by allowing for less labor intensive production methods, such as the resin transfer molding (RTM) process. Many types of two-dimensional woven plies are available. Plain, twill, and satin planar weaves are depicted in Figure 1.1.

With the increasing utilization of PMCs in structural components the need to predict service life under both static and cyclic loads becomes important for successful commercialization. However, to predict life the design engineer must be able to detect the accumulated damage that occurs in a structural component under various service conditions. Once a dependable methodology has been established to detect damage, the design engineer must also be able to ascertain the effect damage has on engineering properties. This need essentially leads to establishing a damage criterion. The damage criterion dictates when to remove a component from service.

In the past, successful fatigue life models for conventional materials would incorporate a relationship between microstructural damage (i.e., the defect state) and the mechanical properties of the materials. Similar models based on high quality fatigue data must be established for PMCs. Models that predict the rate of damage accumulation for PMCs would enhance the ability of a design engineer to predict when a component should be removed from service.

However, in order to construct a useful fatigue life model for PMC laminates constructed from either tapes, weaves or both, an extensive data base must be developed. While information relative to non-woven laminated PMCs has been added to the data base for a number of years, little effort has been invested augmenting the data base for woven PMCs. This dissertation expands the data base of information regarding the fatigue life of a cross-woven PMC. The macroscopic and microscopic behavior of the material was documented at room and elevated temperatures under a fully reversed cyclic load. To accomplish this, advanced experimental techniques were developed and employed for the uniaxial tests. Finally, an isothermal, multiaxial fatigue life model was proposed that captures the reduction
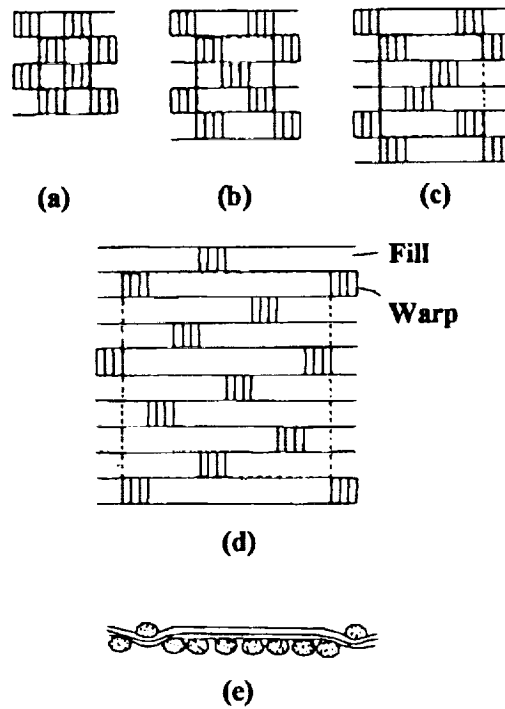
Figure 1.1 Woven 2-D fabrics with various n_g values, (a) $n_g = 2$, plain weave, (b) $n_g = 3$, twill weave, (c) $n_g = 4$, 4-harness (crow foot) satin, (d) $n_g = 8$, 8-harness satin, (e) cross-sectional view (Ishikawa and Chou (1982)).

of stiffness under cyclic load for the aforementioned (0/90) weave. It should be noted that the primary objective of this dissertation was to develop and establish a comprehensive fatigue model for PMCs that correlates well with experimental fatigue data. The following section reviews the typical damage induced in laminated and woven PMCs. The next section contains a discussion regarding damage variables and their relevance. Following this section a review of existing fatigue life models is presented. This chapter concludes with a clear statement of the technical objectives and an overview of the remaining chapters of this dissertation.

1.2 Characterizing Fatigue Damage and Failure Associated with Cyclic Load History

Fatigue failures for conventional engineering materials can be viewed as a two step process: crack initiation followed by crack propagation. Here the majority of the fatigue life is consumed initiating a dominant crack. Once a dominant crack has been initiated, principles of fracture mechanics are utilized to predict crack growth and remnant life. For critical applications where safety issues are paramount (e.g., aeronautics applications) this engineering design approach demands an inspection protocol that employs nondestructive evaluation (NDE) techniques. Crack growth equations are subsequently used to predict the point in time when the detectable crack becomes unstable and propagates catastrophically. Broek (1986) pointed out that in less demanding applications, design engineers simply assume the presence of the smallest flaw that can be detected by NDE techniques, and thus bypass in-situ testing which can become expensive.

Unlike fatigue failure in conventional engineering materials, the accumulation and progression of damage in composite materials are relatively complex. In addition, the basic damage mechanisms encountered in composite laminates are more numerous than conventional materials. For the case of non-woven laminates, Talreja (1987) pointed out that these mechanisms include fiber-matrix debonding (interface failure), matrix cracking that can be intralaminar or interlaminar (delamination), and fiber fracture or fiber micro-buckling. These

mechanisms are depicted graphically in Figure 1.2. The sequence of crack initiation and propagation for these mechanisms is well documented by various authors for tape lay-ups fabricated from a sequential stacking of 0° plies and various off-axis plies. The reader is referred to the early work of Hahn and Lorenzo (1986) as well as Highsmith (1984) on this topic. The reader can also consult texts authored/edited by Reifsnider (1991), Agarwal and Broutman (1990), and Talreja (1987). It should be noted that the vast majority of these data have been acquired from load and strain controlled uniaxial tensile fatigue experiments conducted under ambient conditions. Therefore, a need exists for studying these damage events under various environmental conditions paralleling those of the component.

Fujii and Amijima (1993) as well as Schulte (1986) showed similar damage events to occur in woven laminates. In summary, the events include transverse cracks located in the fill tows (also called weft tows) and resin rich areas, longitudinal cracks in the load bearing warp tows, and bundle debonds and interlaminar delaminations. Note, each tow/bundle consists of thousands of individual fibers. A schematic of the woven damage is shown in Figure 1.3. Further details concerning the sequence for the individual events are given below for both non-woven and woven laminates.

In the process of conducting a detailed review of the fatigue data cited earlier for non-woven laminated PMCs revealed several noteworthy points. First, for tension-tension fatigue tests ($R_\sigma = \sigma_{min} / \sigma_{max}$: $0 < R_\sigma < 1$; see Figure 1.4) the first damage event to occur is matrix cracking in the angled plies. These cracks form through the thickness of the ply in a direction parallel to the fibers, and perpendicular to the laminate face. Typically, matrix cracks are initiated at fiber debonds or at flaws introduced during fabrication. Next, longitudinal cracks appear in the 0° ply oriented parallel to the load direction. Jamison (1986) pointed out that these cracks are caused by the Poisson's mismatch between plies with different orientations, and are probably initiated at fiber breaks in the 0° ply. Delaminations occur at the crossing points of the transverse and longitudinal cracks, along with intersections of the transverse cracks and the free-edge. Throughout the life of the test
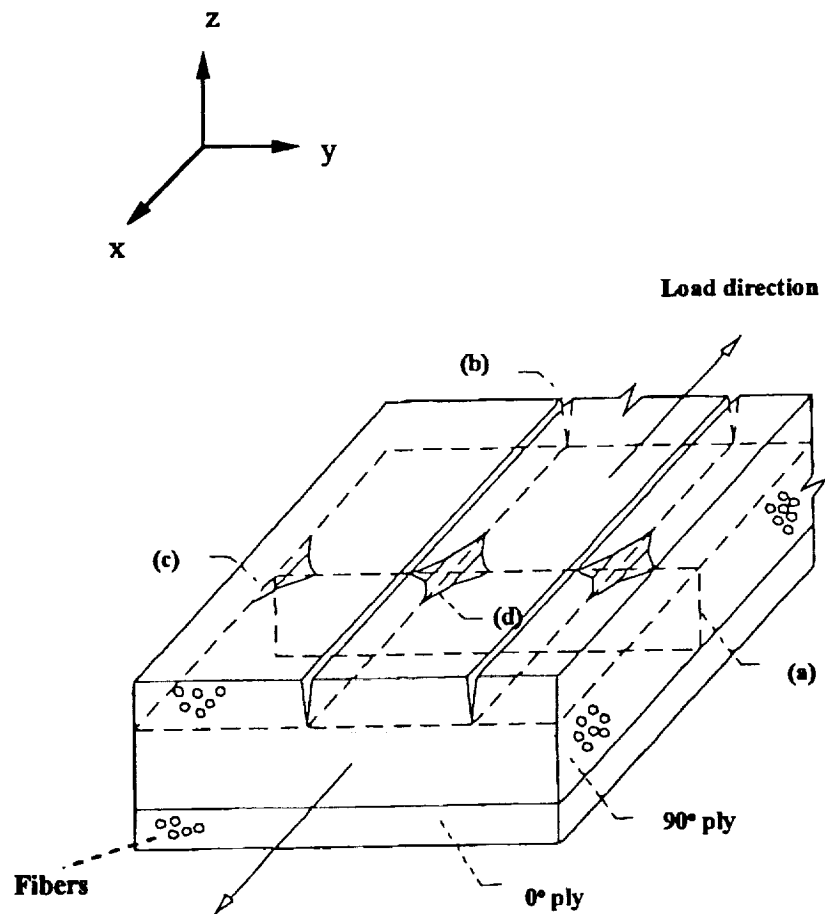
Figure 1.2 Matrix dominated cracking events. (a) Transverse crack, (b) Longitudinal splitting, (c) Free-edge 0/90 delamination, (d) 0/90 delamination induced by crossing cracks.
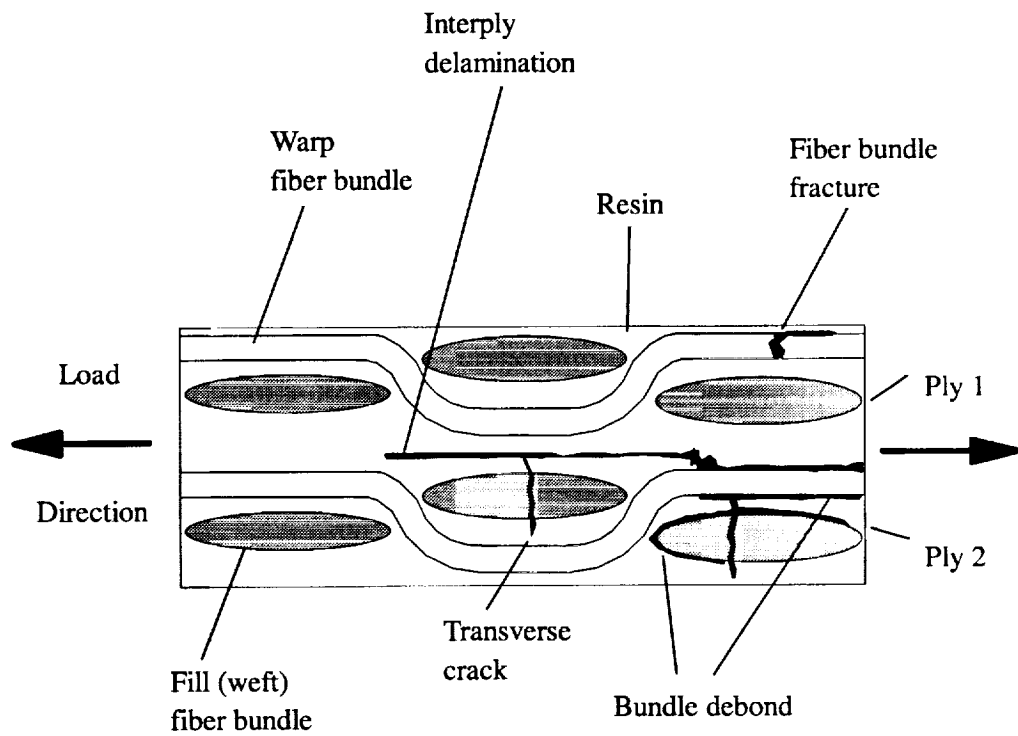
Figure 1.3 Illustration of fatigue damage in a (0/90) weave: Edge -view.
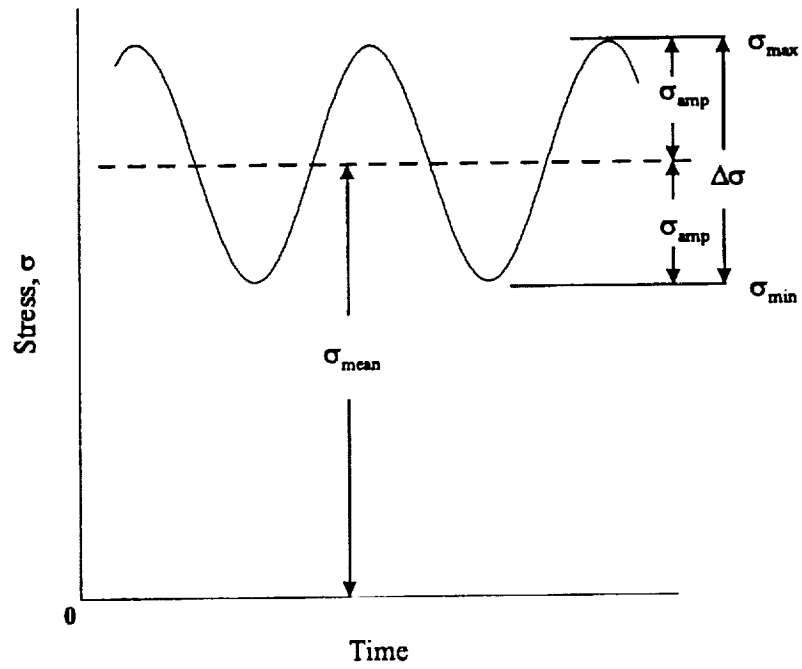
Figure 1.4 Schematic representation of stress/time relationship for load controlled fatigue.

specimen, fiber fractures transpire at random locations in the load bearing 0° plies. Accumulation of stress concentrations and stress redistributions due to the various matrix cracks increases the number of fiber breaks in the material. When the material becomes saturated with fiber breaks in the primary load bearing 0° plies, the laminate fails.

In load-controlled, uniaxial tension-compression fatigue experiments ($R_\sigma < 0$), the failure sequence is similar to the sequence described above, but the accumulating damage is more severe. This is due to the synergistic effects of damage induced during both the tensile and compressive regimes of the load cycle. The reduction of fatigue life in PMC test specimens subjected to tension-compression load regimes is a result of an additional failure mode (i.e., localized material instabilities) that is not present in a tension-tension load cycle. Schultz and Reifsnider (1984), Adam et al. (1991), Ryder and Walker (1979), Carlson and Kardomateas (1996), as well as Rotem and Nelson (1989) have discussed this issue. Under tension-compression load cycles transverse and longitudinal matrix cracks develop first, and the matrix cracks are followed by delaminations. As these delaminations successively multiply, damage will accumulate during the compression segment of each load cycle because individual plies lose the bracing provided by adjacent layers. This bracing by adjacent layers tends to mitigate buckling and/or shear failure. When the material is saturated with delaminations the test specimen fails in compression due to ply buckling, fiber micro-buckling in the intact laminas, and/or out-of-plane failure of the resin.

Schulte (1986) and Bishop (1989) showed that the 2-D woven laminates closely parallel the tension-tension and tension-compression fatigue damage sequences of the well documented non-woven laminates. Transverse cracks initiate and propagate inside the fill (weft) tows and resin rich areas between the bundles as seen in Figure 1.3. These cracks originate in the undulated region where a fill tow encircles a warp tow. The cracks are a result of the lower material stiffness in the region where the cracks originate in comparison to the surrounding regions with straightened bundles. Schulte (1986) proposed that this lower stiffness causes a local softening and as a result the maximum strain occurs at the center of the

undulation where transverse cracks are started. Next, longitudinal cracks develop along the load bearing warp bundles. These cracks are initiated by similar mechanisms found in non-woven cross-ply laminates. The resin material and the warp bundles attempt to contract in the transverse direction due to the Poisson's effect, but are constricted by the transverse fill fibers. Finally, debonds along the axial and transverse bundles initiate both at the free edge and at undulation points in the interior of a laminate. Burr and Morris (1994), Shulte et al. (1987) as well as Bishop (1989) cited experimental evidence that as debonds grow, they coalesce into interlaminar delaminations. These interior interlaminar events are initiated at undulation points containing transverse and longitudinal cracks that cross one another. As was the case for the non-woven laminates, delaminations cause the specimen to fail in compression.

As a final note, the undulation points cause woven laminates to show a slight decrease in stiffness properties and fatigue life when compared to tapes with similar lay-ups. Early work by Weinberger et al. (1977) on carbon fiber reinforced polymers showed that 2-D weaves with less fiber distortion such as an 8-satin weave result in smaller reductions in mechanical properties.

1.3 Fatigue Damage Variables

Up to this point the discussion has for the most part focused on the microscopic damage events which occur throughout life and ultimately lead to failure. These events cause a degradation of the mechanical properties long before catastrophic failure. Usually catastrophic failure is not the design engineer's only concern since the cumulative effect on important design properties such as stiffness eventually becomes detrimental to the functionality of the component. The presence of fatigue induced defects can accelerate corrosion, can cause leakage in containment vessels, and may, as indicated above, alter the behavior of the elastically tailored structure. O'Brien (1978) discussed how stiffness changes on the order of 10 percent can significantly alter the aerodynamic response of

a wing assembly making it unacceptable for service even though the assembly had not "failed" by conventional failure/fracture criteria.

Some studies and conferences have been conducted documenting the effects of various environments (i.e., moisture and temperature) on the static and dynamic behavior of PMCs. The reader is directed to overviews by Harris and Gates (1993), Vinson (1977), and Springer (1981). The majority of the information in these references is concerned with the effects of environment on variables such as ultimate static strength and fatigue life. Availability of data related to the specifics of damage evolution (microscopic damage initiation and growth as well as its influence on macroscopic properties) as a function of environment is extremely limited and in need of supplementation.

The current experimental evidence indicates that environmental degradation is most severe in the resin. Hence, strength properties that display a high dependence on the resin integrity need to be tracked carefully when laminates are exposed to detrimental service conditions. Ryder and Walker (1979) as well as Hahn (1982) pointed out that the sense of the applied load is important. Elevated temperatures cause a noticeable decrease in static strength and fatigue life for test specimens subjected to compressive load regimes. However, temperature has a minimal effect on strength and life for test specimens subjected to uniaxial tension. This is due to the fact that tensile properties are fiber dominated, while for compression load regimes the resin plays a much more significant role. Careful consideration must be given to the more general case where components are subjected to tension/compression cyclic loads. To further complicate the issue of damage accumulation, the sequence of initiation and propagation of the various cracks is a function of laminate lay-up, stacking sequence, structural geometry, and loading conditions. Thus damage accumulation is load path dependent and material dependent. In this sense damage can be considered a material state variable from the standpoint of engineering mechanics.

Quantifiable engineering properties such as stiffness and residual strength can be indicators of the current damage state in a composite material system. Studies by Yang (1978),

Yang and Liu (1977), Reifsnider (1986) as well as Tai et al. (1995) have shown that residual strength in composite materials degrades during fatigue experiments. Similar studies by O'Brien (1978), Odom and Adams (1982), as well as Stinchcomb and Bakis (1991) have demonstrated that stiffness degrades as well. However, both properties can show a temporary increase under certain conditions. For example, misaligned fibers in non-woven laminates can straighten out under tensile loads. Gyekenyesi et al. (1995) also pointed out that a reduction in fiber undulation can be achieved under tensile loads in woven laminates. Both of these phenomenon can increase the longitudinal modulus during the initial stages of a fatigue experiment. Stinchcomb and Bakis (1991) have indicated that matrix damage adjacent to holes or notches helps to relax stress concentrations. This mechanism tends to increase the residual strength.

Ultimately, as a fatigue specimen approaches failure internal damage mechanisms will reduce both the modulus and residual strength below levels exhibited in the initial stages of cyclic load history. In the case of load controlled fatigue experiments where failure is defined as complete fracture, the residual strength diminishes to equal the maximum applied stress. In the section that follows various methods that utilize the residual strength and stiffness as indicators of the damage state are discussed. The relationships between the damage state and macroscopic laminate behavior are highlighted relative to past modeling efforts.

1.4 Fatigue Models for PMCs

During the past three decades many investigators have addressed issues relating to modeling fatigue life of components fabricated from composite materials. Liu and Lessard (1994) offered an overview of the many models employed by design engineers to predict fatigue damage progression and life in composites. A number of models employ the traditional curve fitting approach to S-N data (plotting maximum applied stress, S, versus cycles to failure, N_f). Predicting life using S-N models limits the design engineer to the load regimes

used to develop the S-N curve. Models based on residual strength degradation and modulus degradation are currently drawing the most interest. These models adopt damage variables based on measurable macroscopic properties. Utilizing quantifiable macroscopic properties, the design engineer can quantitatively monitor damage accumulation and with an appropriate model the design engineer can infer the age or remaining life of a component. In addition, damage accumulation models can be expanded beyond simple unidirectional load regimes. The damage variable can be updated by integrating a multiaxial damage accumulation function from some initial damage state (caused by processing or a prior load history) to an updated state induced by the current service load. Hence, the damage accumulation models (both stiffness degradation and strength degradation models) can predict life for multi-step, multi-dimensional load regimes. Furthermore, the damage variable can be modified by factors other than applied cyclic load. Enough flexibility exists in some models to capture time dependent effects such as creep and/or environmental effects. Damage accumulation models have the potential to achieve a generalized form which can be extrapolated to conditions beyond those employed in laboratory experiments.

The residual strength degradation theories assume that the rate of degradation due to cyclic damage accumulation is a decreasing function of accumulated cycles. As was mentioned earlier, failure occurs when the current residual strength of the composite matches the maximum applied stress. Broutman and Sahu (1972) proposed a cumulative damage theory using a linear strength degradation expression. Hahn and Kim (1975) introduced a nonlinear residual strength degradation model predicated on the assumption that the slope of the residual strength is inversely proportional to a power law of the current residual strength. This nonlinear degradation model was further investigated by Yang and Liu (1977). These authors proposed a reliability model for the fatigue life of composite materials where the design engineer computes the probability of failure associated with a given number of applied cycles. An advanced, residual strength degradation model which predicts fatigue life for multi-stress levels was proposed by Reifsnider and Stinchcomb (1986). This model

is based on the assumption that the residual strength degradation rate is a power function of fatigue cycles. However, the measurement of residual strength during damage development in a specimen is somewhat impractical since only one measurement can be made per specimen. Lee (1988) pointed out that it is also difficult to compare the damage states between two specimens when the damage state is characterized by the current residual strength. Moreover, residual strength degradation is not always uniquely related to the state of physical damage. Chou and Croman (1979) showed this to be the case for the sudden death syndrome, where physical damage (transverse cracks, delaminations, etc.) is continuously occurring but the residual strength is constant until very near to failure when the rate of strength degradation accelerates. Thus the design engineer is cautioned regarding the use of residual strength models to predict the fatigue behavior of an individual component in service.

Modulus degradation theories are based on the observation that under cyclic load, the stiffness of the composite decreases as a function of accumulated cycles. The change in stiffness of a composite laminate as a result of cyclic load is a repeatable characteristic for a given type of material, laminate arrangement, and load spectrum. Changes may take place in multiple stages. Figure 1.5(a), as presented by Schulte (1986), depicts the three stage stiffness behavior of a $(0_2/90_2/0_2/90_2)_s$ graphite epoxy non-woven laminate subjected to tension-tension ($R_\sigma = 0.1$) cyclic loading. Stage I damage is characterized by an initial rapid decrease in stiffness caused by matrix cracking and some early fiber fracture. Stage II damage is a lengthy intermediate period of moderate stiffness reduction which results from additional matrix cracking in off-axis and 0° plies, crack coupling along ply interfaces, and internal delaminations. The onset of Stage III damage near the end of life is characterized by a rapid decrease in stiffness. This is a result of an increase in damage growth rate representative of delamination coalescence and fiber fracture.

A three stage stiffness degradation plot of a cross-weave laminate is depicted in Figure 1.5 (b). The experimental conditions for the figure are the same as for the cross-ply appearing in the same figure. As is the case for non-wovens, transverse cracks dominate the
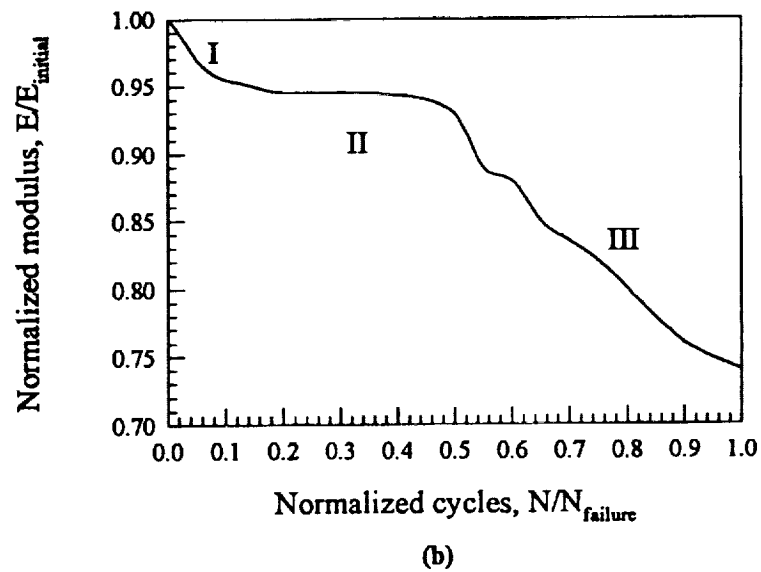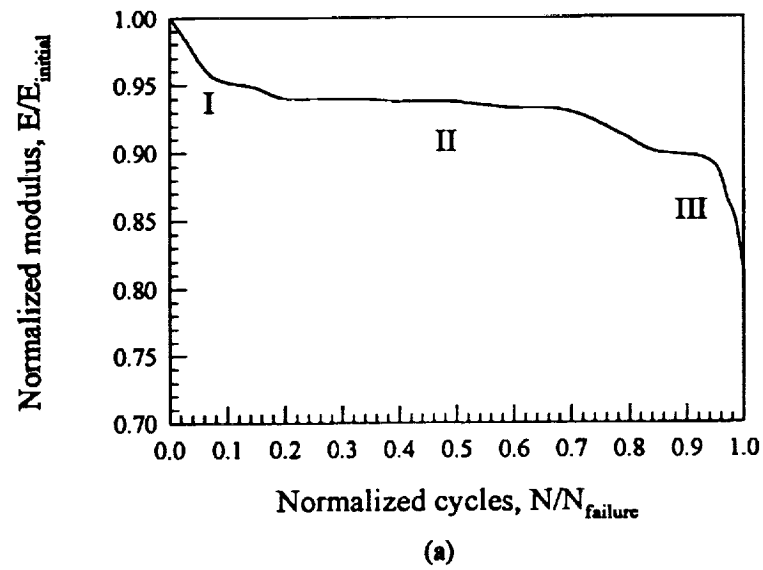
Figure 1.5 (a) Typical three stage stiffness reduction for $(0_2/90_2/0_2/90_2)_s$ carbon/epoxy laminate. (b) Stiffness degradation for a carbon/epoxy 8-harness satin cross-weave (Schulte (1986)).

first stage. Damage during the second stage is dictated by the initiation and growth of longitudinal cracks and bundle debonds. Finally, the transverse and longitudinal cracks and debonded bundles coalescence to initiate interlaminar delaminations which define the start of the third stage leading to failure. Similar multiple stage behavior is also observed when the laminates are subjected to reversed loading.

Numerous studies concerning non-woven laminates have indicated that moduli correlate well with internal matrix damage. For example, efforts by Talreja (1987) and O'Brien (1978) concluded that stiffness loss is a function of matrix crack density and delamination area. The degree of damage associated with crack density can also be obtained from nondestructive inspection of a component. In addition, Wang et al. (1984) and Gyekenyesi (1996) claimed that crack density can be predicted using a mechanistic paradigm such as fracture mechanics coupled with the assumption of a minimum flaw size.

From the design engineer's viewpoint failure using the moduli degradation method can be defined as some critical loss in stiffness as discussed by Ye (1989), Poursartip et al. (1982) and Hahn and Kim (1976). Alternately, the accumulation of strain for the case of load controlled fatigue can be compared to the ultimate static strain established in a monotonic test in order to define failure. This latter definition has been advocated by Hwang and Han (1989) and Yang et al. (1989) and is considered an indirect definition of the modulus degradation criteria. Both definitions yield critical values that are easily obtained from experiments.

Stiffness changes have been documented for a number of PMC systems. Unlike residual strength, stiffness data can be monitored continuously during the life of a single specimen. Meskini (1986) pointed out that stiffness can be obtained nondestructively throughout the load history of a test specimen. Stiffness data can be normalized with respect to initial undamaged stiffness (E/E_o) and plotted versus normalized fatigue life (N/N_f) as shown in Figure 1.5. Ye (1989) demonstrated the repeatability of data for different experimental conditions using this form of data presentation. Stinchcomb and Reifsnider (1979) and Poursartip

et al. (1982) have both shown that the shape of the curve for short life ($N_f < 10^5$) and long life tests ($N_f > 10^5$) is similar. The curves vary little between specimens at different loads when data is depicted as plots of normalized modulus verses normalized cycles to failure. This seems to indicate that damage accumulation has the same basic phenomenological characteristics irrespective of load history for constant environmental conditions. Stinchcomb and Bakis (1991) suggested the use of master curves to extrapolate short-term life data to long-term component performance. Finally, the normalized stiffness approach is an indicator of the "fatigue age" of laminates at various load levels. With a knowledge of the initial material properties and current properties, the normalized stiffness approach allows the engineer to ascertain the current life of a component. The approach also yields a reference damage state for the next load application.

In an actual service application, the modulus degradation approach can be applied to obtain the age of the component if the current stiffness is known. For simple geometries the component can be strain gaged and then subjected to an induced load to obtain the moduli of interest. Golfman (1993) showed the acousto-ultrasonics method of NDE as another possible avenue in the near future. Golfman successfully predicted the elastic constants in a high speed, PMC turbine blade using the technique. Finally, updated moduli values can be achieved by the utilizing a damage mechanics model which is a function of crack density (see Talreja (1987)). The crack damage can be measured by the application NDE methods such as x-ray or acousto-ultrasonics (Hemann et al. (1987)), or by predicting crack damage by employing an analytical model such as one based on fracture mechanics and the strain energy release rate principle (Gyekenyesi (1996)).

The theories and approaches discussed above have to a certain extent shown good agreement with most available fatigue data. However, the vast majority of data produced thus far has been concerned with non-woven laminates subjected to ambient conditions. Further research is needed to study woven laminates and to develop a more definitive relationship between the physical damage (such as matrix cracking and delamination) and the macroscopic

behavior. A thorough understanding of the microscopic damage mechanisms in both wovens and non-wovens generated under various service histories is required before a generalized model can be proposed and utilized with confidence. The goal is developing an analytical model relating stiffness loss to actual damage. Having this tool design engineers will be a step closer to achieving a more generalized paradigm with variables that account for service history, service environment, laminate lay-up, and multiaxial loading.

1.5 Objectives and Scope

This dissertation focuses on the characterization of the monotonic tensile, compressive, and fully reversed fatigue behaviors exhibited by a carbon fiber/polyimide resin, woven laminate at room and elevated temperatures. The monotonic compressive and the fully reversed fatigue tests were conducted utilizing an unsupported specimen design. The 8-harness satin (0/90) weave is the basic building block and critical element for two-dimensional woven multiaxial lay-ups and was chosen because of its widespread interest and application in the aerospace industry. Support for this study was provided by the NASA sponsored Advanced Subsonics Technology (AST) program, a cooperative effort between government, industry, and universities to conduct research to develop the advanced gas turbine engines of the future. The study was carried out utilizing the facilities of the Structures and Acoustics Division located at the NASA Lewis Research Center.

Unique experimental techniques were developed and employed for the isothermal tests. These included designing untabbed, reduced gage section, tensile and unsupported compressive specimens, developing accurate methods of temperature control and measurement for quartz lamp heating, and programming advanced software to drive the hydraulic load frame. The unsupported compressive specimen design allows the composite to fail as a result of natural consequences such as out of plane deformations and buckling failure modes. This is in contrast to most monotonic and fatigue data dealing with compressive load regimes. Most studies use antibuckling guides which limit compressive failures to crushing

modes. These pure compressive failures achieved while using buckling guides are of little practical value in the design of composite components since components are usually designed for buckling or post buckling behavior governed by stiffness criteria. The quartz lamp heating system was used because of its dynamic capabilities making it suitable for future thermomechanical fatigue (temperature and load varying simultaneously). An innovative technique to acquire the temperature in the gage section was developed here. A calibration scheme was designed to establish a relationship between the coupon gage temperature and thermocouple temperature. Microstructural damage mechanisms were extensively studied using non-destructive, in-situ edge view microscopy and destructive sectioning of the coupons. Comparisons were conducted between the temperature extremes concerning the damage and failure mechanisms. The longitudinal stiffness was monitored and recorded during each test. This macroscopic property was then related to the residual compressive strength as well as the actual microscopic damage mechanisms. Chapters II and III discuss the experimental set-up and results, respectively.

A phenomenological analytical model based on the modulus degradation as a damage variable was established. The fatigue damage accumulation law proposed incorporates a scalar representation of damage, but admits an anisotropic evolutionary law. The model predicts the current damage state (as quantified by current stiffness) and remnant life of a composite that has undergone a known cyclic load at temperature. The damage/life model is a function of the multiaxial maximum fatigue stress, the multiaxial fatigue mean stress, the current level of damage, and temperature. Chapter IV contains a description of the paradigm and its application/comparison in respect to the present data.

Finally, Chapter V gives a brief description of the experimental and analytical accomplishments, conclusions, and future directions.

CHAPTER II

MATERIAL, TEST EQUIPMENT AND TEST PROCEDURES

2.1 Introduction

This chapter presents an in-depth discussion of the experimental facilities utilized for this study. In addition, details regarding material fabrication and the design of the test specimen geometries are presented. Technical and practical aspects that guided the development of software that controlled both monotonic and cyclic fatigue tests are given. Sections concerning damage inspection techniques, and a complete overview of the test procedure as well as a test matrix follow later in the chapter. Detailed explanations are provided for each of these topics since they impact the interpretation of the fatigue data presented in the next chapter.

2.2 Material

The high temperature PMC employed in this study carries the designation T650-35/PMR15. The laminated composite was fabricated by General Electric Aircraft Engines (GEAE) in support of the NASA sponsored Advanced Subsonic Technologies (AST) Program. This material is a carbon fiber/polyimide composite with a two dimensional fiber architecture. An 8-harness satin balanced (0/90) cross-weave was utilized in fabricating each ply. Plate specimens that measured 35.6 by 35.6 cm (14 by 14 in.) were supplied in two

sizes concerning the thickness, i.e., plates with a 10-ply thickness, and plates with 16 plies through the thickness. The average thickness of the 10-ply plates was 0.323 cm (0.127 in.). The average thickness for the 16-ply plates was 0.533 cm (0.210 in.). Ultrasonic C-scans were conducted to ascertain fabrication quality prior to testing. C-scans are damage assessment tools that transmit ultrasonic signals through an object. After an ultrasonic wave passes through a specimen, the wave attenuation is analyzed for indications of damage. The details of this procedure have been presented in a discussion by Cantwell and Morton (1992). In this study the results of the C-scans indicated that the overall fabrication quality was consistent from plate to plate with very little signal attenuation. The material was fabricated in a multistep process. The details of the fabrication process subsequent to stacking the towpregs have been listed in Table I.

Test specimens were cut at the NASA Lewis Research Center from the laminated plates using an abrasive water-jet procedure. After cutting and prior to testing, specimens were dried for 72 hours at 121.1 °C (250 °F) in a 94.8 Pa (28 in. Hg) vacuum. To minimize moisture absorption after the drying procedure, specimens were stored in a desiccator until they were utilized in the test program.

Values for an average glass transition temperature of the matrix (T_G) and an average fiber volume fraction were established based on data obtained from each plate supplied by GEAE. Six samples were taken from the two 10-ply plates (i.e., three samples from each plate). Twelve samples were obtained from the four 16-ply plates. A glass transition temperature of 335 °C (635 °F) was obtained through a rheological analysis which was later verified by thermal mechanical analysis (TMA). The average fiber volume fraction of 0.64 was established through procedures set forth in ASTM Standard D 3171.

2.3 Specimen Design

Two dog-bone specimen configurations were employed in this study. The first dog-bone configuration, identified as Coupon **A,** was utilized in tensile tests where the loads were

TABLE I. FABRICATION PROCESS

Autoclave Temperature Schedule
- 51.7 to 221.1 °C (125 to 430 °F) in 180 mins. at a rate of 0.94 °C/min. (1.7 °F/min.)
- Hold at 221.1 °C (430 °F) for 180 mins.
- 221.1 to 248.9 °C (430 to 480 °F) in 25 mins. at a rate of 1.1 °C (2 °F/min.)
- Hold at 248.9 °C (480 °F) for 45 mins.
- 248.9 to 315.6 °C (480 to 600 °F) in 60 mins. at a rate of 1.1 °C/min. (2 °F/min.)
- Hold at 315.6 °C (600°F) for 180 mins.
- Cool to 65.6 °C (150 °F) in 120 mins. At a rate of 2.1 °C (3.8 °F/min.)

Vacuum Schedule
- 10.2 to 87.6 Pa (3 to 5 in Hg) while heating to 148.9 °C (300 °F)
- Apply full vacuum at 148.9 °C (300 °F)

Pressure Schedule
- Apply 1379 kPa (200 psi) at 243.3 °C (470 °F)
- Release pressure during cool down at 204.4 °C (400 °F)

Post Cure
- 23.9 to 246.1 °C (75 to 475 °F) in 100 mins. At a rate of 2.22 °C/min. (4 °F/min.)
- 246.1 to 287.8 °C (475 to 550 °F) in 150 mins. at a rate of 0.28 °C (0.5 °F/min.)
- Hold at 287.8 °C (550 °F) for 300 mins.
- 287.8 to 315.6 °C (550 to 600 °F) in 100 mins. at a rate of 0.28 °C (0.5 °F/min.)
- Hold at 315.6 °C (600 °F) for 600 mins.
- 315.6 to 204.4 °C (600 to 400 °F) in 50 mins. at a rate of 2.22 °C (4 °F/min.)
- Remove from oven and cool at room temperature in desiccator.

increased monotonically. The other dog-bone specimen, identified as Coupon **B,** was uti-lized in monotonic compression tests and in fully reversed fatigue tests. Both dog-bone specimen geometries were flat and untabbed. A general schematic of the dog-bone coupon is shown in Figure 2.1. Dimensions for both dog-bone configurations are given in Table II. As a general practice, a minimum width (W2 in Figure 2.1) of 1.91 cm (0.75 in.) was established for both coupons to ensure that enough of the woven architecture was encom-passed in the gage section so as not to violate the continuum assumption. The design for Coupon **A** was based on a modified version of a reduced gage section coupon used for high temperature testing of metal matrix composites (MMCs) and ceramic matrix composites (CMCs). The original geometry of this reduced gage specimen was developed by Worthem (1990). All Coupon **A** specimens were cut from plates with a 10-ply thickness. These thin coupons were only utilized for the monotonic tensile tests due to specimen buckling (insta-bility) concerns.

Coupon **B** was employed for experiments with compressive loads - i.e., either compres-sive loads that were increased monotonically, or fully reversed tension-compression fatigue tests. In order to minimize instability under compressive loads all the Coupon **B** specimens were fabricated from the 16-ply plates, i.e., the thicker plate. This coupon has a short, un-supported gage section, and a large grip area. This large grip area allowed load transfer between the serrated grip surfaces and the untabbed specimens without slipping or crush-ing. The dimensions of this coupon were optimized in order to:

- minimize the unsupported length between the grips to prevent buckling;

- maximize the unsupported length between grips to allow room for the quartz lamps (see the following section for a discussion on this issue);

- establish a transition radius which allowed an adequate reduction of area to fa-cilitate failure within the gage section;

Preliminary monotonic compression tests were conducted using 16-ply specimens. These preliminary test specimens were rectangular (i.e., not a dog bone geometry) with a
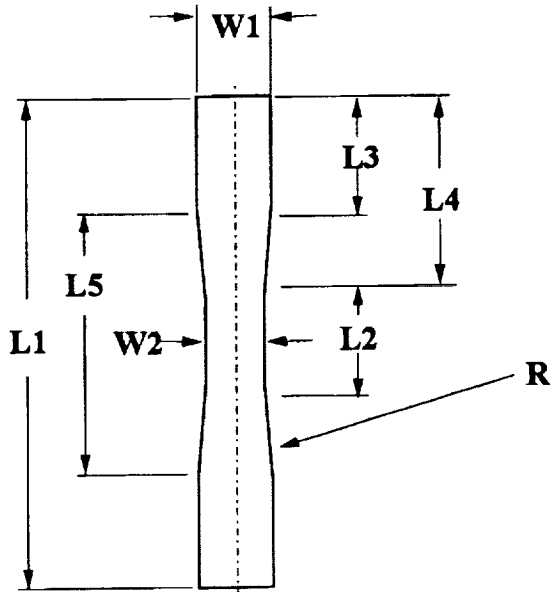
Figure 2.1 General schematic of specimen geometry.

TABLE II. DIMENSIONS FOR REDUCED GAGE SECTION SPECIMENS

Dimensions	Coupon A Tensile specimen cm (in)	Coupon B Comp. specimen cm (in)
Length, L1	17.78 (7.00)	15.24 (6.00)
L2	2.79 (1.10)	1.91 (0.75)
L3	4.45 (1.75)	5.72 (2.25)
L4	7.49 (2.95)	6.68 (2.63)
L5	8.89 (3.50)	3.81 (1.50)
Width, W1	2.16 (0.85)	2.03 (0.80)
W2	1.91 (0.75)	1.91 (0.75)
Radius, R	36.83 (14.5)	7.19 (2.83)

15.24 cm (6 in.) length and 1.91 cm (0.75 in.) width. Compression tests were conducted on the rectangular specimens to establish values for the unsupported length of Coupon **B**. Strain gages were positioned on both faces to study the buckling behavior under load. Typical buckling behavior for the 16-ply rectangular specimens as a function of unsupported lengths is shown in Figure 2.2. Note that the variation of Strain Gage 2 depicted in Figure 2.2(a) was due to a slight misalignment of the strain gage in respect to the load axis of the specimen. It was concluded from trends such as in Figure 2.2 that an unsupported length 3.81 cm (1.50 in.) was acceptable for the load ranges employed in this study. The final configuration accommodated relatively large stress values, and sustained the highest percentage of gage failures, without exhibiting signs of buckling failure. The transition radius from the grip area to the gage section reduced the specimen width from 2.03 cm (0.80 in., W1 in Figure 2.1) in the grips to 1.91 cm (0.75 in., W2 in Figure 2.1) in the gage section while maintaining a straight sided gage length of 1.91 cm (0.75 in., L2 in Figure 2.1).

In addition to the uniaxial compression specimens used to establish the unsupported gage length for Coupon **B**, a second rectangular specimen was utilized to generate benchmark data. The data acquired from these rectangular specimens provided information upon which a comparison could be made with the compression data obtained from the Coupon **B** configuration. Here the rectangular specimens were cut from the thinner 10-ply plates and had nominal dimensions of 11.43 × 1.27 cm (4.5 × 0.5 in.). These specimens were tested in the standardized Wyoming Modified Celanese (WMC) compression test fixture. The WMC fixture was employed for monotonic compression tests at room temperature. The WMC fixture represents a design improvement relative to the ASTM Standard D3410 Celanese Compression Test Fixture. The primary improvement involves a new grip design that allows for variable specimen tab thickness ranging from 0.38 to 0.64 cm (0.15 to 0.25 in.). The standard ASTM fixture requires a relatively precise specimen tab thickness of 0.40 ± 0.005 cm (0.157 ± 0.002 in.). Specimens tested in the WMC fixture were tabbed using a 0.076 cm (0.03 in.) thick quasi-isotropic glass/epoxy. Therefore, the
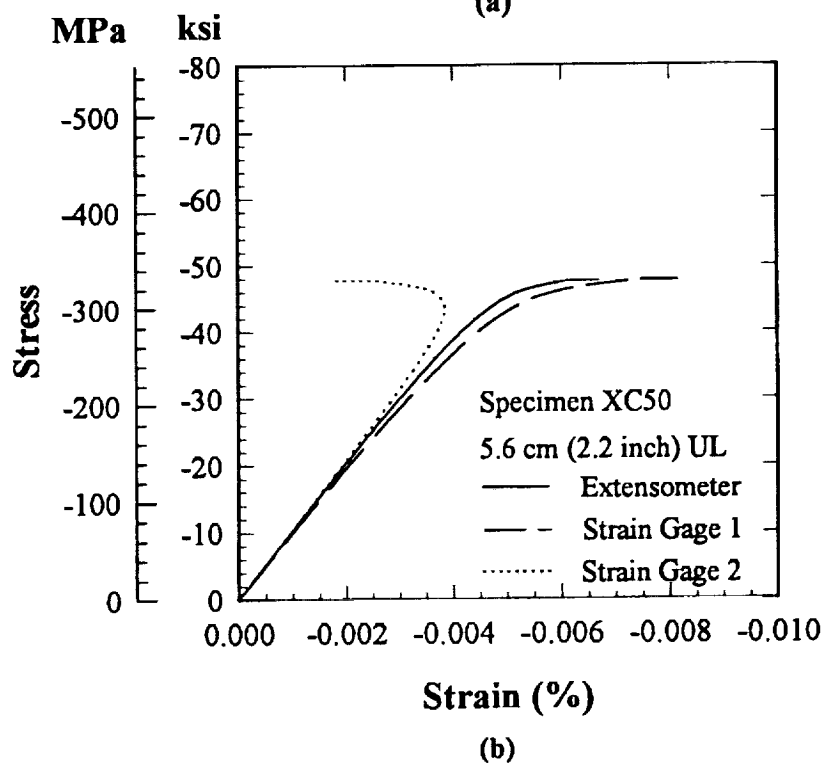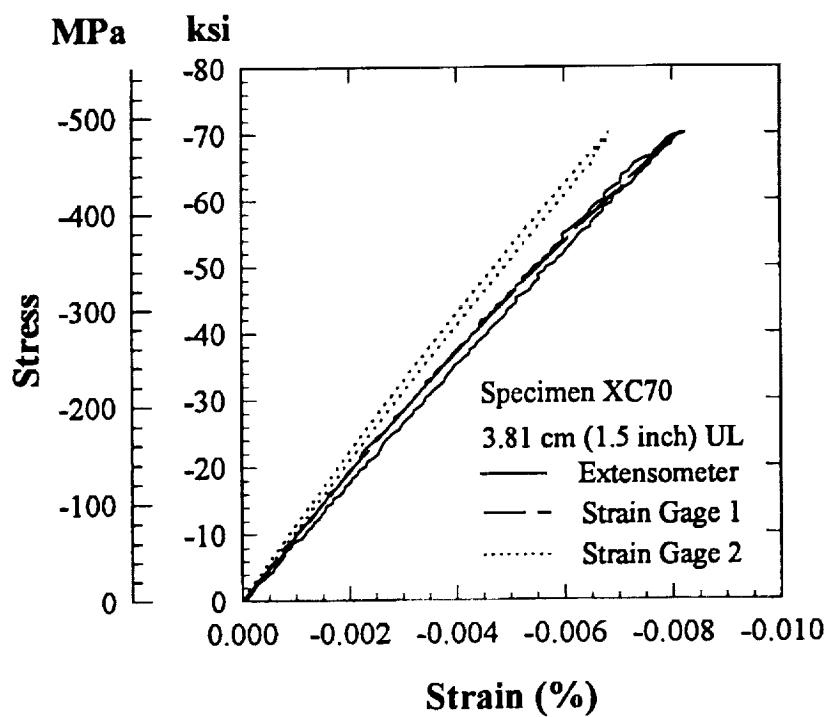
Figure 2.2 Preliminary compressive tests to study buckling as a function of unsupported length (UL). (a) No apparent buckling. (b) Strain gage behavior indicative of buckling.

overall tab thickness of the specimen utilized for the WMC fixture was 0.483 cm (0.190 in.). The reader is directed to the ASTM Standard D3410 and the Wyoming Test Fixtures Incorporated Product Catalog for further details concerning the fixture.

2.4 Equipment

The test rig utilized for this program is a closed-loop, servo-hydraulic system with a load capacity of 88.96 kN (20 kip). The system is depicted in Figure 2.3. Specimens were gripped with hydraulic actuated, water cooled, diamond pattern serrated, wedge grips. A high resolution linear variable differential transformer (LVDT) was utilized to assure precision in controlling and monitoring displacement. Typically, a standard ±12.7 cm (±5 in.) range LVDT is used. Here, a high resolution LVDT with a maximum displacement of ±0.508 cm (±0.20 in.) was employed.

Longitudinal strain measurements were obtained using an air cooled extensometer with a 1.27 cm (0.5 in.) gage length. The extensometer was mounted on the edge of the specimen. Contact with the coupon was achieved by using conical end point probes fabricated from high purity alumina. To prevent the probes from slipping, a small amount of Elmers® glue was applied to the probe tips for both room temperature and elevated temperature specimens. The spring force was approximately 2.9 N (0.055 lb). Periodically transverse strain measurements were made at room temperature. This information was obtained using commercially available strain gages. The transverse strain gages had gage lengths of 0.635 cm (0.25 in.).

Specimens were heated using high intensity tungsten-filament quartz bulbs (500 W/bulb). Lamps were positioned on either side of the gage section facing the width of the specimen. The long axis of the lamps were oriented perpendicular to the loading axis. Two sets of lamp bodies were constructed for this study. For the monotonic tensile tests where ample space was available between the grips, larger three bulb bodies were employed. When using the shorter compressive specimens with 3.81 cm (1.50 in.)
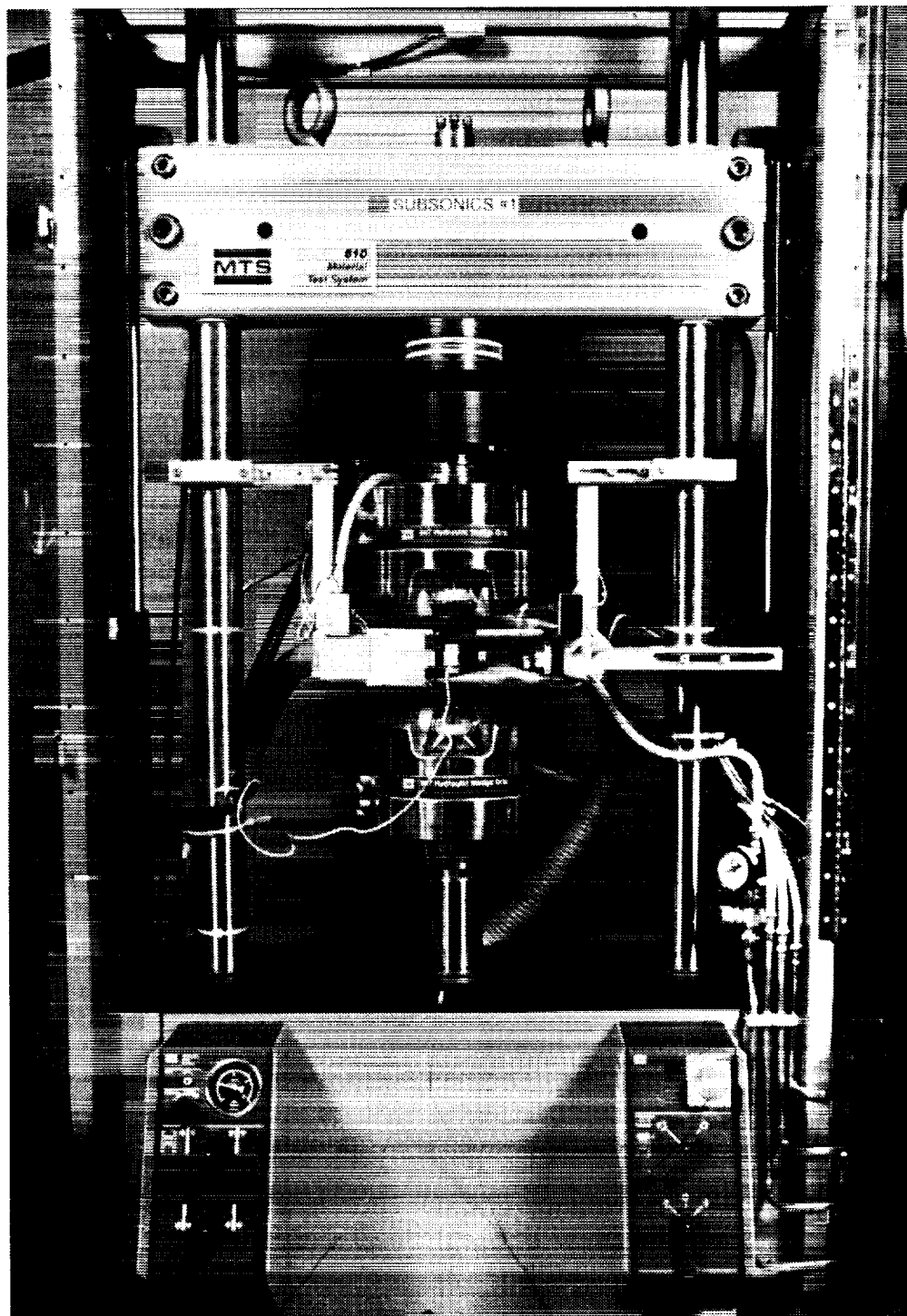
Figure 2.3 Uniaxial composite test system.

between grips, smaller single bulb bodies (500 W/bulb) were utilized. A schematic showing the large bodied lamps is provided in Figure 2.4. Parabolic reflectors inside the lamp bodies focused radiant energy evenly over the specimen. The single zone heating system was controlled by a self-tuning closed loop temperature controller. Adjustable support fixtures allowed the lamp bodies to be maneuvered independent of one another. This facilitated the reduction of temperature gradients over the gage section. The minimal response time of the quartz lamps made them well suited for this test program and future thermomechanical fatigue experiments.

An innovative test technique was developed in this test program to obtain accurate temperature measurements. For conductive materials, such as MMCs, thermocouples can be spot-welded directly onto the surface of the specimen to obtain surface temperatures. This approach was discussed by Castelli et al. (1992). Since PMCs are not conductive, it was not possible to include the specimen in a thermocouple circuit. Thus a technique was developed that essentially embeds a thermocouple in a bead of material. The bead material must be similar to the non-conductive test specimen. The bead with the embedded thermocouple is then attached to the surface of the specimen. The beaded thermocouple approach was advocated by Butkis (1991) for CMC materials, which are also non-conductive. In the Butkis study (which utilized quartz lamp heating), the temperature of the bead was assumed to be equal to the specimen temperature. This assumption was not substantiated with experimental data produced during this study. Here an effort was made to verify the beaded thermocouple temperature with the specimen temperature. A description of the construction and calibration of the thermocouple set-up ensues.

A K-type thermocouple was embedded in a block of PMR15 polyimide which was then attached to the coupon using a small stainless steel clip as shown in Figures 2.5 and 2.6. The block was a fiberless composition of PMR15 since the inclusion of conductive carbon fibers would have interfered with the thermocouple current. The block was shaped as a cube with a common length, width and height of 0.254 cm (0.10 in.). For this study a single block

SPECIMEN FACE VIEW
(Front lamp not shown)

SPECIMEN EDGE VIEW
(Extensometer not shown)

Extensometer

Heat shield

Ceramic probe

Hydraulic grip

Specimen

CCD camera

PMR-15 cube with embedded k-Type thermocouple

Reflector

Lamp body

Quartz bulb
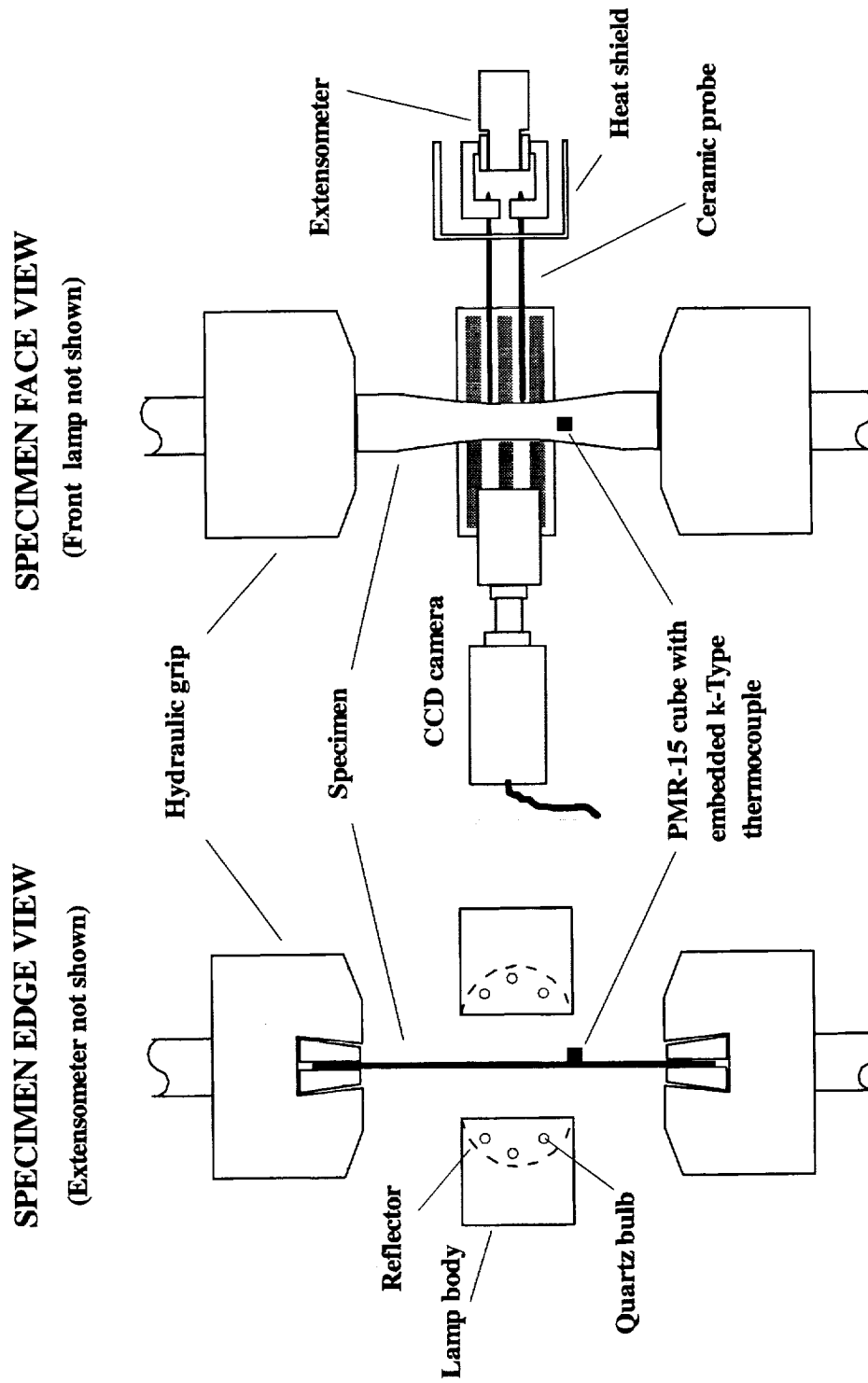
Figure 2.4 Schematic of test set-up.
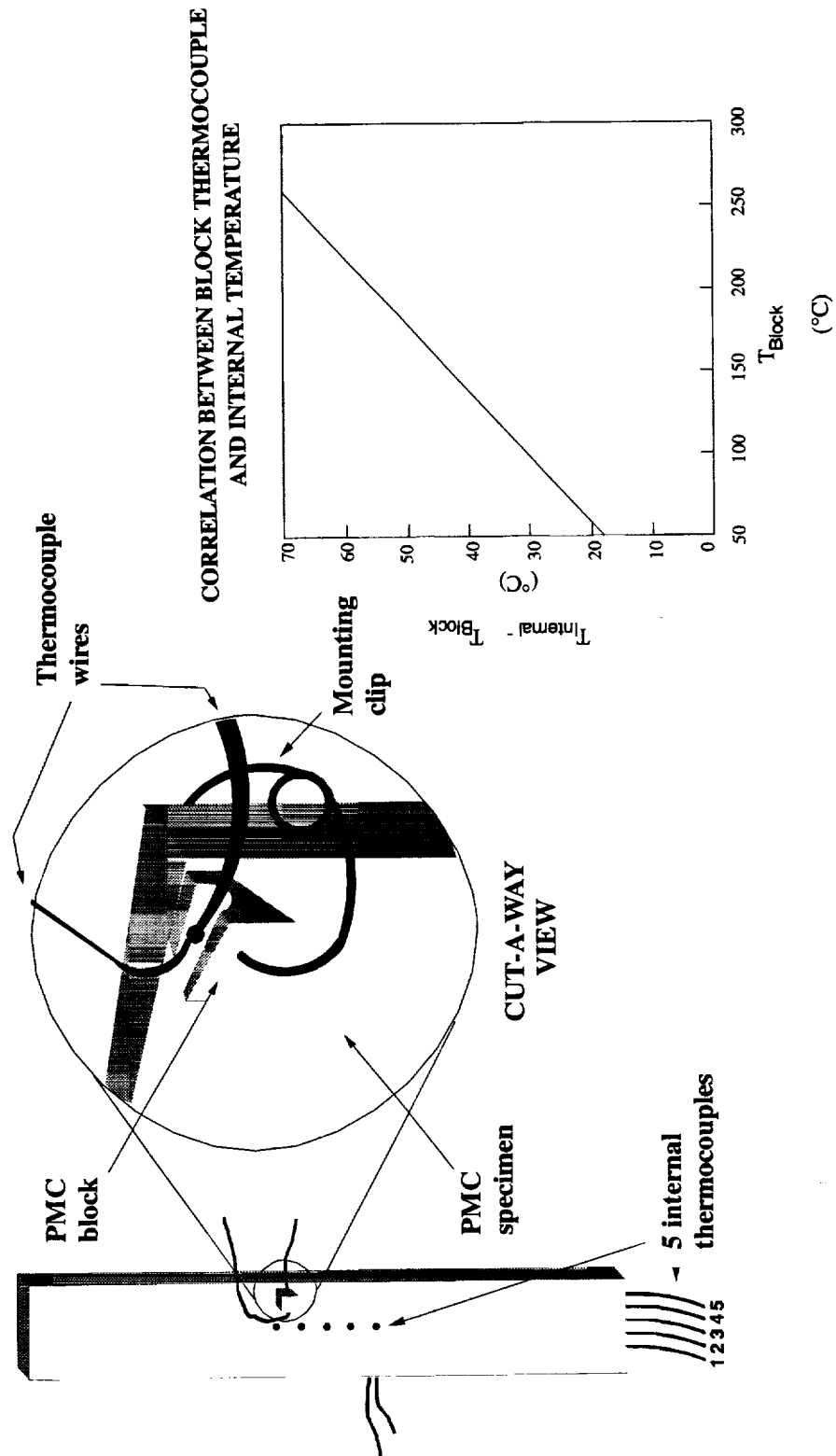
Figure 2.5 Schematic of calibration specimen, thermocouple block, and typical correlation curve.

Figure 2.6 Close-up edge view of specimen in test fixture. Shown are thermocouple blocks, attachment clips, quartz lamps, and extensometer on opposite edge.

thermocouple was attached to each specimen. The assumption here was that the lamps uniformly heated the gage section. By placing the block just outside of the gage section and employing a relatively small clip, the problem of shading the specimen from the radiant heat by the block and clip was minimized.

Before the test program started there were rational expectations that the block temperature would not be equal to the coupon gage temperature. It was felt that the geometry and differing thermal boundary conditions between the block and the specimen would contribute to the temperature differential. These expectations were born out. By utilizing calibration specimens with five internal thermocouples located in the central region of the gage section, a temperature differential was established between the internal thermocouples and the block thermocouple.

Two calibration specimen geometries were fabricated that corresponded to the two dog-bone specimen designs discussed previously. The thermocouples were positioned internally during the processing of the calibration specimens. The five thermocouples spanned a total length of 2.54 cm (1 in.) along the gage section, with a 0.635 cm (0.25 in.) spacing in-between. A linear relationship between internal coupon temperatures and block temperatures was established by checking various temperatures and correlating the measurements. At each step increase the lamp intensity was maintained for a period of time to allow thermal equilibrium in both the blocks and the specimens. From these measurements, correlation curves for the specific laminate lay-up and geometries were constructed. A typical curve is depicted in Figure 2.5. To verify repeatability, the calibration specimen and block were removed from the grips and allowed to cool. The calibration specimen was then reinstalled and data was taken once again using the same temperature cycle. The results of this exercise showed little variations. The procedures for block correlation and gradient adjustments were periodically repeated during the test program to demonstrate minimal variations in test temperatures. Thereafter, the specimen temperatures were obtained from the thermocouple block and correlation curve.

The coupons with the internal thermocouples were also used to establish the positions of the quartz lamps in order to minimize or eliminate temperature gradients in the gage section. Once lamp positions were established, the maximum temperature was located at the center internal thermocouple. The readings at the gage section boundaries, located ±1.27 cm (±0.50 in.) from center of the specimen, were at most 3 °C (5.4 °F) below the center line temperature.

2.5 Real-Time Control Software

Both monotonic and fatigue experiments were conducted under computer control. Early in the test program a conscious decision was made to use load control instead of strain control. This decision was made due to difficulties alluded to earlier with the extensometer maintaining contact with the specimen. Debonding of fiber bundles and fiber bundle breaking along the coupon edge can easily dislodge the extensometer probes. If the test is conducted in strain control these events can force a premature end to the test. Also, under load control the definition of failure can be easily defined as the complete fracture of the specimen. As noted earlier, an extensometer was utilized in all the tests to record strain information, but this information was not used to control the test.

A FORTRAN algorithm was developed as part of this research project to control the hydraulic system. The main state-of-art attribute of the fatigue software was the ability of simulating the conditions of one control mode while being in another. For example, tests were conducted utilizing displacement control between fixed load limits and constant load rates (any combination of displacement, load, and strain was possible). The difficulty concerning load control of a hydraulic system arises when a specimen fails during compression. Under load control the system increases hydraulic pressure in an attempt to attain the specified load. Since the interlocks have a short time delay before activating, this failure event can damage the equipment located between the grips. The software developed here prevents this sort of damage from occurring by allowing the fully reversed fatigue tests to

operate under constant load limits and constant load rates (i.e., a load control environment) while maintaining the hydraulic rig in displacement control. The advantage of displacement control is the fact that the hydraulic rig increments the displacement by a fixed amount regardless of the specimens compliance. If the specimen fails, the increment remains constant. The hydraulic system is thereby operating in a closed loop independent of the specimen. Parameters relating the control mode of the hydraulic system (displacement) to the mode to be imitated (load) were updated with each cycle to assure that constant load rates were maintained with changing specimen properties.

An ability to periodically zero the specimen load in order to conduct elastic tensile and compressive moduli tests was incorporated into the fatigue software. Here the intent was to measure the current moduli as a function of accumulated cycles. As the computer algorithm initiated the routine to collect information to determine current moduli values, the coupon was loaded and unloaded three times for both the tensile and compressive moduli tests. The maximum tensile stress applied to the test specimen while acquiring the tensile modulus was 140 MPa (20 ksi). The maximum compressive stress applied to the test specimen in order to obtain the compressive modulus was −140 MPa (−20 ksi). These stress values were chosen so as not to cause further damage while the current moduli were acquired. As Gyekenyesi et al. (1995) pointed out these stress values were approximately 30 percent of the monotonic stress levels needed to induce transverse cracks in a similar lay-up composed of an AMB21 polyimide resin weave with equivalent fiber type, content and lay-up. The tensile moduli were determined for each of the three tensile cycles and an average value was recorded. Similarly, the compressive moduli were calculated for each of the three compressive loadings and then averaged. The moduli solutions involved fitting a first order linear regression to the unload portion of the individual stress-strain curves in the tensile and compressive regimes. The recorded moduli was the slope of this regression curve.

Stress, strain, and displacement data were acquired and archived to data files. A minimum of 100 data points were collected per cycle. The software was programmed to archive

information for the two cycles previous to the current cycle. This archive was updated for each cycle. Thus, if a specimen failed during the current cycle an archive existed for the last two cycles prior to failure. These last two stress-strain cycles provided information that allowed the calculation of the final moduli by post-processing. The tensile modulus was obtained by calculating the slope of the loading segment of the fatigue stress-strain curve. This portion of the stress-strain curve was bounded by 0 and 138 MPa (20 ksi). The compressive modulus was post-processed by obtaining the slope of the compressive loading regime of the fatigue stress-strain curve. This portion was bounded by 0 and −138 MPa (−20 ksi). The maximum stresses used to calculate the post-processed moduli corresponded to the stress range used to calculate the elastic moduli obtained during the periodic routines as discussed above. Gyekenyesi et al. (1995) showed the post-processed moduli obtained from a stress-strain fatigue cycle will have similar values when compared to measured elastic moduli obtained by the above procedure. However, differences could arise in some materials if a large hysteresis occurs during the fatigue cycle.

2.6 Damage Inspection

Documenting the microstructural damage events as a function of residual life and current modulus was a major objective of this test program. Microstructural events of particular interest were:

- transverse cracks in both the resin rich areas and through the fill bundles,
- debonding of warp and fill bundles from the resin,
- delamination between plies, and
- fracture of fiber bundles.

Inspection techniques utilized included edge view microscopy (in-situ) and destructive sectioning. The information gathered from these procedures was used to develop a qualitative understanding of the relationship between macroscopic behavior and these microstructural events.

The equipment for edge view microscopy is shown schematically in Figure 2.4. The viewing edge of each specimen in this test program was polished using 200-grit sandpaper, followed by sanding with 400 grit, and finally with 600 grit paper. Real time observations of the polished specimen edge were conducted using a charged coupled device (CCD) video camera with a 135 mm lens attachment. The viewing area of the gage section (observed on a video monitor) was approximately 0.5×0.5 cm (0.2×0.2 in.). Here the lens was located 25 cm (10 in.) from the specimen edge. This view provided enough resolution to observe significant events, and also provided a large enough viewing area to be representative of the gage section. The information was recorded and stored using a video cassette recorder (VCR). The video tape and computer generated cyclic data were correlated through the use of the VCR's time counter. For tests lasting more than two hours the VCR was programmed to record the edge view at specified time intervals. Usual settings allowed for approximately 20 to 30 recordings throughout the specimen life with each segment lasting one minute.

Destructive examinations were conducted on specimens obtained from interrupted tests. Four rectangular pieces were cut from the gage area as shown schematically in Figure 2.7. A diamond cut-off wheel was used. After mounting and polishing, the cut sections were viewed at various magnifications ranging from 5 to 1000x. Figure 2.8 displays the sectional views taken from an untested, undamaged specimen. The four views are labeled to identify the different components (warp yarn, fill yarn, and resin) of the composite system. The views identified in Figures 2.7 and 2.8 are used as a reference in later discussions of results.

2.7 Experimental Procedure

The isothermal monotonic and fatigue experiments were conducted at two temperatures, i.e., 22 °C (72 °F) or room temperature, and 316 °C (600 °F) which will be referred to as elevated temperature. The elevated temperature was approximately 19 °C (35 °F) below the dry glass transition temperature, T_G. Conditions in the laboratory during all tests were maintained at 22 °C (72 °F) and 45 percent relative humidity.
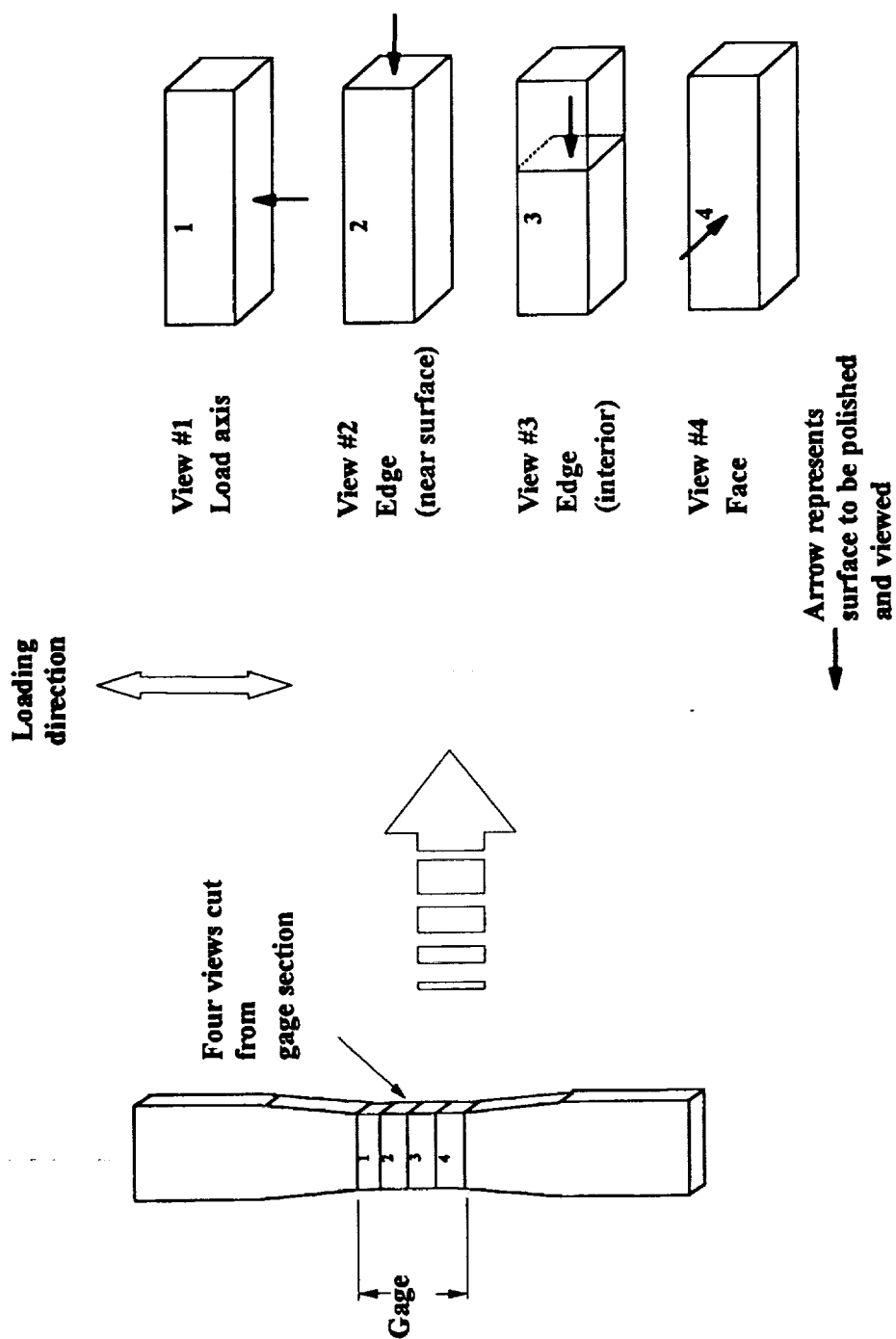
Figure 2.7 Schematic displaying the various views for microstructural analysis.
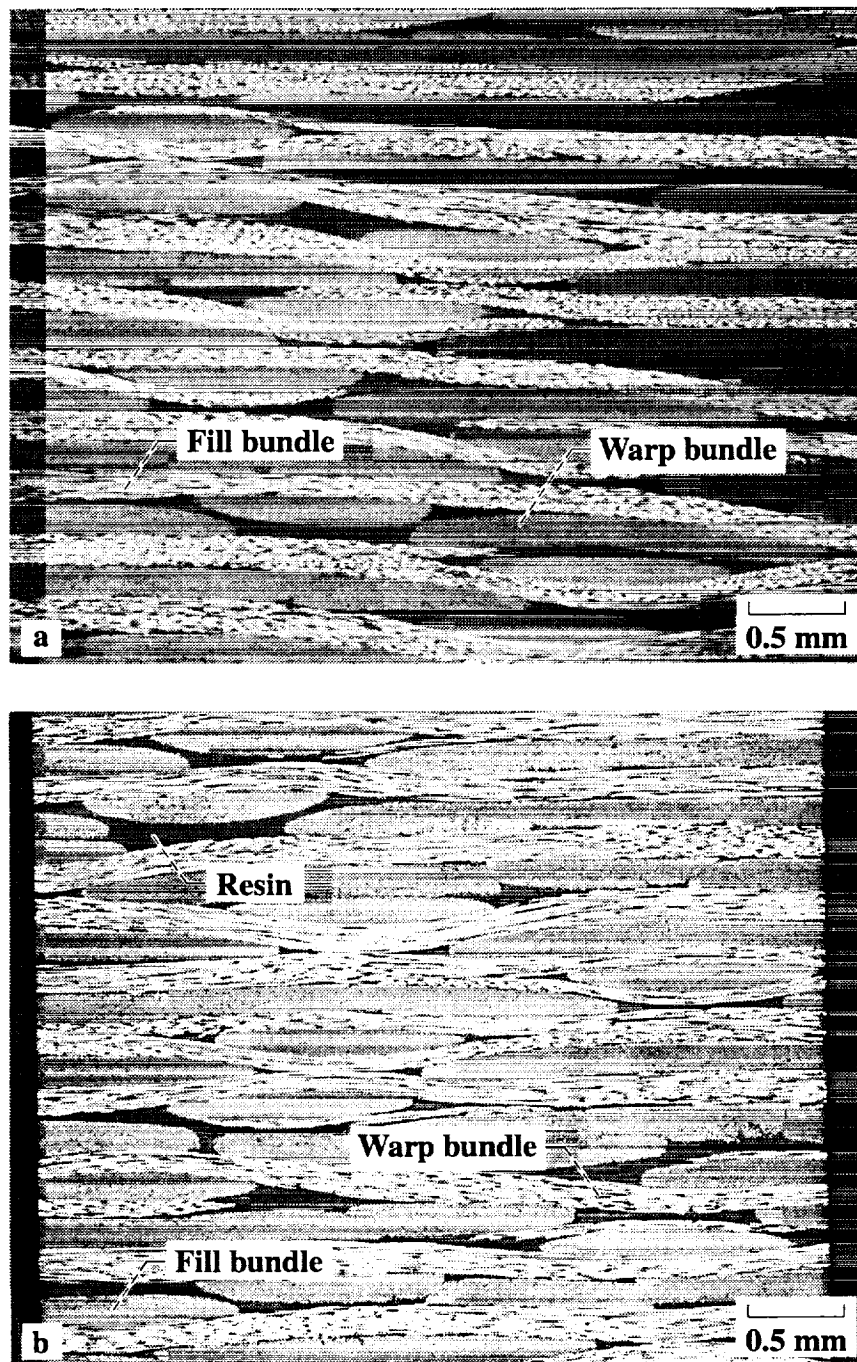
Figure 2.8 Microscopic views of an undamaged specimen at 25x magnification. (a) View #1, load axis. (b) View #2, edge (equivalent to view #3). (c) View #4, face. See Figure 2.7 for explanation of views.
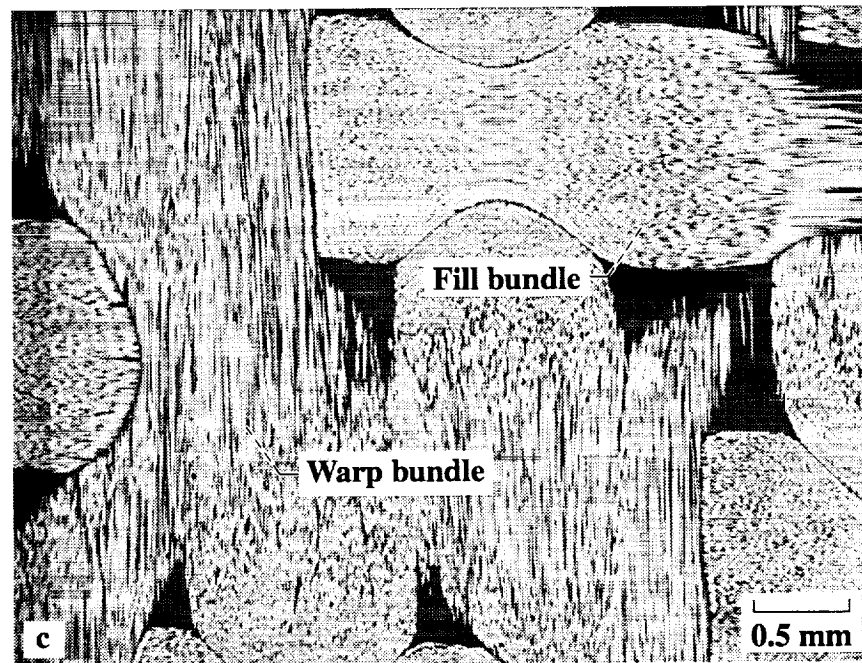
Figure 2.8 Continued.

For each coupon tested at room temperature pre-test tensile and compressive moduli measurements were acquired. However, for coupons tested at elevated temperature both elevated temperature moduli and room temperature moduli were recorded prior to accumulating load history. Specimens tested at the elevated temperature were allowed to soak for ten minutes before mechanical loads were applied. Based on the previous temperature calibration experiments, it was determined that this was sufficient time to allow the system to attain thermal equilibrium. For all tests strain was zeroed after reaching thermal equilibrium, hence only mechanical strains were recorded. For test specimens subjected to monotonically increasing load, the elevated temperature was maintained for approximately ten minutes during the test. Bowles et al. (1996) indicates that for this type of material thermo-oxidative degradation will not occur for the short exposure times used here. Therefore, the behavior of the coupons subjected to monotonically increasing loads was purely a function of the temperature dependent mechanical properties. Monotonic tensile and compressive tests were duplicated at least three times at both room temperature and elevated temperature. Specimen failure for both the monotonic tests and the fatigue tests was defined as complete fracture of the specimen into distinctly separate pieces.

The monotonic tensile tests were conducted in load control using test Coupon **A** (see Table II). The load rate was 20.7 MPa/sec (3 ksi/sec) which resulted in tests lasting approximately one minute. Displacement control was utilized for the monotonically increasing compression tests. Here test Coupon **B** (see Table I) was employed. The displacement rate was –0.00254 cm/sec (–0.001 in./sec) with a test duration of approximately one minute. Finally, to validate the monotonic compressive behavior of the Coupon **B** design, the WMC fixture was employed at room temperature. Again, displacement control was utilized at a rate of –0.00254 cm/sec (–0.001 in./sec).

The isothermal fatigue experiments were conducted at multiple levels of maximum stress. However, the stress ratio for all fatigue experiments was maintained at $R_\sigma = -1.0$ ($\sigma_{min}/\sigma_{max}$). The maximum stress values yielded lives of 10^1 to 10^6 cycles to failure at both

test temperatures. Due to difficulties in maintaining extensometer contact with the specimen edge, it was necessary to limit the cyclic load frequency to 2 Hz. Therefore, a cyclic load frequency of 2 Hz was employed with a triangular load wave form. At this rate probe contact was maintained. All the fatigue specimens were subjected to constant load limits and constant load rates while utilizing displacement control (see section 2.3 for more discussion).

2.8 Interrupted Tests

Certain monotonic tests and certain fatigue tests were interrupted in order to ascertain information concerning microstructural damage, degraded moduli and residual strength. Selected monotonic tensile and compressive tests were interrupted to obtain sections for microstructural analysis. The sectioning procedure effectively destroys the specimen. The destructive examination experiments were stopped at approximately 55 and 90 percent of the ultimate tensile and compressive strengths. In addition, selected fatigue tests were interrupted to acquire information regarding the relative state of the microstructure as well as obtaining values for the residual compressive strength. The tests were interrupted based on the degradation of the tensile and compressive moduli. These moduli were monitored periodically throughout the fatigue test. As was discussed in Chapter I, the moduli degradation behavior can be classified into several stages. Tests were interrupted based on the moduli degradations corresponding to these three stages. The control software was programmed to interrupt a fatigue test when either the compressive or tensile moduli decreased to predefined values. Specific values of moduli degradation are discussed in the next chapter. For each predetermined interruption point two coupons were obtained. One coupon was selected for destructive examinations while the other was used to obtain the residual compressive strength.

CHAPTER III

EXPERIMENTAL RESULTS AND DISCUSSION

3.1 Introduction

This chapter contains experimental results from monotonic strength tests and cyclic fatigue tests conducted on the PMC material system discussed in the previous chapter. Information pertaining to the uniaxial strength, fatigue life, stiffness reduction and residual strength were obtained at room temperature and elevated temperature. Results from the monotonic tensile tests and monotonic compressive tests are discussed first. Following each of these sections are discussions concerning the microscopic damage mechanisms (transverse cracks, bundle debonds, etc.) and their order of occurrence. An in-depth analysis of the fully reversed fatigue life data appears after the discussion of the monotonic strength data. For both room temperature cyclic fatigue data and elevated temperature cyclic fatigue data, a discussion of macroscopic behavior of the material is followed by details concerning the microstructural damage mechanisms. This latter discussion contains comparisons of damage initiation and damage accumulation for both temperature regimes. Then a final section discussing residual compressive strength is presented.

3.2 Monotonic Tension - Results

The tensile properties of the composite at 22 °C (72 °F, in the discussions that follow

this is referred to as room temperature) and 316 °C (600 °F, in the discussions that follow this is referred to as elevated temperature) are presented in Tables III and IV. Note that in these tables the subscript RT denotes room temperature and the subscript ET designates elevated temperature. It should be pointed out that the stress values presented in the tables and throughout this discussion were calculated based on the initial cross sectional areas of the coupons. In addition, a statistical comparison between the room temperature tensile data obtained from plate 1 (10 plies) and the room temperature tensile data obtained from plate 2 (10 plies) was conducted to check for plate-to-plate variations. Note that specimens from plate 1 were identified as P1 in Tables III and IV. Similarly, specimens from plate 2 were identified with a P2 designation. Statistical comparisons of the standard deviations were conducted using the F-test. Statistical comparisons of the means were conducted using the t-test. Both the standard deviations and the means associated with room temperature properties E, σ_{ult}, and ε_{ult} fell within an interval defined by the 95 percent confidence level for both statistical tests. Thus one is 95 percent confident that the true parameter is contained within this interval. Note that this interval also contains the estimated values for means and standard deviations. Based on these results, coupons were randomly chosen and the values reported herein represent pooled averages.

Elevated temperature had only a minimal effect on composite tensile properties because the tensile behavior of the material was fiber dominated. While the behavior of the polyimide resin is significantly altered at elevated temperatures, the carbon fibers are generally unaffected at the test temperatures in this study. Deterioration of the carbon fibers due to oxidation becomes an issue at temperatures beyond 400 °C (752 °F). To underscore this issue consider comparisons of the ultimate tensile strengths, ultimate tensile strains, and elastic moduli at room temperature and elevated temperature. The average ultimate tensile stress within ±1 standard deviation at 22 °C (72 °F) was 855 ± 17.0 MPa (124 ± 2.46 ksi). The average ultimate tensile stress within ±1 standard deviation at 316 °C (600 °F) was 831 ± 14.3 MPa (121 ± 2.07 ksi). Thus, the ultimate stress decreased approximately

TABLE III. TENSILE TEST RESULTS FOR 10-PLY
T650-35/PMR15 (0/90) WEAVE AT 22°C (72°F)

Specimen ID	$E_{tensile\ RT}$, GPa (Msi)	$E_{comp\ RT}$, GPa (Msi)	$\sigma_{tensile\ ult}$, MPa (ksi)	$\varepsilon_{tensile\ ult}$, %
P1_19	76.5 (11.1)	73.1 (10.6)	869 (126)	1.18
P1_4	75.2 (10.9)	72.4 (10.5)	841 (122)	1.15
P1_15	74.5 (10.8)	72.4 (10.5)	862 (125)	1.18
P1_30	74.5 (10.8)	72.4 (10.5)	855 (124)	1.18
P1_8	76.5 (11.1)	75.2 (10.9)	834 (121)	1.13
P1_17	76.5 (11.1)	74.5 (10.8)	883 (128)	1.20
P2_20	76.5 (11.1)	73.1 (10.6)	876 (127)	1.18
P2_16	74.5 (10.8)	72.4 (10.5)	848 (123)	1.13
P2_5	76.5 (11.1)	73.1 (10.6)	834 (121)	1.08
P2_23	77.2 (11.2)	75.2 (10.9)	855 (124)	1.10
P2_19	78.6 (11.4)	76.5 (11.1)	841 (122)	1.10
Average	76.1 (11.0)	73.8 (10.7)	855 (124)	1.15
Stnd Dev	1.32 (0.191)	1.44 (0.209)	17.0 (2.46)	0.0408

TABLE IV. TENSILE TEST RESULTS FOR 10-PLY
T650-35/PMR15 (0/90) WEAVE AT 316°C (600°F)

Specimen ID	$E_{tensile\ RT}$, GPa (Msi)	$E_{comp\ RT}$, GPa (Msi)	$E_{tensile\ ET}$, GPa (Msi)	$E_{comp\ ET}$, GPa (Msi)	$\sigma_{tensile\ ult}$, MPa (ksi)	$\varepsilon_{tensile\ ult}$, %
P1_23	74.5 (10.8)	72.4 (10.5)	73.1 (10.6)	71.0 (10.3)	827 (120)	1.18
P1_11	76.1 (11.0)	73.1 (10.6)	74.5 (10.8)	72.4 (10.5)	814 (118)	1.10
P1_13	75.2 (10.9)	73.8 (10.7)	73.1 (10.6)	71.7 (10.4)	841 (122)	1.15
P1_25	76.5 (11.1)	74.5 (10.8)	74.5 (10.8)	72.4 (10.5)	821 (119)	1.15
P1_21	76.1 (11.0)	73.8 (10.7)	73.8 (10.7)	71.7 (10.4)	848 (123)	1.24
P1_22	76.1 (11.0)	73.8 (10.7)	74.5 (10.8)	71.7 (10.4)	821 (119)	1.18
P1_24	76.5 (11.1)	74.5 (10.8)	75.2 (10.9)	73.1 (10.6)	848 (123)	1.20
Average	75.8 (11.0)	73.7 (10.7)	74.1 (10.7)	72.0 (10.4)	831 (121)	1.17
Stnd Dev	0.737 (0.107)	0.737 (0.107)	0.782 (0.113)	0.673 (0.0976)	14.3 (2.07)	0.0441

2.8 percent due to elevated temperature. The average ultimate tensile strain within ±1 standard deviation at 22 °C (72 °F) was 1.15 ± 0.0408 percent. The average ultimate tensile strain within ±1 standard deviation at 316 °C (600 °F) was 1.17 ± 0.0441 percent. Thus, the ultimate strain increased by 1.7 percent due to the elevated temperature. In addition, the longitudinal moduli decreased approximately 2.3 percent due to the elevated temperature. Figure 3.1 displays typical tensile stress versus strain behavior for room temperature conditions. Figure 3.2 displays typical tensile stress versus strain behavior at elevated temperature. At both temperatures, the composite showed relatively linear behavior with a slight stiffening as load increased. This increase in stiffness was likely due to the straightening of misaligned fibers and the locking of bundles at the crimp points along the weave. The curve becomes jagged prior to failure—a result of cracking events taking place within the gage area at the onset of failure.

3.3 Monotonic Tension - Microstructural Damage

A generalized schematic identifying various microscopic damage mechanisms for this composite material is depicted in Figure 1.3. During room temperature tests, transverse cracks were initiated at approximately 379 MPa (55 ksi), and these cracks continued to accumulate up to failure. Evidence of this behavior was obtained from the edge view camera and by interrupting monotonic tests at predetermined stress levels. The specimens from the interrupted tests were subsequently sectioned and viewed under magnification. Figure 3.3 illustrates the accumulated damage characterized by a destructive examination of an interrupted test at 758 MPa (110 ksi). The cracks appearing in this figure were viewed from the specimen edge and face (view #2 and view #4 - see Figure 2.7). The transverse crack counts (normalized with respect to observation length and number of plies) were obtained at the interrupted stress levels of 379 MPa (55 ksi) and 758 MPa (110 ksi). Crack counts were only obtained from test specimens that were sectioned. At 379 MPa (55 ksi) the crack count was 0.5 cracks/cm·ply (1.3 cracks/in.·ply) while at 758 MPa (110 ksi) it was
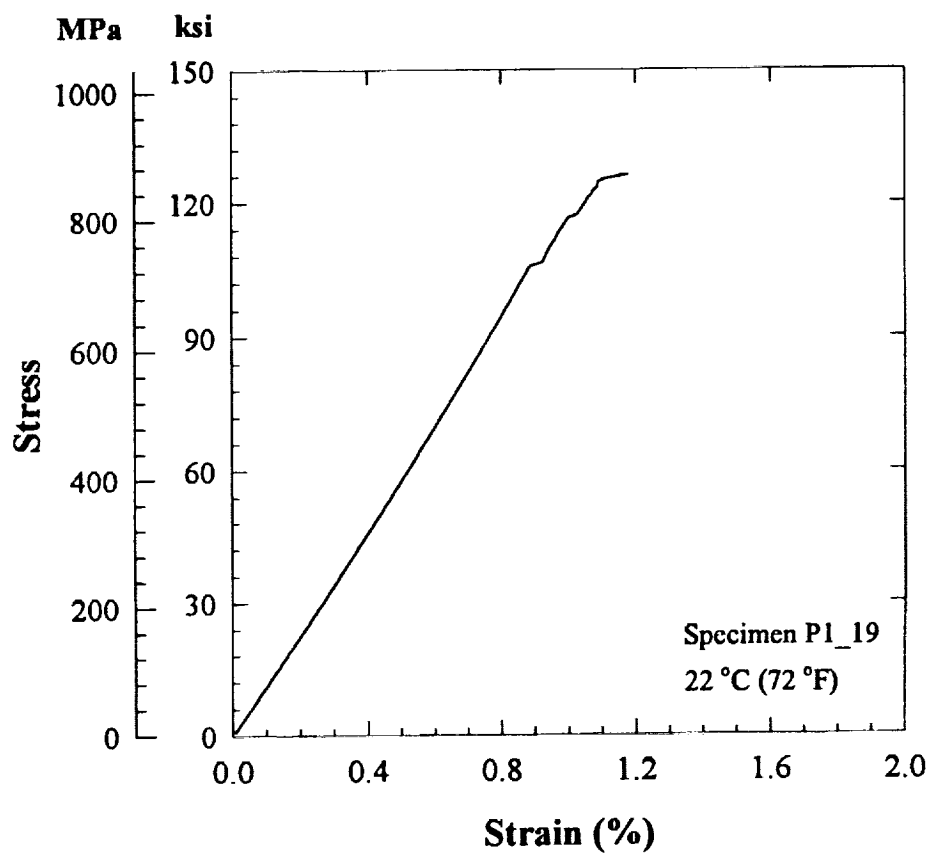
Figure 3.1 Typical monotonic tensile response of T650-35/PMR15 10-ply, (0/90) weave at 22°C (72°F).
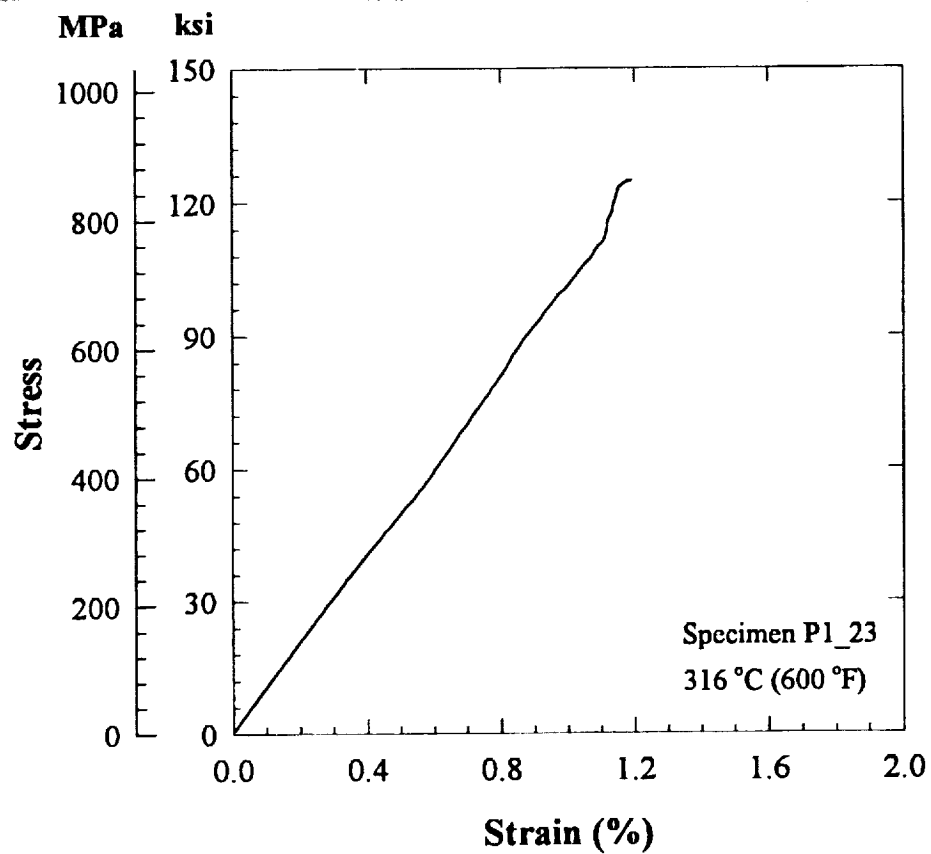
Figure 3.2 Typical monotonic tensile response of T650-35/PMR15 10-ply, (0/90) weave at 316°C (600°F).

Load direction
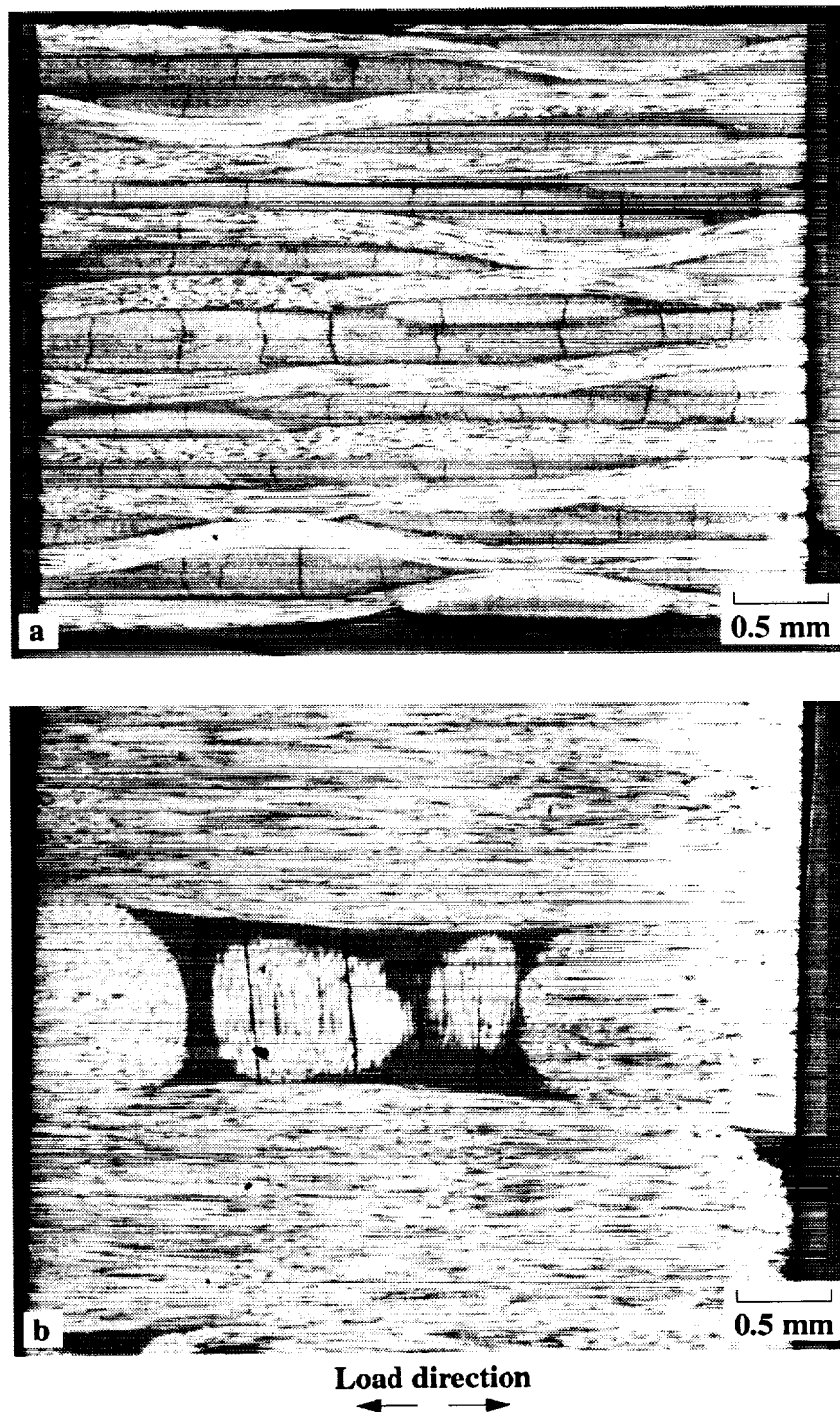
Figure 3.3 Microscopic view of transverse cracks in 22 °C (72 °F) tensile coupon. (a) Edge (view #2) with 25x magnification. (b) Face view (view #4) with 25x magnification: See Figure 2.7 for explanation of view angle: Specimen P1_7.

14.6 cracks/cm·ply (37.1 cracks/in.·ply). At room temperature the transverse cracks appeared to be uniformly distributed through the width and the thickness.

Warp bundle debonds and interlaminar delaminations were next in the sequence of damage events at room temperature. These events occurred at an approximate stress value of 827 MPa (120 ksi). Debonds and delaminations were initiated near the intersection of the face and edge of the test specimen (i.e., the corner of the coupon). Stress concentrations in this region (a result of the Poisson's ratio mismatch between the bundles and resin) were the probable cause of the debonds. Although the debonds and delaminations appeared to occur simultaneously, bundle debonds probably occurred first. These debonds then branched to the resin rich interlaminar area which induced delaminations. Failure occurred shortly thereafter when isolated debonded warp bundles fractured. Figure 3.4 illustrates the sequence of events for the progressive damage attributed to a bundle debond and interlaminar delamination. The sequence was observed from the edge view with the video camera. As a final note, individual fiber fractures within a bundle were not found in any of the room temperature sectioned views.

A slightly different pattern of microscopic damage was observed at 316 °C (600 °F). Warp bundle debonds occurred simultaneously with transverse cracks along the edge of the coupon. These events were first detected via the edge view camera at approximately 414 MPa (60 ksi). Both mechanisms continued to accumulate up to failure. However, in contrast to room temperature tests there was a relatively low density of transverse cracks which was most likely the result of increased ductility of the resin at elevated temperature. Relatively few transverse cracks were detected in the sectioned views taken from specimens at an interrupted stress level of 758 MPa (110 ksi), and none at all were detected at the lower interrupted stress level of 379 MPa (55 ksi). The transverse crack count at 758 MPa (110 ksi) was 2.3 cracks/cm·ply (5.8 cracks/in.·ply). When observed, the transverse cracks were homogeneously distributed through the gage section. Figure 3.5 shows a warp bundle debond viewed from the load axis (view #1 - see Figure 2.7). Again, failure occurred when
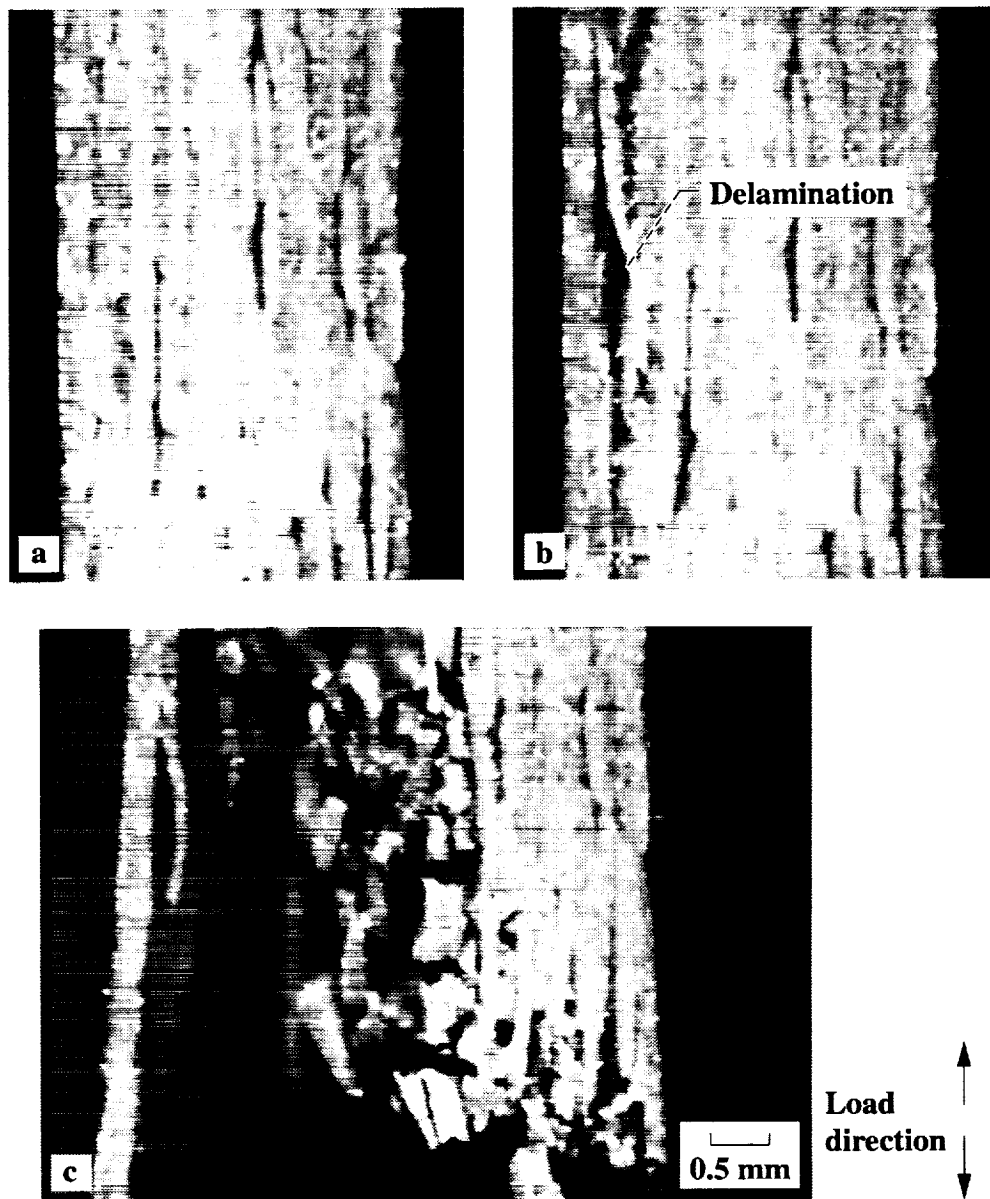
Figure 3.4 Progressive damage in 22 °C (72 °F) tensile specimen as observed using video images of monitored edge view with 15x magnification. (a) Image taken at 793 MPa (115 ksi) before bundle debond and delamination. (b) Debond and delamination at 827 MPa (120 ksi). (c) Failure at 876 MPa (127 ksi): Specimen P1_17.
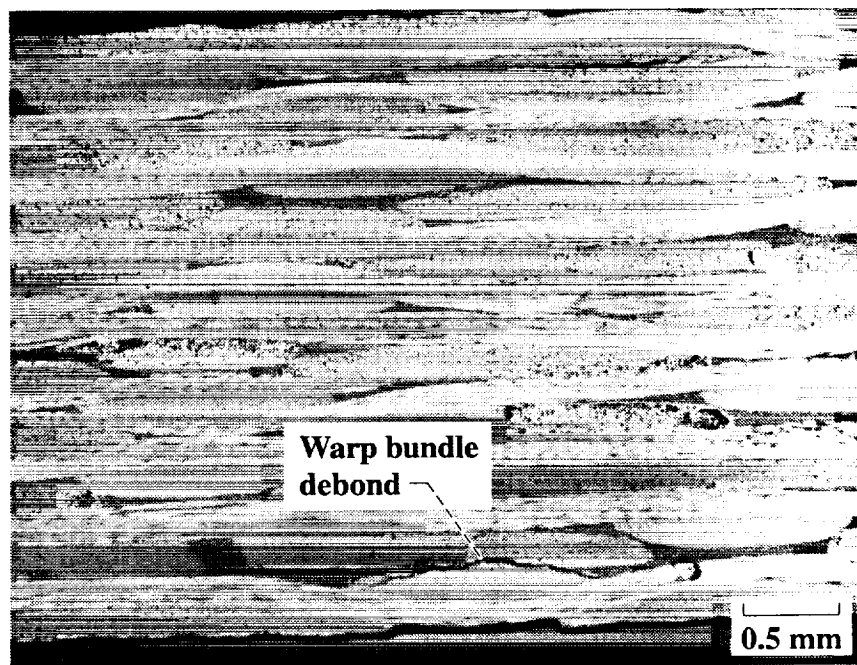
Load direction

Figure 3.5 Warped bundle debonds in 316 °C (600 °F) tensile specimen as observed from the load axis at 25x magnification (view #1; see Figure 2.7): Specimen P1_12.

the isolated debonded warp bundles failed with increasing stress. Figure 3.6 displays the sequence of events leading to failure for progressive damage at the elevated temperature. This sequence was observed from the edge view camera.

3.4 Monotonic Compression - Results

The uniaxial monotonic compressive results are summarized in Tables V, VI and VII. Elevated temperature had a more pronounced affect on the compression properties of the composite. The average ultimate compressive strength within ±1 standard deviation at 22 °C (72 °F) was –675 ± 5.21 MPa (–97.8 ± 0.756 ksi). The average ultimate compressive strength at 316 °C (600 °F) was –629 ± 26.4 MPa (–91.2 ± 3.82 ksi). Thus, the ultimate strength was reduced by 6.7 percent as a result of the elevated temperature. At 22 °C (72 °F) the ultimate compressive strain within ±1 standard deviation was –1.12 ± 0.0457 percent. At 316 °C (600 °F) the ultimate compressive strain was –1.04 ± 0.0465 percent. Thus, elevated temperature caused a 7.1 percent decrease in ultimate strain. Figures 3.7 and 3.8 show typical stress-strain curves for monotonic compression tests at room temperature and elevated temperature, respectively. The strain gage data (gages applied to both faces) appearing in Figure 3.7 verified that macroscopic buckling did not occur (see section 2.3 for an in-depth discussion). At both temperatures nonlinear behavior was observed at the higher load levels, i.e., the stiffness decreased with increasing load. In contrast to the tensile behavior, the loss in stiffness under compressive loads was probably the result of increasing curvature at the fabric's warp/weft cross-over points.

As noted earlier, Coupon B was used for the compression tests that generated the information presented above. To validate that Coupon B produced acceptable compressive strength data, six monotonic compressive tests (see Table VII for data) were conducted at room temperature utilizing the Wyoming Modified Celanese Fixture. The average ultimate strength obtained using this fixture was –668 MPa (–96.8 ksi) with a standard deviation of ±46.5 MPa (±6.78 ksi). Test results from the Celanese fixture showed
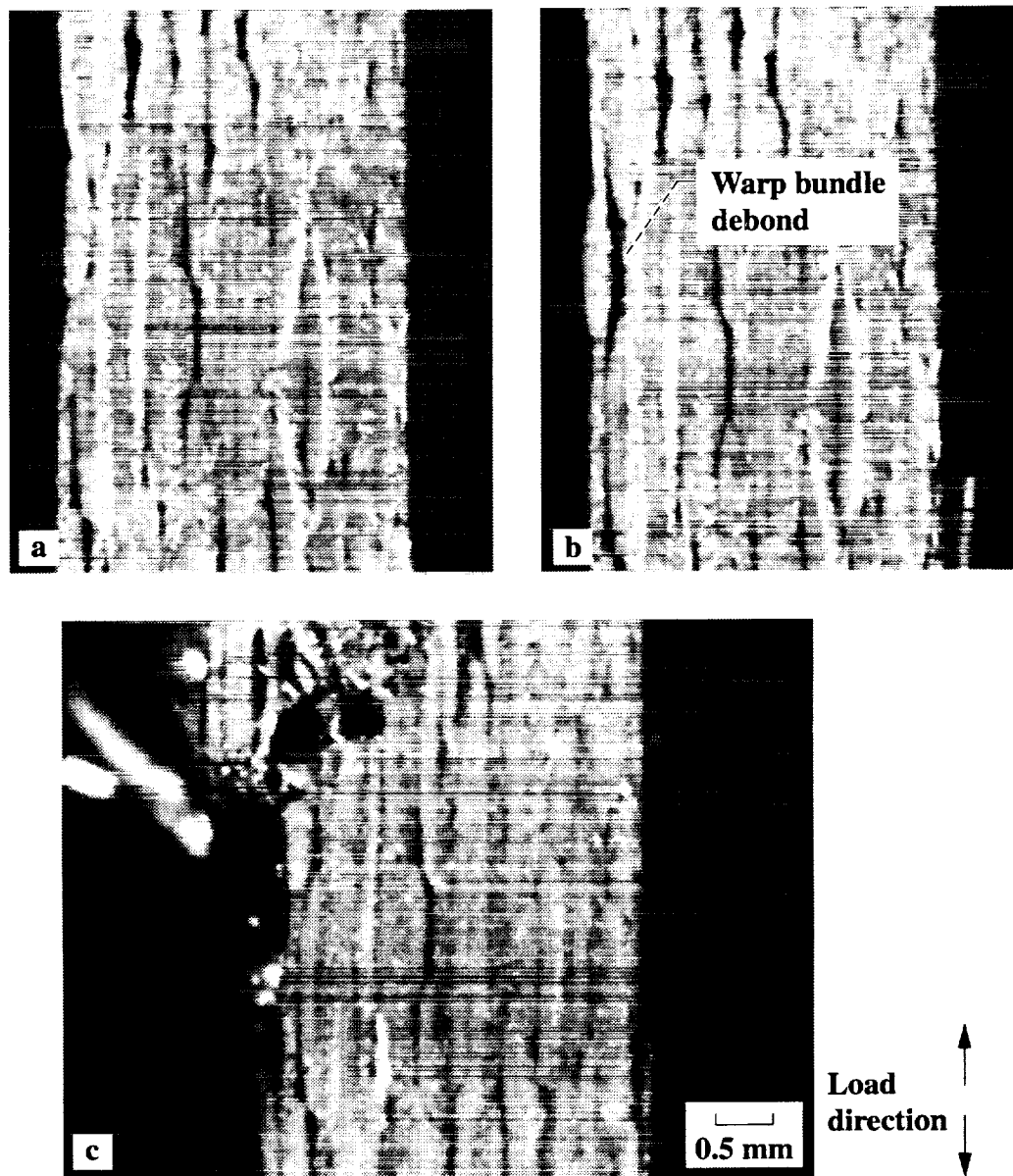
Figure 3.6 Progressive damage in 316 °C (600 °F) tensile specimen as observed using video images of monitored edge view with 15x magnification. (a) Image taken at 345 MPa (50 ksi) before transverse crack bundle debond. (b) Bundle debond at 414 MPa (60 ksi). (c) Failure at 848 MPa (123 ksi) initiated at bundle debond: Specimen P1_21.

TABLE V. COMPRESSIVE TEST RESULTS FOR 16-PLY
T650-35/PMR15 (0/90) WEAVE AT 22°C (72°F)

Specimen ID	$E_{tensile\ RT}$, GPa (Msi)	$E_{comp\ RT}$, GPa (Msi)	$\sigma_{comp.\ ult}$, MPa (ksi)	$\varepsilon_{comp.\ ult}$, %
PC1_1	70.3 (10.2)	64.3 (9.3)	-672 (-97.6)	-1.09
PC1_6	77.9 (11.3)	71.0 (10.3)	-675 (-97.9)	-1.10
PC3_30	75.2 (10.9)	70.3 (10.2)	-669 (-97.0)	-1.11
PC2_8	72.4 (10.5)	67.2 (9.8)	-681 (-98.8)	-1.19
Average	74.0 (10.7)	68.2 (9.9)	-675 (-97.8)	-1.12
Stnd Dev	3.36 (0.488)	3.07 (0.446)	5.21 (0.756)	0.0457

TABLE VI. COMPRESSIVE TEST RESULTS FOR 16-PLY
T650-35/PMR15 (0/90) WEAVE AT 316°C (600°F)

Specimen ID	$E_{tensile\ RT}$, GPa (Msi)	$E_{comp\ RT}$, GPa (Msi)	$E_{tensile\ ET}$, GPa (Msi)	$E_{comp\ ET}$, GPa (Msi)	$\sigma_{comp\ ult}$, MPa (ksi)	$\varepsilon_{comp\ ult}$, %
PC2_29	74.5 (10.8)	69.1 (10.0)	73.4 (10.7)	68.4 (9.9)	-631 (-91.5)	-1.08
PC2_18	71.7 (10.4)	67.1 (9.7)	70.8 (10.3)	66.4 (9.6)	-623 (-90.3)	-1.05
PC3_26	74.5 (10.8)	69.2 (10.0)	73.6 (10.7)	68.9 (10.0)	-599 (-86.8)	-0.97
PC3_31	73.8 (10.7)	68.8 (10.0)	72.9 (10.6)	68.1 (9.9)	-663 (-96.1)	-1.04
Average	73.4 (10.6)	68.5 (9.9)	72.7 (10.5)	68.0 (9.9)	-629 (-91.2)	-1.04
Stnd Dev	1.28 (0.185)	0.977 (0.141)	1.28 (0.189)	1.08 (0.157)	26.4 (3.82)	0.0465

TABLE VII. COMPRESSIVE TEST RESULTS FOR 10-PLY
T650-35/PMR15 (0/90) WEAVE USING MODIFIED
CELANESE FIXTURE AT 22°C (72°)

Specimen ID	$\sigma_{comp.\ ult}$, MPa (ksi)
C1	-693 (-100.6)
C2	-652 (-94.6)
C3	-598 (-86.7)
C4	-703 (-102.0)
C5	-640 (-92.8)
C6	-723 (-104.9)
Average	-668 (-96.9)
Stnd Dev	46.5 (6.78)
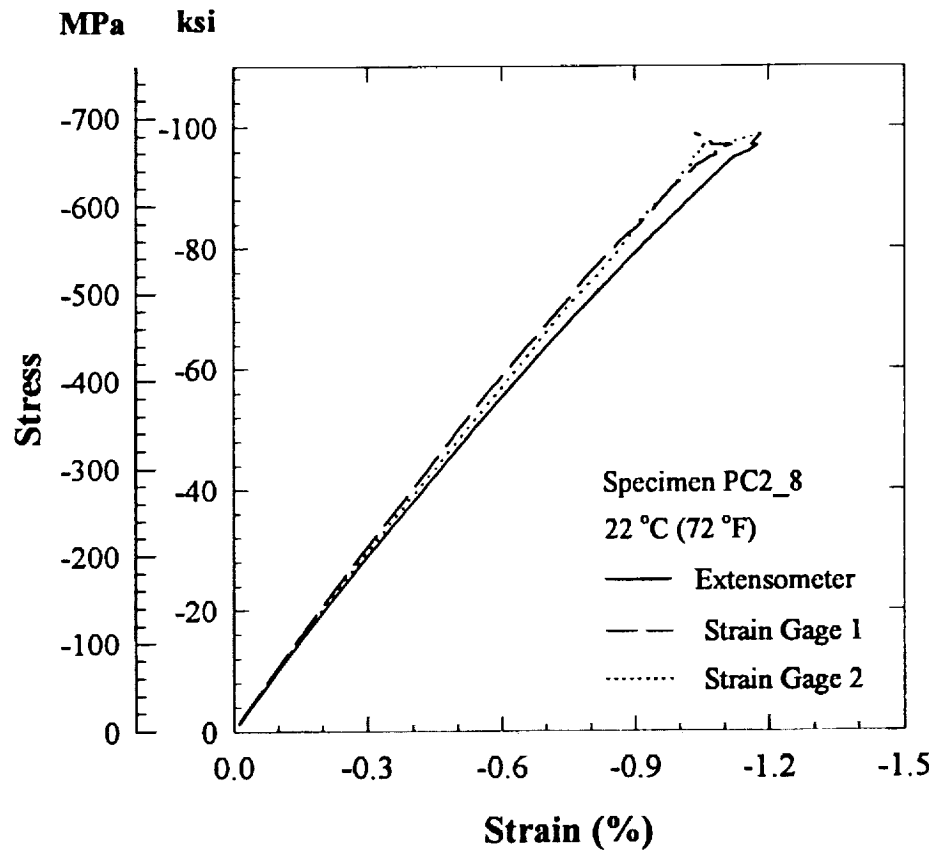
Figure 3.7 Typical monotonic compressive response of T650-35/PMR15 16-ply (0/90) weave at 22°C (72°F).
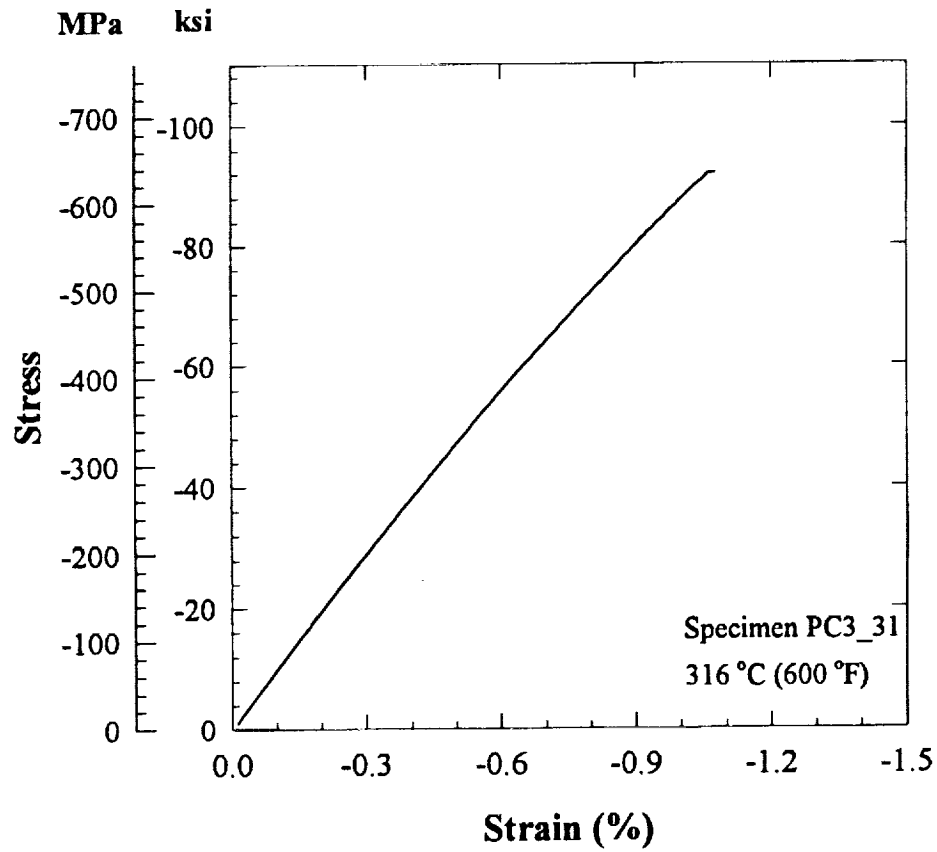
Figure 3.8 Typical monotonic compressive response of T650-35/PMR15 16-ply (0/90) weave at 316°C (600°F).

acceptable agreement with the Coupon **B** room temperature test results provided above. This is a strong indication that the data obtained using the Coupon **B** specimen geometry was reproducible.

3.5 Monotonic Compression - Microstructural Damage

At room temperature and elevated temperature, neither the destructive microscopy nor the edge view monitoring indicated any signs of microstructural damage prior to failure for monotonic compressive loading. Destructive sectioning was conducted on specimens exposed to stress levels as high as -580 MPa (-84 ksi). By viewing the edges of the specimens during the compressive tests, it was observed that the failures were instantaneous at both room and elevated temperatures. At 22 °C (72 °F) failure was likely the result of the simultaneous occurrence of massive bundle debonds and bundle buckling. The debonds were caused by the Poisson's induced out of plane tensile strain. Post-failure inspection indicated extensive bundle debonding, interlaminar delaminations, and warp bundle buckling. At 316 °C (600 °F), failure was again the likely result of fiber bundle debonds and fiber bundle buckling. Figure 3.9 displays a typical in-situ edge view at the point of failure for a test conducted at 316 °C (600 °F). The elevated temperature post-failure analysis showed fewer delaminations and somewhat more resin shear damage than room temperature analysis. The shear damage is identified as the large cracks oriented at 45° in respect to the load axis. Typical post-failure stereo microscope views of room and elevated temperature specimens are shown in Figure 3.10. Apparent in the edge views are the massive delaminations and the fracture of bundles due to buckling.

3.6 Isothermal Fatigue Life - Results

A summary of the isothermal fatigue life behavior is presented in Tables VIII (room temperature) and IX (elevated temperature). The data from both tables appear in a graphical format in Figure 3.11. Note that for all the cyclic fatigue data discussed here, the stress
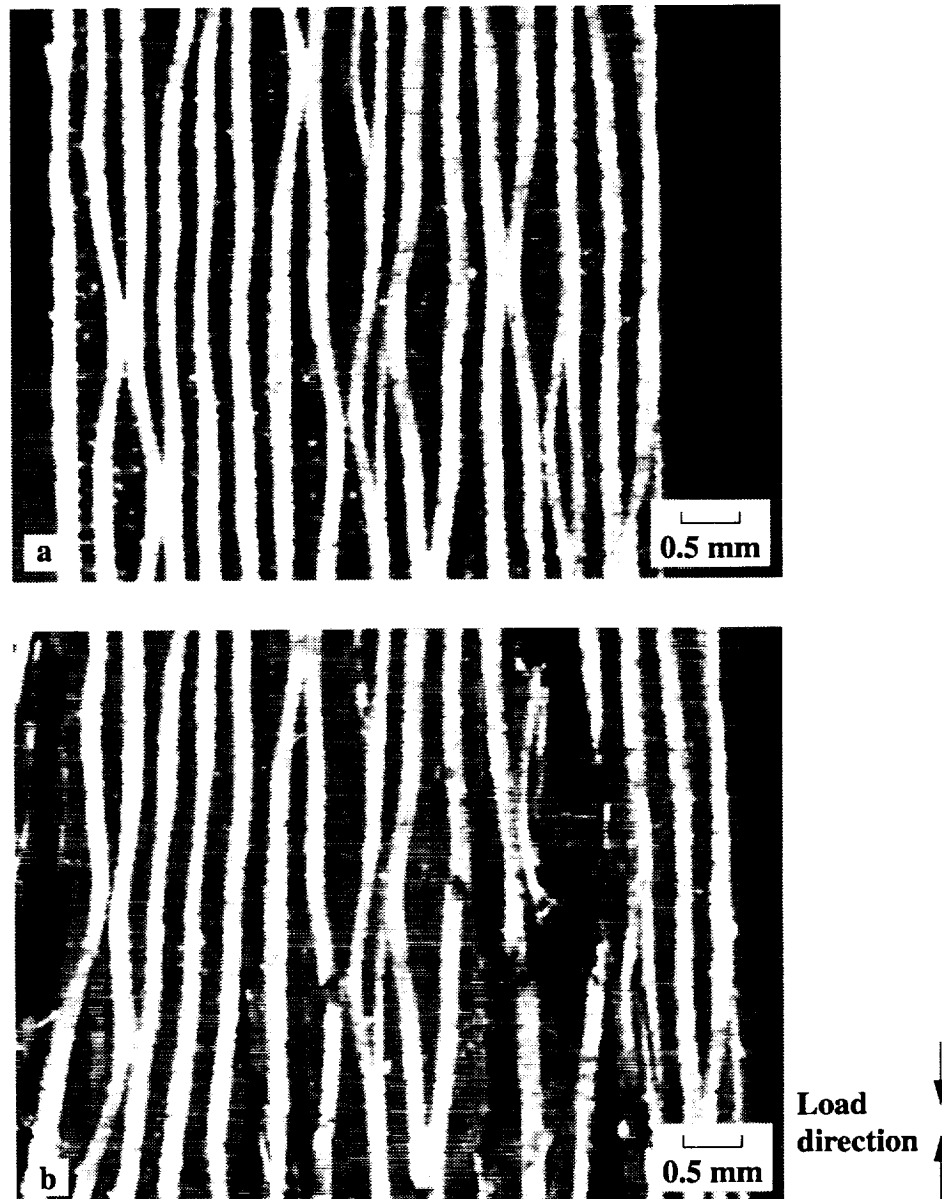
Figure 3.9 Monotonic compressive coupon at 316 °C (600 °F) as observed using video images of monitored edge view with 15x magnification. (a) Image taken at –593 MPa (–86 ksi); the instant before failure. (b) Failure at –599 MPa (–87 ksi): Specimen PC3_26.

Load direction
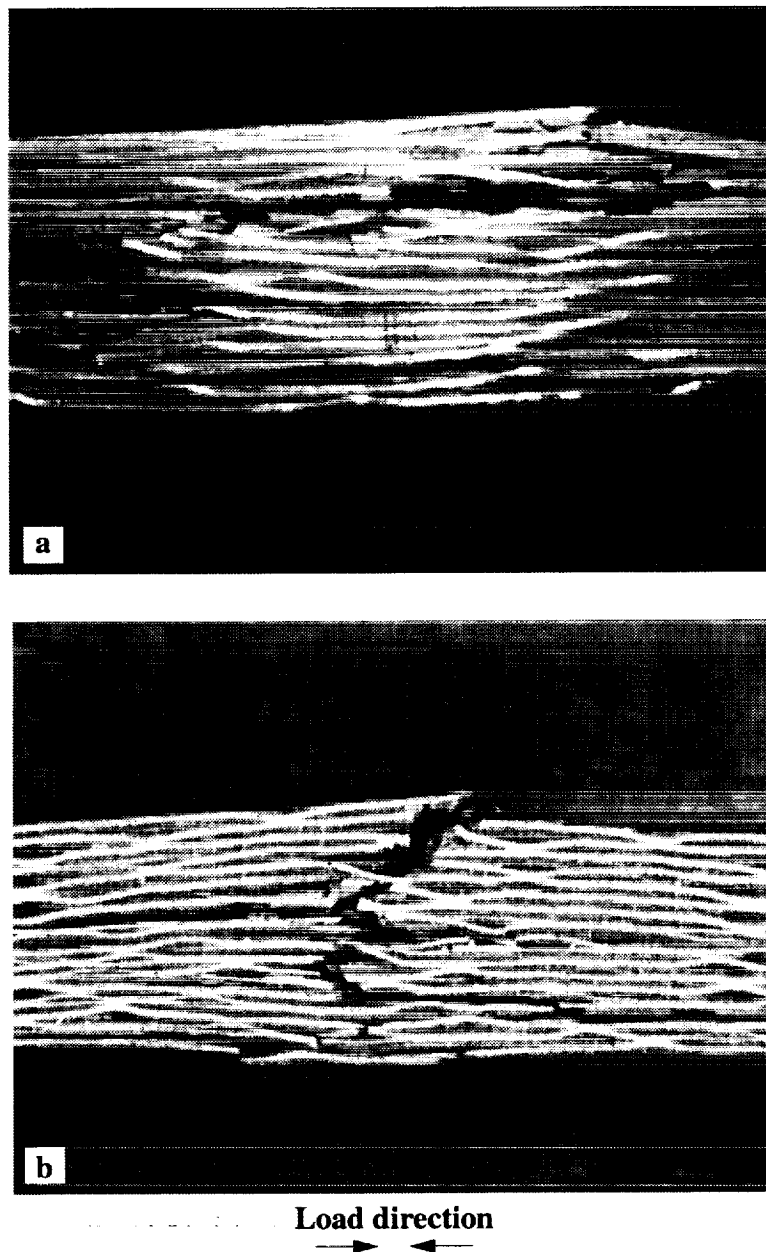
Figure 3.10 Typical post-failure edge views of compressive
specimens at 7.5x magnification. (a) 22 °C (72 °F): Specimen
PC1_3. (b) 316 °C (600 °F): Specimen PC3_15.

TABLE VIII. FATIGUE RESULTS FOR T650-35/PMR15 (0/90) WEAVE AT 22°C (72°F)

Specimen ID	σ_{max}, MPa (ksi)	$E_{ten\ RT\ init}$, GPa (Msi)	$E_{comp\ RT\ init}$, GPa (Msi)	Cycles to failure, N_f
PC2_1	483 (70)	73.0 (10.6)	69.7 (10.1)	100
PC3_32	414 (60)	74.6 (10.8)	71.0 (10.3)	2426
PC2_30	379 (55)	69.8 (10.1)	66.3 (9.6)	3552
PC3_17	379 (55)	69.9 (10.1)	66.8 (9.7)	3721
PC2_24	379 (55)	72.6 (10.5)	69.3 (10.1)	8429
PC2_6	345 (50)	71.8 (10.4)	68.7 (10.0)	21804
PC3_7	345 (50)	72.1 (10.5)	68.8 (10.0)	24254
PC3_9	345 (50)	74.2 (10.8)	70.9 (10.3)	26884
PC2_13	310 (45)	74.9 (10.9)	71.8 (10.4)	160423
PC2_31	310 (45)	72.1 (10.5)	69.0 (10.0)	111245
PC2_32	310 (45)	68.1 (9.8)	65.5 (9.5)	61231
PC2_12	276 (40)	72.1 (10.5)	68.7 (10.0)	1367095

TABLE IX. FATIGUE RESULTS FOR T650-35/PMR15 (0/90) WEAVE AT 316°C (600°F)

Spec. ID	σ_{max}, MPa (ksi)	$E_{tensile\ ET\ init}$, GPa (Msi)	$E_{comp\ ET\ init}$, GPa (Msi)	Cycles to failure, N_f
PC2_15	379 (55)	70.6 (10.2)	67.5 (9.8)	141
PC3_19	379 (55)	67.3 (9.8)	64.7 (9.4)	74
PC3_22	379 (55)	72.6 (10.5)	69.3 (10.1)	259
PC2_23	345 (50)	69.0 (10.0)	66.3 (9.6)	103
PC3_4	345 (50)	71.2 (10.3)	68.3 (9.9)	466
PC2_11	345 (50)	73.9 (10.7)	70.6 (10.2)	492
PC2_28	310 (45)	68.2 (9.9)	65.5 (9.5)	5678
PC3_20	310 (45)	68.3 (9.9)	65.7 (9.5)	5140
PC1_4	310 (45)	71.3 (10.3)	68.1 (9.9)	7858
PC3_8	276 (40)	69.5 (10.1)	66.6 (9.7)	38164
PC2_5	276 (40)	70.4 (10.2)	67.5 (9.8)	33930
PC1_8	276 (40)	72.1 (10.5)	69.0 (10.0)	134100
PC2_16	241 (35)	72.8 (10.6)	69.5 (10.1)	432943
PC1_5	241 (35)	69.9 (10.1)	67.3 (9.8)	354440
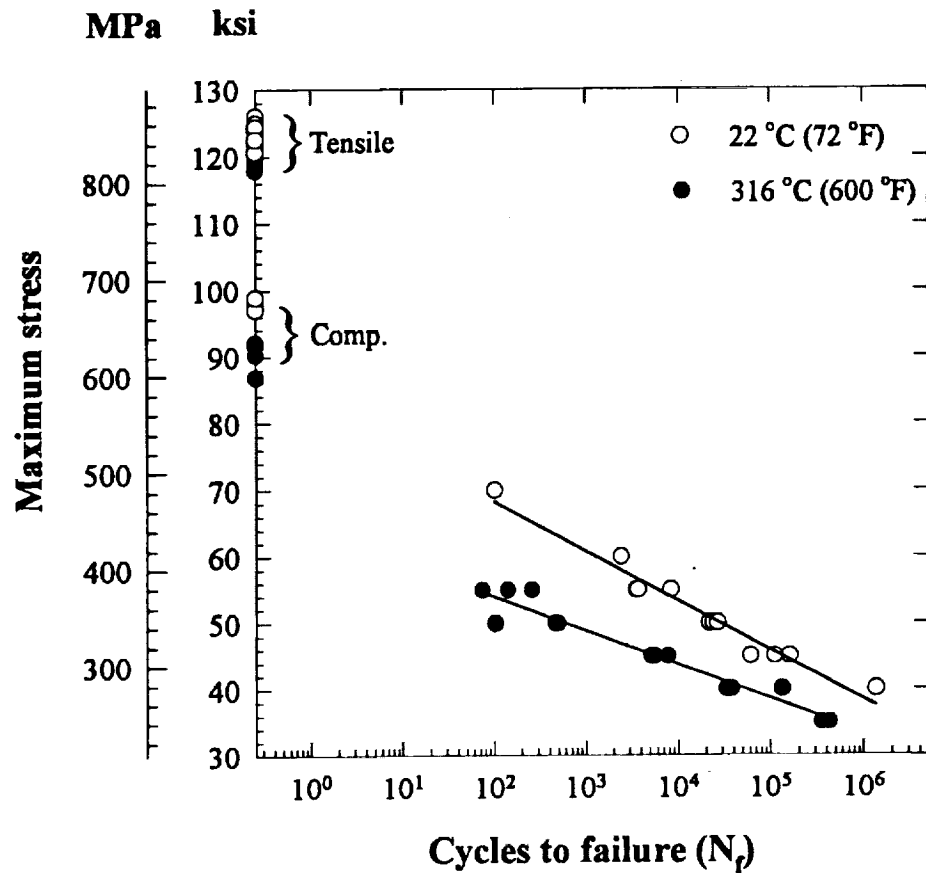
Figure 3.11 Stress based isothermal fatigue life comparison for T650-35/PMR15 (0/90) weaves at 22 and 316 °C (72 and 600 °F). Test conditions were R_σ=-1 and *Freq.*=2 Hz.

range ratio was $R_\sigma = -1$. The data in Figure 3.11 were generated by testing coupons at constant maximum cyclic stress levels ranging from 276 MPa (40 ksi) to 483 MPa (70 ksi) for room temperature data, and 241 MPa (35 ksi) to 379 MPa (55 ksi) for elevated temperature data. As a reference, the monotonic tensile and absolute monotonic compressive data appear in this figure along the vertical axis. The maximum cyclic stress levels produced lives ranging from 10^1 to over 10^6 cycles to failure for the room temperature data, and from 10^1 to over 10^5 cycles to failure for the elevated temperature data. The elevated temperature data showed a significant reduction in cycles to failure when compared to room temperature data tested at the same maximum stress level. For example, at the applied maximum stress of 345 MPa (50 ksi), the specimens exposed to room temperature had an average life 70 times greater than specimens exposed to elevated temperature (i.e., 24,314 versus 353 cycles to failure, N_f).

The fatigue data in Figure 3.11 are presented with a linear first order regression fit of the maximum cyclic stress versus log N_f data at each temperature. The standard form for the fatigue life, i.e.,

$$\sigma_{\max} = a + b \log N_f \tag{3.1}$$

is used in the regression analysis. The constants at room temperature were $a = 574.3$ MPa (83.3 ksi) and $b = -51.6$ MPa/cycle (-7.5 ksi/cycle). The constants at elevated temperature were $a = 443.3$ MPa (64.3 ksi) and $b = -35.5$ MPa/cycle (-5.1 ksi/cycle). Both temperatures displayed relatively steep slopes (see Figure 3.11). This is in contrast with typical tension-tension fatigue data for composites where the life curves are relatively flat and exhibit limited temperature dependence. This contrasting behavior is due to the increased influence of the resin during fully reversed fatigue. To underscore the issue that the resin plays a significant role in fatigue life for reversed loads, note that the final fracture event always occurred during the compressive portion of the cycle. This phenomenon is discussed in more detail in Section 3.8.

3.7 Elastic Moduli Degradation - Results

When subjected to the fully reversed cyclic fatigue, the macroscopic material response of the composite system changed constantly due to various microscopic damage mechanisms. Thus, macroscopic properties such as stiffness and residual compressive strength noticeably declined with accumulated cycles. Note that the constant change in residual compressive strength contrasts the reported behavior for residual tensile strength found in the literature for various composite systems. However, this section focuses on moduli degradation and compares the strain accumulation along with moduli degradation at the various maximum cyclic stress levels and temperatures. In the following section the initiation and progression of the different damage mechanisms which induced the degradation in both these engineering properties are presented. The residual compressive strength and its relationship with the current compressive modulus is discussed in the final two sections of this chapter.

Stress-strain curves at different accumulated fatigue cycles for both room and elevated temperatures are presented in Figures 3.12 and 3.13, respectively. These curves illustrate the progressive changes in deformation behavior up to the cycle prior to failure. Increased strain accumulations and moduli degradations are evident in both figures. Hysteresis was apparent at all stress levels, at both temperatures, and from the first cycle to the last. Hysteresis loops occurred even when there were no signs of observable damage or property degradation. However, hysteresis was not evident in the stress-strain curves obtained from the elastic moduli tests. The elastic moduli tests were conducted in the following manner. At predetermined intervals, the fatigue tests were suspended and the test specimen was unloaded. The current elastic moduli (tensile and compressive) of the specimen as a function of accumulated cycles were then obtained by applying relatively mild maximum stress levels of ±138 MPa (±20 ksi) (for more information concerning the periodic elastic moduli tests, the reader is advised to consult Section 2.5 of the previous chapter). Thus, at some cyclic stress level between 138 MPa (20 ksi) and 241 MPa (35 ksi) mechanisms leading to
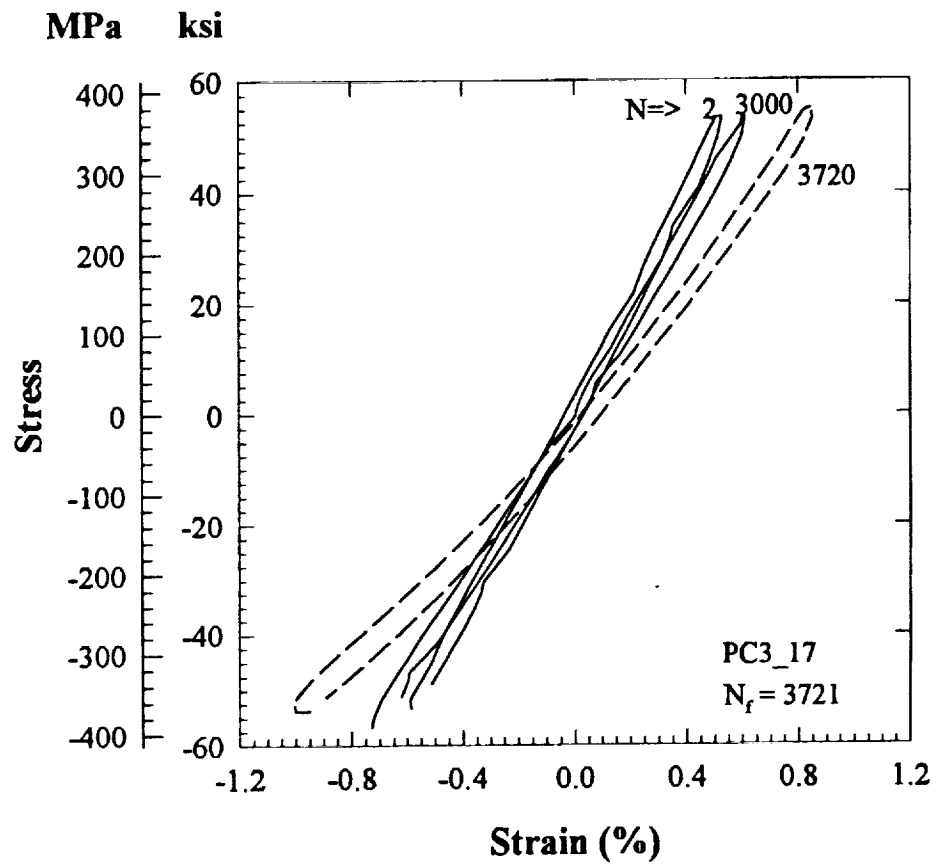
Figure 3.12 Fatigue deformation response of T650-35/PMR15 16-ply (0/90) weave at 22°C (72°F): σ_{max} = 379 MPa (55 ksi).
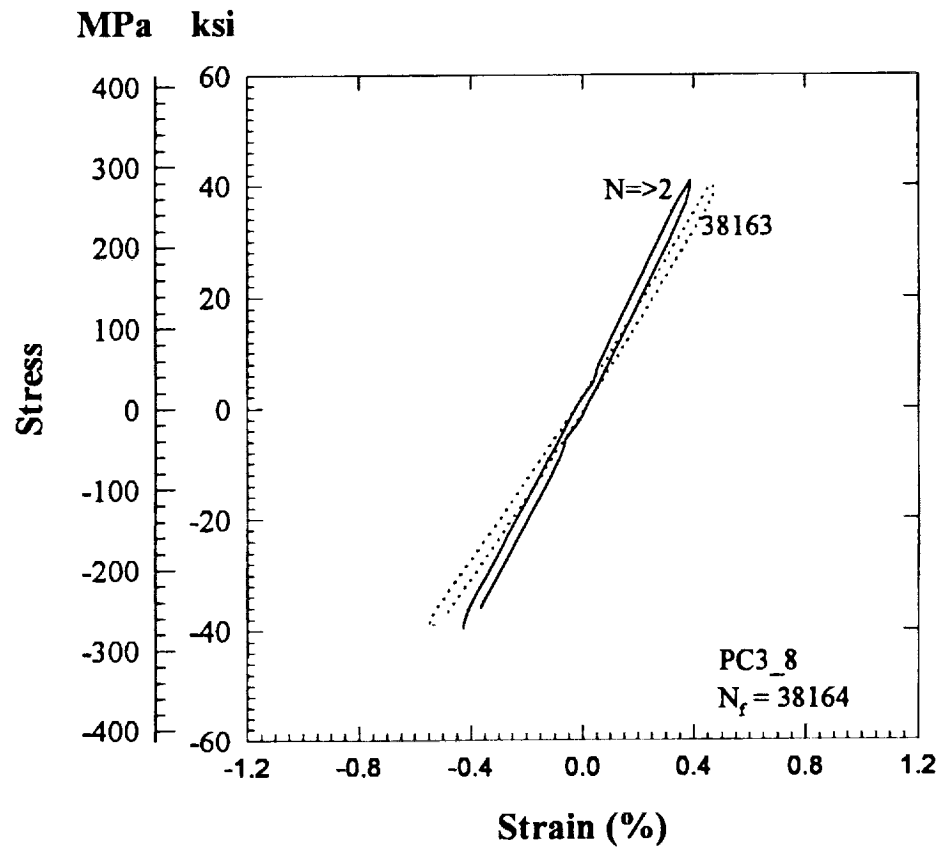
Figure 3.13 Fatigue deformation response of T650-35/PMR15 16-ply (0/90) weave at 316°C (600°F): $\sigma_{max} = 276$ MPa (40 ksi).

68

the observed hysteresis were initiated. It is presumed that during the tensile portion of a load cycle a locking mechanism occurred at the bundle crimp points. This locking effect was reversed under compressive loads, which in turn increased the curvature at the bundle cross-over points. It is surmised that non-observable damage, such as microcracks at the crimp points and inelastic deformation of the resin were likely occurring allowing the locking mechanism to relax.

Fatigue strain behavior and moduli degradation as a function of accumulated cycles are displayed in Figures 3.14 to 3.18. Data for both are presented for completeness. The plots in Figures 3.14 (room temperature) and 3.15 (elevated temperature) show the maximum and minimum strain as a function of accumulated cycles. Also, the strain value at zero stress (i.e., permanent offset strain) is shown in both figures. The strain at zero stress was plotted in order to indicate the presence of strain ratcheting. The strain value appearing in the figures was obtained by averaging the strain at zero stress during loading and the strain at zero stress during unloading. As seen in both figures, the average strain at zero stress was constant throughout the fatigue life. Thus, strain ratcheting did not occur. However, this is not unusual for a fully reversed cycle load regime where the mean stress is zero.

Figure 3.16 shows a typical comparison between the room temperature and elevated temperature compressive moduli (normalized with respect to the initial stiffness) for an equivalent maximum cyclic stress level. Notice that the normalized moduli degrade at the same rate, but the coupon tested at 316 °C (600 °F) failed much earlier than the coupon tested at room temperature. This artifact is incorporated into the analytical model discussed in the next chapter.

The three stage behavior of modulus degradation alluded to in Chapter I is apparent in Figures 3.16 to 3.18. The first damage stage (see Figure 3.16) occurred during the initial 1 percent of life. This was followed by a linear second stage (constant degradation rate) which constituted the majority of life. The second stage was quite pronounced for both the room temperature data (Figure 3.17) and the elevated temperature data (Figure 3.18). As failure
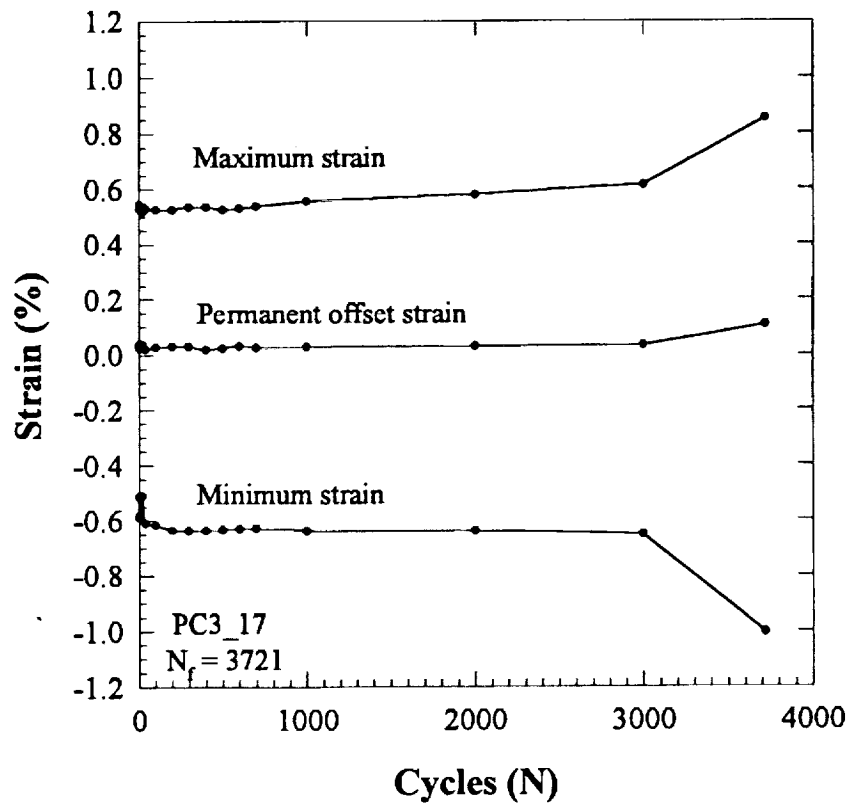
Figure 3.14 Fatigue strain behavior of T650-35/PMR15 (0/90) at 22°C (72°F): $\sigma_{max} = 379$ MPa (55 ksi).
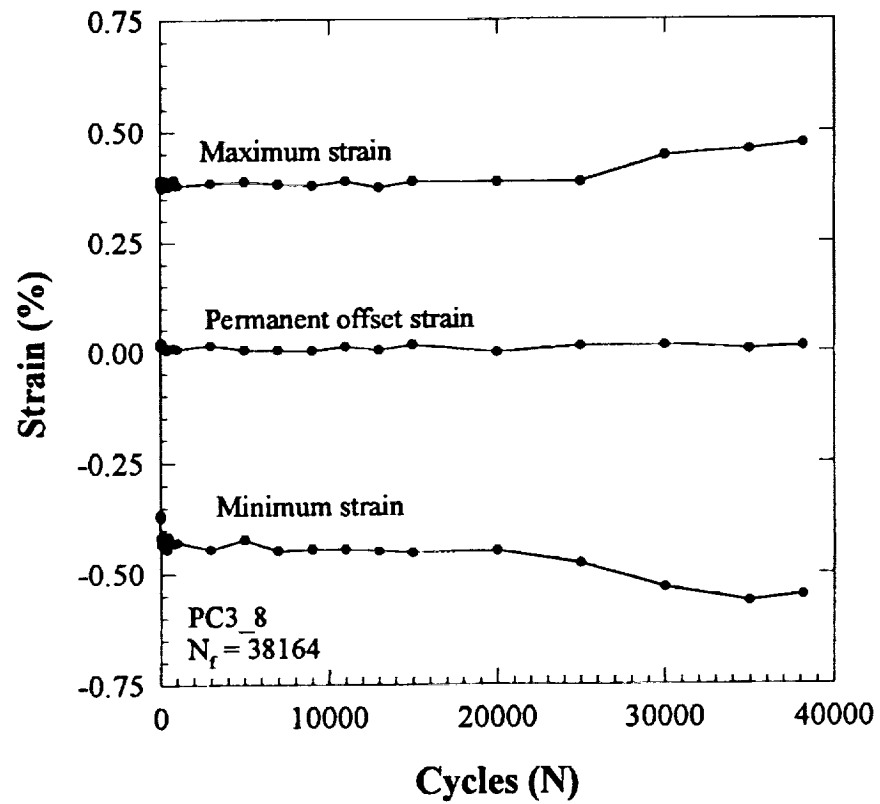
Figure 3.15 Fatigue strain behavior of T650-35/PMR15 (0/90) at 316°C (600°F) $\sigma_{max} = 276$ MPa (40 ksi).
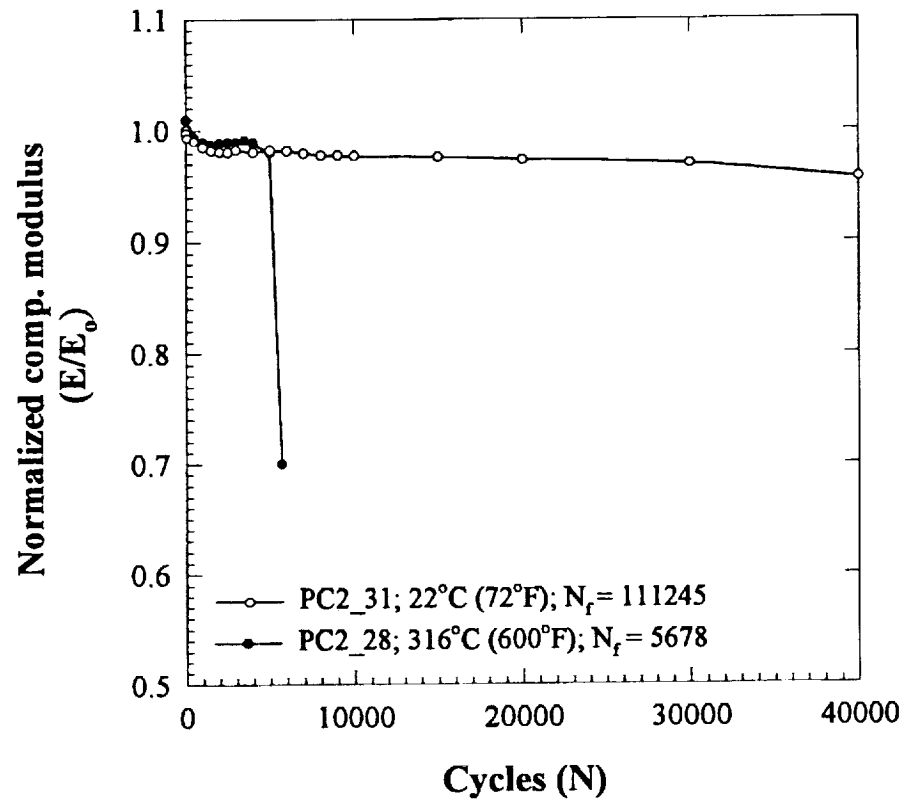
Figure 3.16 Comparison of modulus degradation behavior between 22°C (72°F) and 316°C (600°F) at an equivalent maximum stress: σ_{max} = 310 MPa (45 ksi).
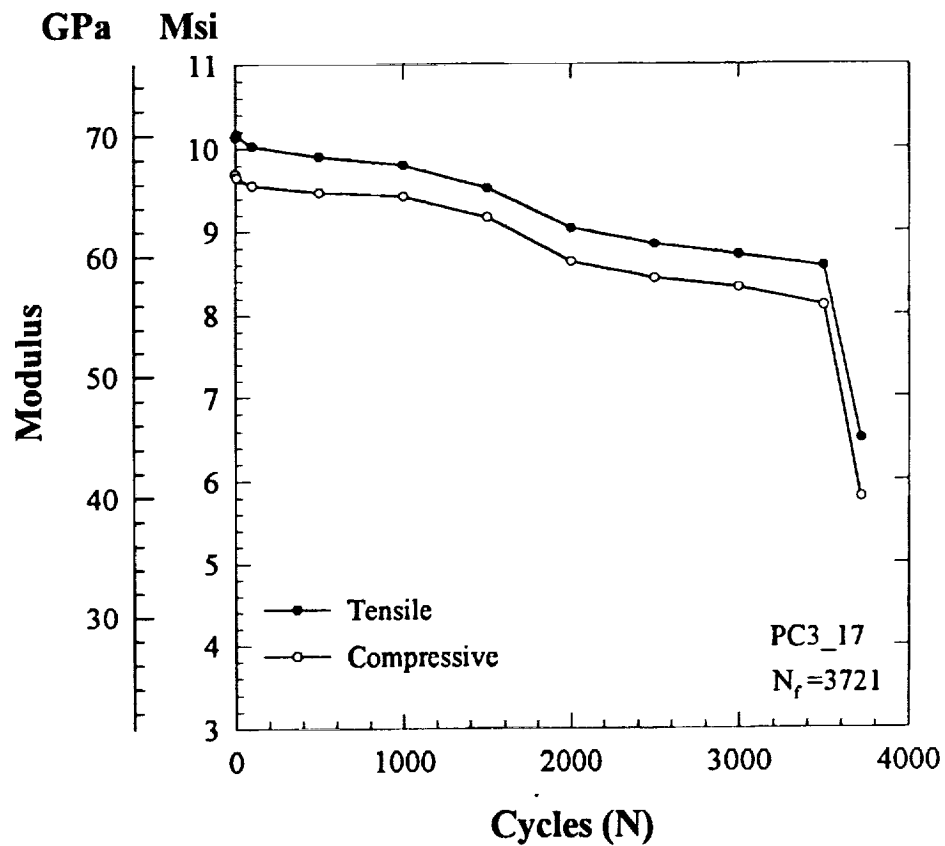
Figure 3.17 Typical degradation of tensile and compressive moduli during isothermal fatigue at 22°C (72°F): $\sigma_{max} = 379$ MPa (55 ksi).
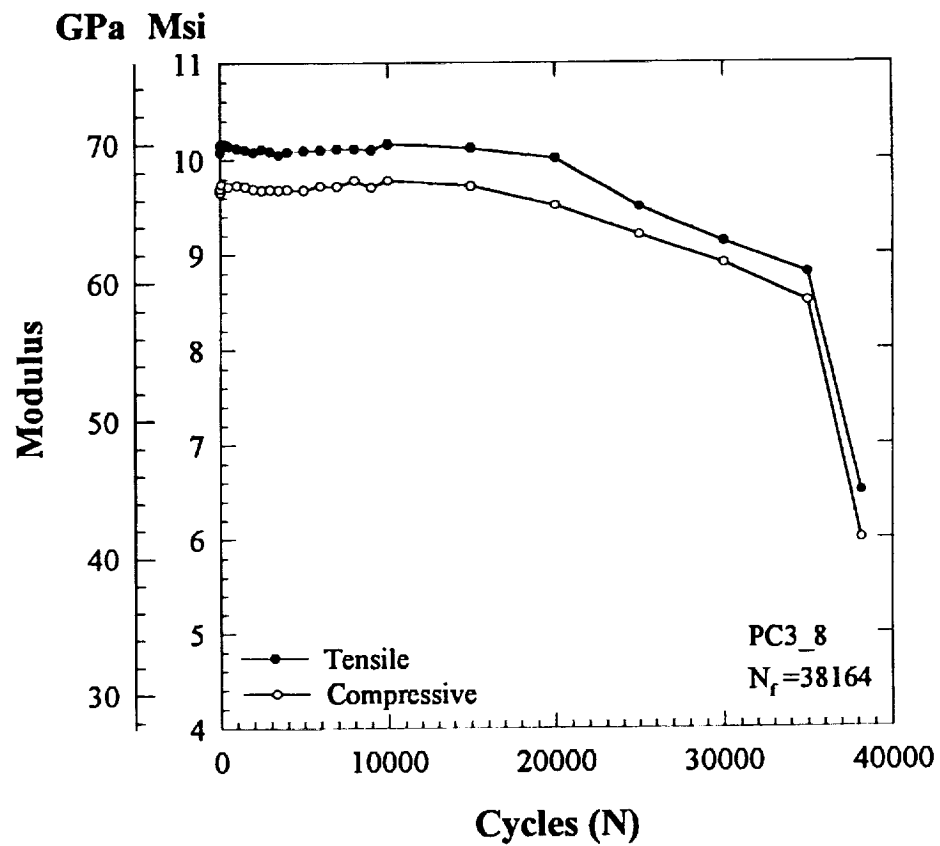
Figure 3.18 Typical degradation of tensile and compressive moduli during isothermal fatigue at 316°C (600°F): $\sigma_{max} = 276$ MPa (40 ksi).

approached, a dramatic increase in the damage rate occurred. This increased rate of damage was reflected in the sudden loss of moduli prior to failure. Note that similar degradation rates were observed for both tensile and compressive moduli. This indicated an equivalent sensitivity of stiffness to the various microscopic damage mechanisms in either load direction. Thus for the sake of brevity, even though data was collected on the degradation of both tensile and compressive moduli the description of stiffness degradation from this point forward will be limited to the compressive modulus. Note the discussion focuses on the compressive modulus because failure always occurred during the compressive segment of the cycle.

Figure 3.19 depicts room temperature data for compressive stiffness (normalized with respect to the initial stiffness) versus accumulated cycles (normalized in respect to cycles to failure, N_f) for three specimens at a single maximum cyclic stress level of 379 MPa (55 ksi). From the data presented in this figure, it is easily seen that normalized moduli as a function of normalized accumulated cycles is consistent from specimen to specimen, at a given temperature and stress level. Figure 3.20 depicts the average Stage II room temperature modulus degradation behavior at three stress levels as a function of accumulated cycles. The multiple curves were obtained by fitting a first order linear regression curve to the Stage II data obtained from three specimens tested at a particular maximum stress level. For example, at σ_{max} = 379 MPa (55 ksi) a regression curve was obtained from the Stage II data appearing in Figure 3.19. The average accumulated cycles were achieved by multiplying each specimen's normalized life by the average life of the three. It is clear from Figure 3.20 that the rate of degradation of the normalized stiffness as a function of accumulated cycles is dependent on the applied maximum cyclic stress at room temperature.

Figure 3.21 displays the normalized degradation data for three specimens at 316 °C (600 °F) with an applied maximum cyclic stress of 310 MPa (45 ksi). Modulus degradation behavior similar to room temperature data was seen at each of the maximum applied cyclic stress levels at this temperature. Again, Stage II dominated the life of the coupons. However,
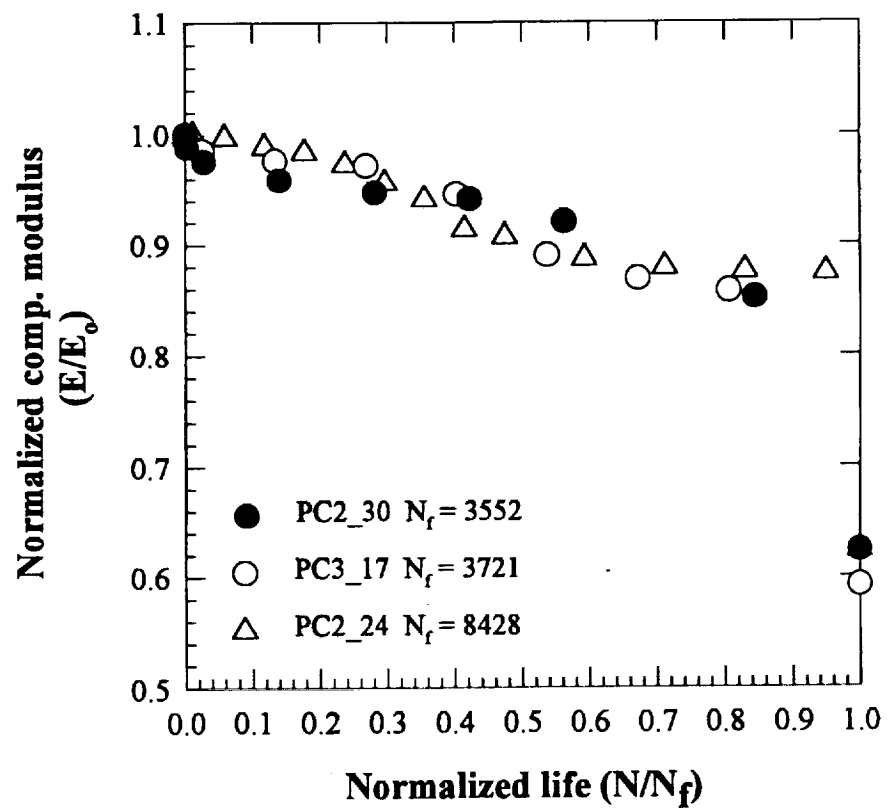
Figure 3.19 Normalized compressive modulus degradation behavior for multiple specimens at 22°C (72°F): σ_{max} = 379 MPa (55 ksi).
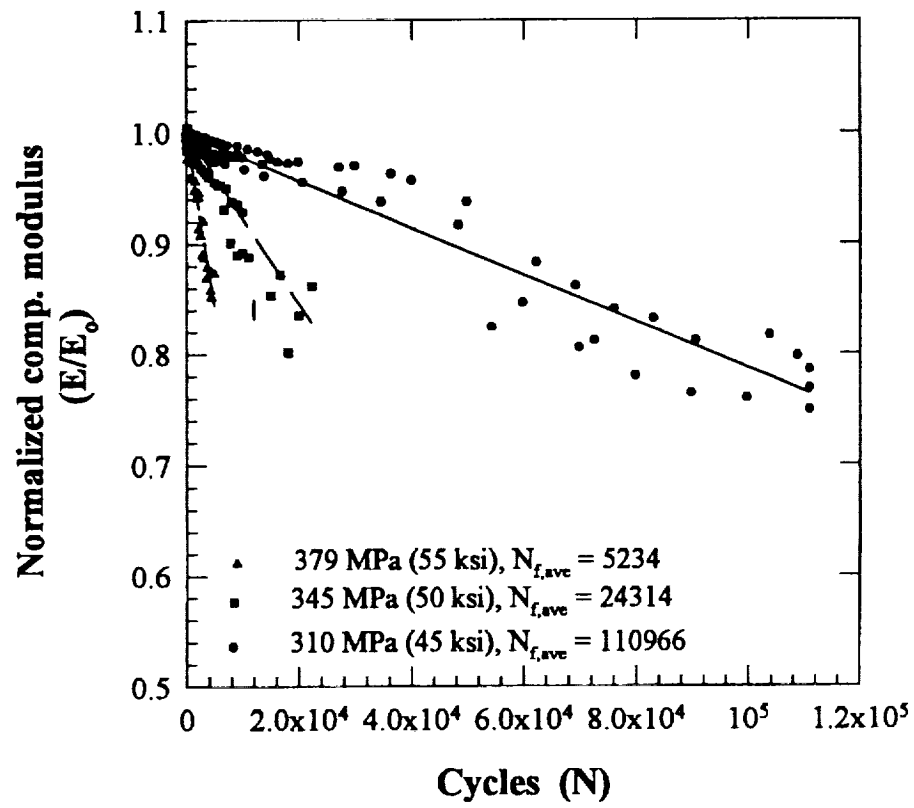
Figure 3.20 Normalized compressive modulus degradation behavior at various cyclic loads for 22°C (72°F) condition. For clarity, Stage III is not shown.
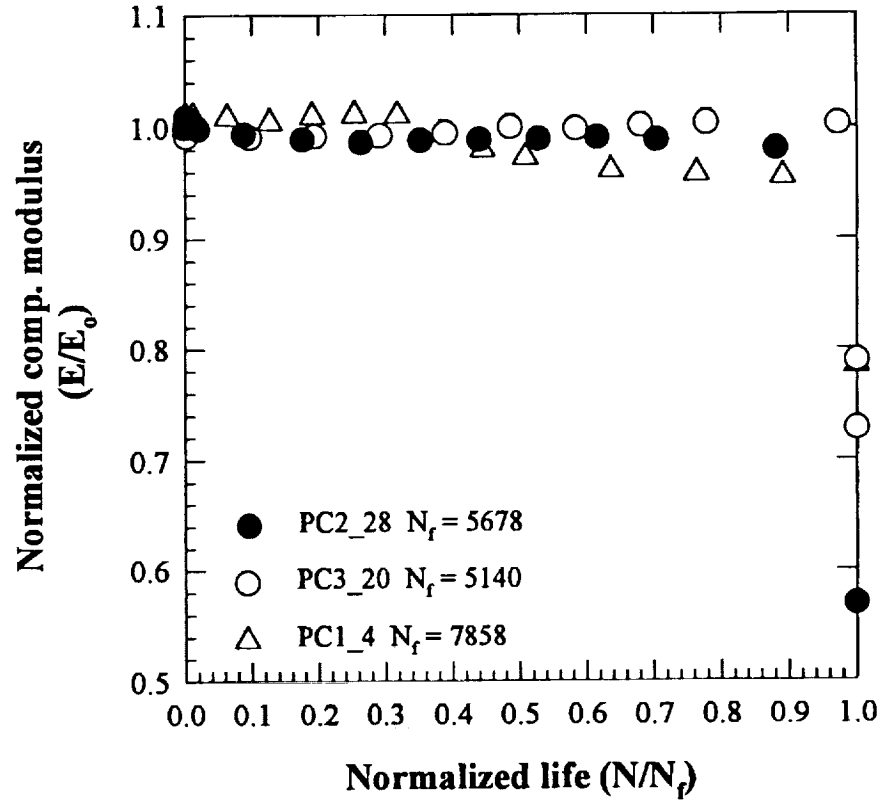
Figure 3.21 Normalized compressive modulus degradation behavior for multiple specimens at the 316°C (600°F): σ_{max} = 310 MPa (45 ksi).

the slope of the linear segments were relatively shallow in comparison to the room temperature data. Also, note in Figure 3.21 that a slight increase was observed in some specimens during the early segments of life. Both the occasional early increase and the relatively shallow Stage II were likely influenced by an increase in resin stiffness due to cross-linking of the resin molecules at elevated temperature. The reader is directed to Bowles et al. (1996) for further discussions on this issue. A figure showing elevated temperature compressive elastic modulus curves as a function of accumulated cycles (similar to the room temperature data of Figure 3.20) at various maximum cyclic stresses is not shown. This figure would appear extremely cluttered since the shallow slopes of each of the curves produced at the various maximum cyclic stress levels would tend to overlap one curve upon the other.

3.8 Isothermal Fatigue - Microstructural Damage

The observations of microstructural damage for both room temperature and elevated temperature are presented in this section. Certain maximum cyclic stress levels were selected for the interrupted tests. Specimens cycled at these stress levels were also subjected to the destructive examinations. For room temperature fatigue tests the pre-selected stress levels were 379.2 MPa (55 ksi) and 310.3 MPa (45 ksi). These stress levels corresponded to fatigue lives of 10^3 and 10^5, respectively. At these stress levels, tests were interrupted at cycles that corresponded to approximately 1, 5, and 10 percent degradation of the initial compressive modulus, E_o. Table X presents a representative summary of the microscopic damage sequence at 22 °C (72 °F). This sequence at room temperature was documented by both the in-situ edge view and the destructive examinations. Comparisons between the two cyclic stress levels at room temperature showed identical damage mechanisms. Therefore, micrographs in the following discussion are based only on the observations from the 379 MPa (55 ksi) maximum cyclic stress level.

At a 1 percent stiffness loss (208 cycles), a few transverse cracks were visible from the edge view in Figure 3.22 (view #2 - Figure 2.7). The transverse crack count was

TABLE X. FATIGUE DAMAGE SEQUENCE FOR
T650-35/PMR15 (0/90) WEAVE AT 22°C (72°F)

*Normalized compressive modulus, E/E_o	*Fraction of life, N/N_f	Damage event	Description
1.0	0.00	Transverse cracks	Transverse cracks occurred during the initial cycles and multiplied until saturation at $0.94E_o$ ($0.5N_f$). The cracks were equally distributed through the width and thickness.
0.93	0.50	Bundle debonds	Bundle debonds occurred after saturation of the transverse cracks. These events initiated and multiplied along specimen edges and continued to expand up to failure.
0.86	0.80	Interlaminar delaminations	Delaminations initiated from the transverse cracks and bundle debonds. Outer plies delaminated first followed by the inner plies. A few individual fiber fractures were seen at the transverse crack tips.
0.83	0.93	Bundle fractures	Bundle fracture due to buckling occurred first in the isolated debonded bundles along the edges of the coupon. Increased frequency of interior delaminations and interior bundle fractures resulted as failure approached. At this point a drastic increase in damage rate (i.e. stiffness loss) occurred. The specimen failed due to massive bundle debonds and bundle buckling in the remaining intact plies.

* Values taken at point of damage initiation.

Load direction

Figure 3.22 Edge view of transverse cracks as observed by microstructural examination of 22 °C (72 °F) specimen with 1% stiffness reduction (view #2; see Figure 2.7): 25x magnification: $\sigma_{max} = 379$ MPa (55 ksi); $N_{interrupt} = 208$; Specimen PC3_10.

0.9 cracks/cm·ply (2.2 cracks/in.·ply). No other forms of damage were apparent at this point in the fatigue life of the composite. Figure 3.23 displays the edge view (view #2) for a specimen with a 5 percent stiffness loss (3120 cycles). The transverse crack count increased to 15.9 cracks/cm·ply (40.5 cracks/in.·ply). In Figure 3.24, warp bundle debonds at the intersection of the specimen's edge and the transverse crack tips were evident. The transverse cracks had a homogeneous distribution throughout the thickness and width.

At an 11 percent stiffness reduction, the bundle debonds propagated and coalesced into interlaminar delaminations as is shown in Figure 3.25. Note the coupon had an 11 percent stiffness reduction as opposed to 10 percent stiffness reduction due to the fact that the elastic moduli tests were conducted at defined intervals as explained in Chapter II. Therefore, the fatigue tests were interrupted only after the latest elastic moduli results achieved the predetermined reduction in stiffness. The debonds were concentrated along the face and edge of the coupons and expanded through the thickness. The dark shaded areas indicated in the photo are polishing artifacts which are likely the result of loose, damaged material that was removed by the polishing cloth. Also, due to the lack of color in the photos the epoxy used to mount the sectioned views has the same shade as the PMR15 of the composite. Although there is an obvious difference in the color when viewed through the microscope, the contrast is lost in the black-and-white images presented here. At this level of damage accumulation, the transverse crack count was 15.1 cracks/cm·ply (38.5 cracks/in.·ply). Because the count did not increase in comparison to the crack count at 5 percent stiffness loss, it is likely that a saturation level was achieved. The delamination of the top ply can also be seen in this figure. These examinations clearly indicated that delaminations grew ply by ply through the thickness until final failure occurred. Although fractures of warp bundles were not yet seen at this point, a limited amount of individual fiber breaks were observed at the transverse crack tips. This phenomenon is indicated in the face view of Figure 3.26 (view #4 - see Figure 2.7). This view was obtained by polishing the face of the specimen until the tip of the transverse crack was seen. Figure 3.27 depicts the progressive

Load direction
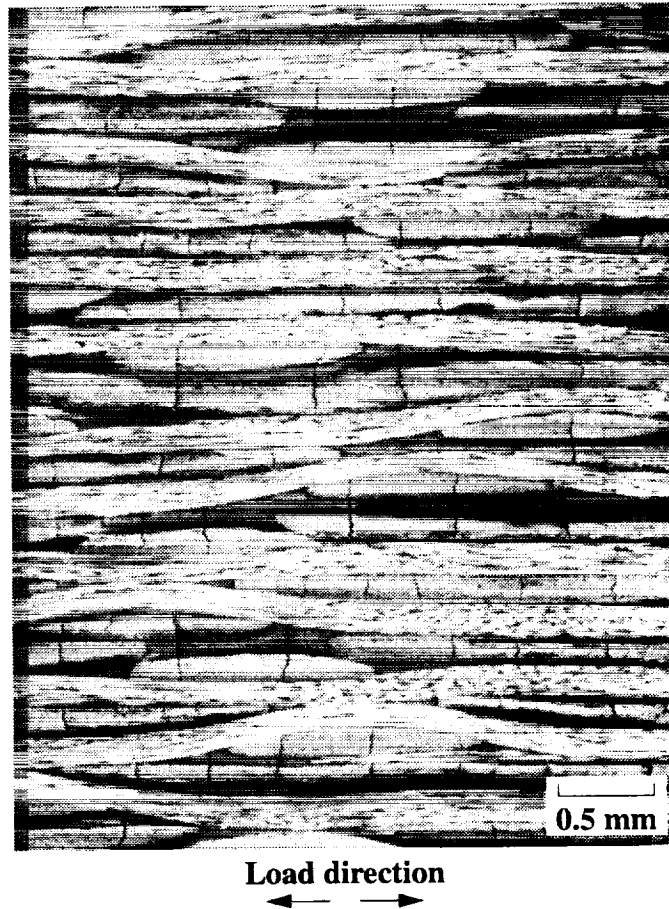
Figure 3.23 Edge view of transverse cracks as observed by microstructural examination of 22 °C (72 °F) specimen with 5% stiffness reduction (view #2; see Figure 2.7): 25x magnification; $\sigma_{max} = 379$ MPa (55 ksi); $N_{interrupt} = 3120$; Specimen PC2_10.

Figure 3.24 Edge view of transverse crack tip and initiation of bundle debond as observed by microstructural examination of 22 °C (72 °F) specimen with 5% stiffness reduction. (view #2; see Figure 2.7): 500x magnification; σ_{max} = 379 MPa (55 ksi); $N_{interrupt}$ = 3120; Specimen PC2_10.
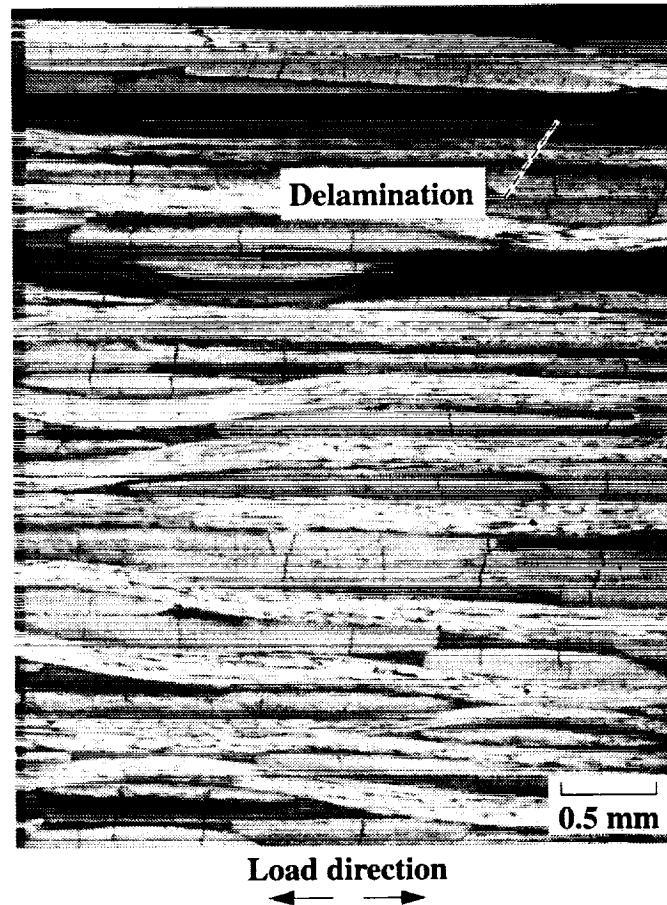
Figure 3.25 Edge view of transverse cracks and interply delamination as observed by microstructural examination of 22 °C (72 °F) specimen with 11% stiffness reduction. (view #2; see Figure 2.7): 25x magnification: σ_{max} = 379 MPa (55 ksi); $N_{interrupt}$ = 3010; Specimen PC3_25.
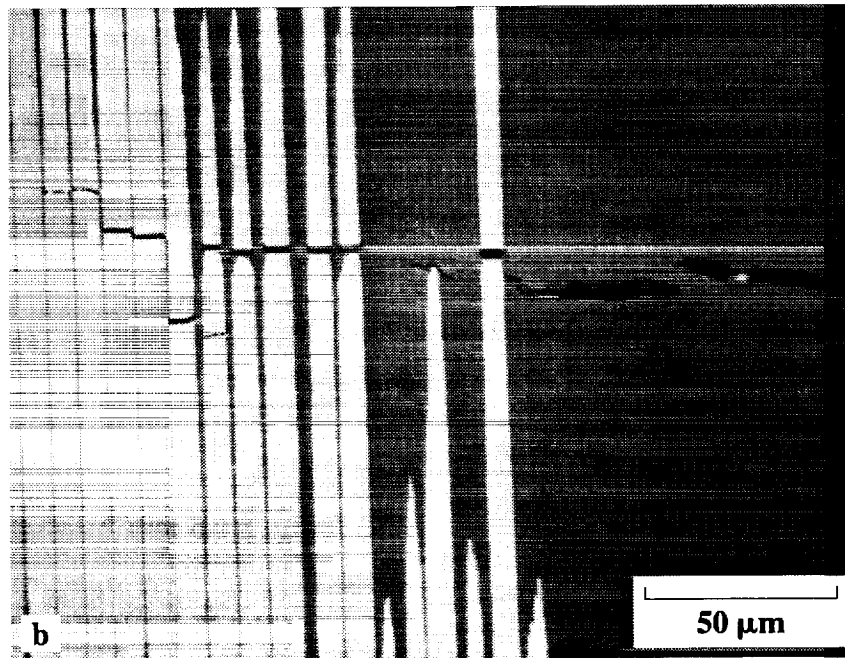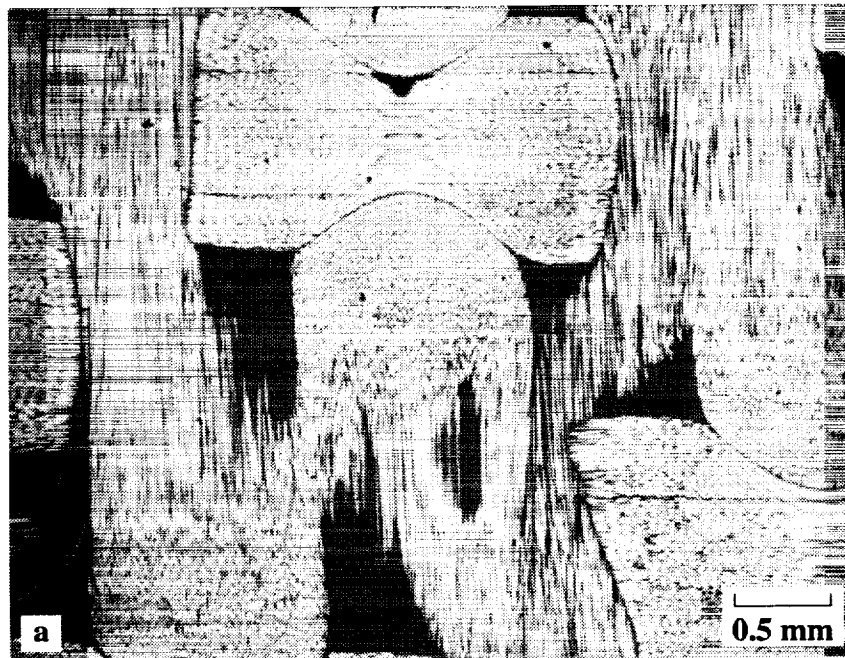
Figure 3.26 Transverse cracks as observed from the polished face of a 22 °C (72 °F) specimen with 11% stiffness reduction. (view #4; see Figure 2.7): (a) 25x magnification. (b) Showing fiber breaks at 500x magnification: σ_{max} = 379 MPa (55 ksi); $N_{interrupt}$ = 3010; Specimen PC3_25.
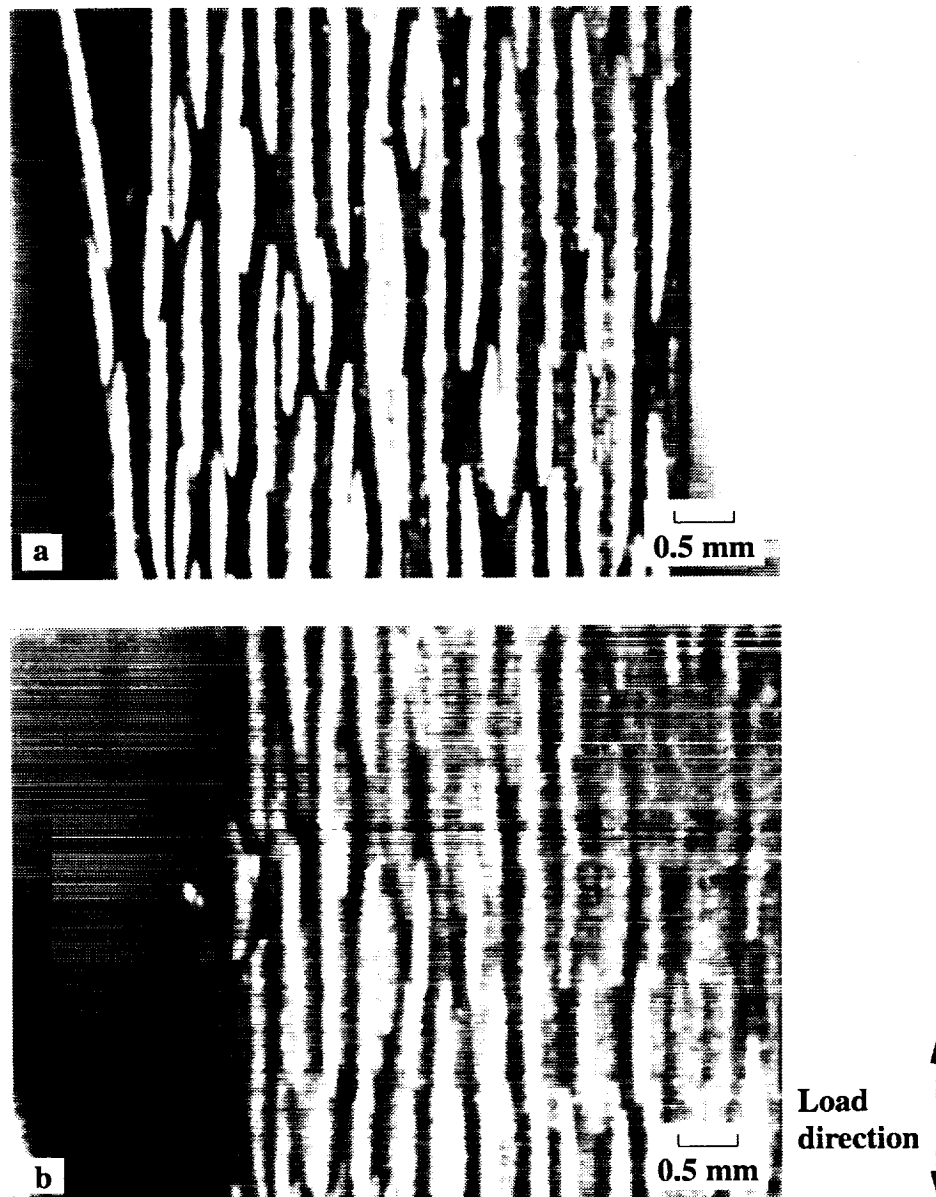
Figure 3.27 Damage progression as observed by in-situ edge view of 22 °C (72 °F) specimen at 15x magnification. (a) Delamination at cycle 1800. (b) Inward growth of delamination and buckling of isolated bundle at cycle 2300. (c) Failure in compression due to massive bundle debonding and buckling: $\sigma_{max} = 414$ MPa (60 ksi); Specimen PC3_32; $N_f = 2426$.
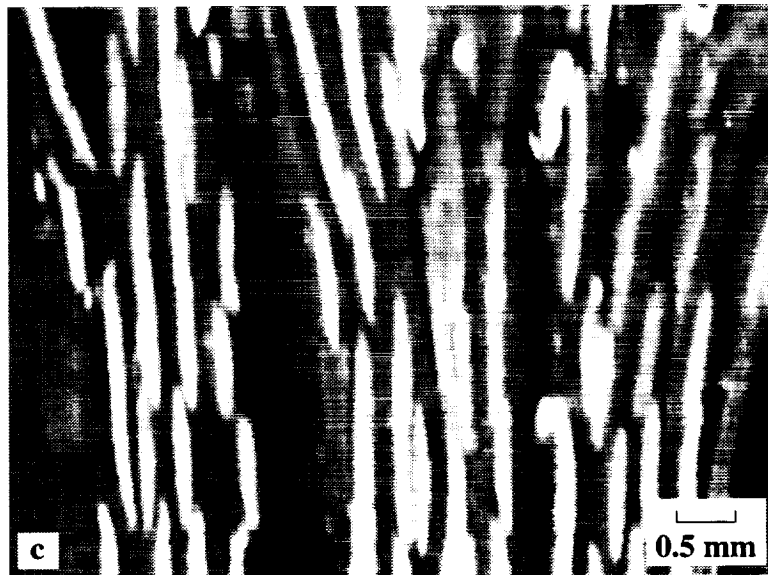
Figure 3.27 Continued.

growth of damage in a room temperature fatigue coupon. In this figure a succession of micrographs depict the inward (i.e., into the thickness) growth of delaminations, tow failures of exterior warp bundles due to buckling, and final failure. Final fracture was the result of massive debonds and delaminations in the intact interior plies. A post failure view is displayed in Figure 3.28. Throughout the life of the room temperature coupon the transverse crack counts showed equivalent distribution for both the near edge and the interior transverse views (views #2 and #3 - Figure 2.7).

At 316 °C (600 °F), the destructive examination was conducted at the maximum applied cyclic stress of 275.8 MPa (40 ksi). This applied cyclic stress yielded lives of approximately 10^4 cycles. Table XI displays a summary of the damage sequence at 316 °C (600 °F) as documented by both the in-situ edge view and the destructive examinations. The values in the table reflect averaged results.

No microscopic damage was observed in any of the sectioned views taken at a 1 percent stiffness reduction (100 cycles). However, the in-situ edge view showed initial bundle debonds and breaks occurred along the edge and face. The bundle debonds occurred within the first few cycles and progressed until failure. The damage level (i.e., the 1 percent decrease in the normalized stiffness) was maintained until a sufficient number of transverse cracks accumulated. The transverse cracks penetrated approximately one or two bundle widths from the edge. Figure 3.29 displays the penetration depth of the transverse cracks as seen from the face of sectioned specimen taken at a 5 percent stiffness reduction. At this current stiffness the crack count at the edge (view #2) was 5.9 cracks/cm·ply (15.0 cracks/in.·ply), while the interior of the specimen (view #3) showed no damage.

Interlaminar delaminations first appeared in the edge view when the composite reached a 4 percent stiffness reduction. Figure 3.30 depicts the warp bundle debonds along the face and edge (longitudinal load axis - view #1) of a sectioned specimen with a 5 perecnt stiffness loss. The final damage mechanisms, initiated at 5 percent stiffness reduction, were interply delaminations. At this point an increased rate of bundle fractures were occurring

Load direction
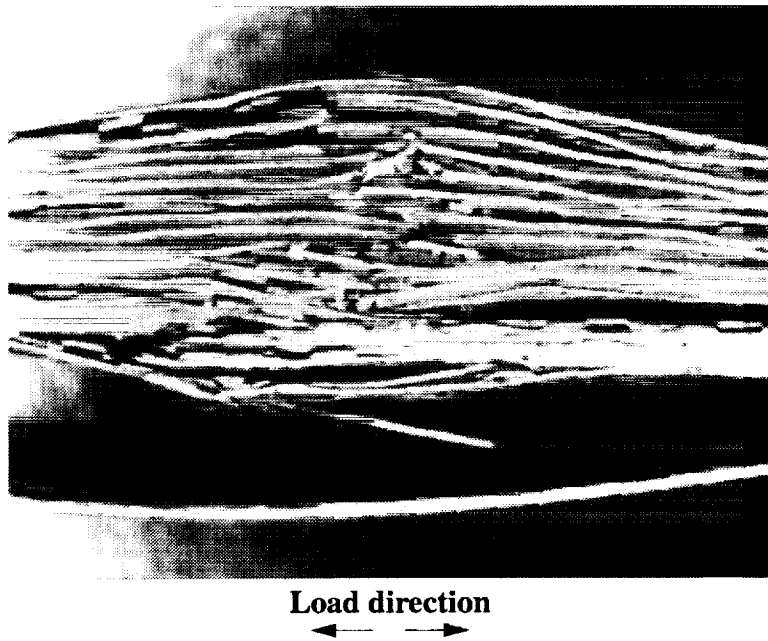
Figure 3.28 Post failure view of 22 °C (72 °F) specimen at 7.5x magnification. Specimen PC3_32.

TABLE XI. FATIGUE DAMAGE SEQUENCE FOR
T650-35/PMR15 (0/90) WEAVE AT 316°C (600°F)

*Normalized compressive modulus, E/E_o	*Fraction of life, N/N_f	Damage event	Description
0.99	0.34	Bundle Debonds	Bundle debonds and buckles occurred along the edge and the face without much penetration in to the interior of the specimen. The events were caused by edge effects and temperature. Because only the surface bundles were affected, modulus was minimally influenced.
0.99	0.42	Bundle breaks	The debonded bundles fractured due to buckling, but only along the edge and the face. Again, modulus was relatively unaffected.
0.98	0.88	Transverse cracks	Transverse cracks were apparent, although at much higher concentrations closer to the edge.
0.96	0.90	Interlaminar delaminations	Delaminations were initiated at the outermost layer. Progressive delaminations continued inward until specimen fracture due to a combination of massive bundle debonding and resin shear failure of remaining intact plies.

* Values taken at point of damage initiation.

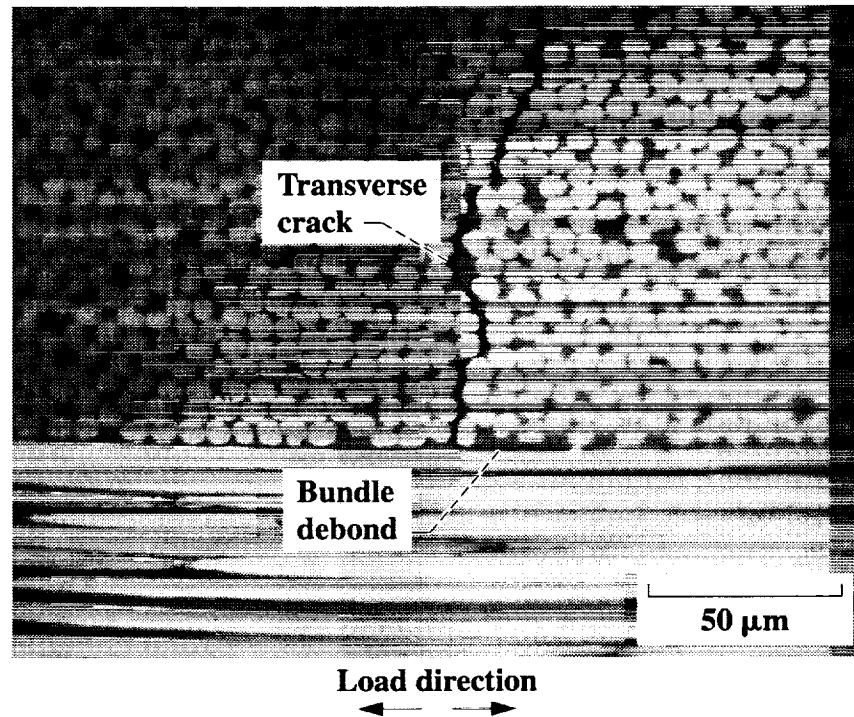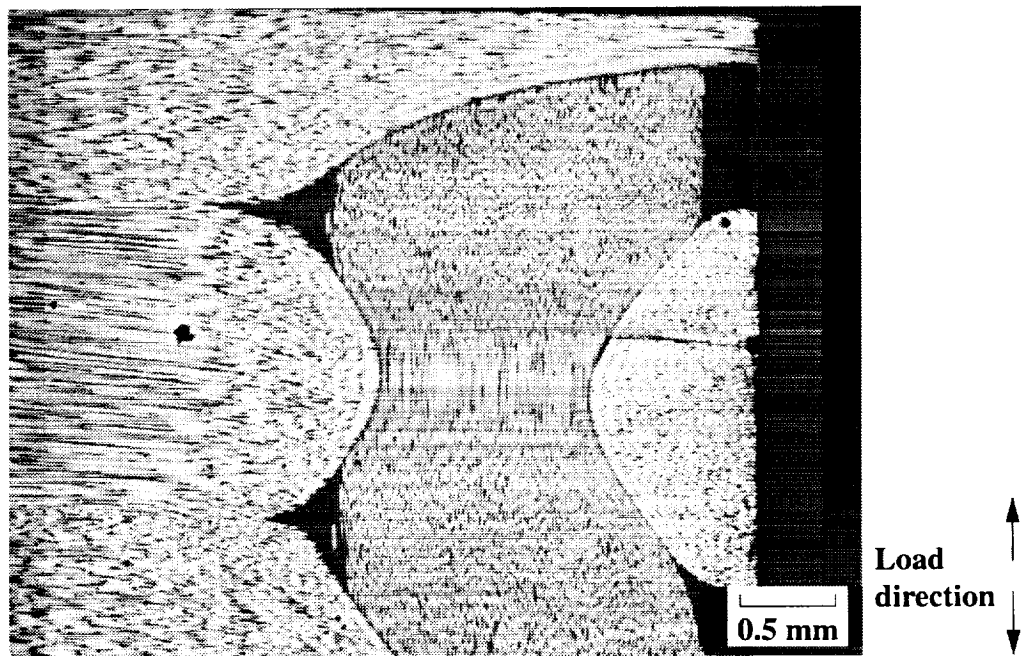**Figure 3.29** Face view showing penetration of transverse cracks as observed by microstructural examination of 316 °C (600 °F) specimen with 5% stiffness reduction. (view #4; see Figure 2.7): 25x magnification; σ_{max} = 276 MPa (40 ksi); $N_{interrupt}$ = 130000; Specimen PC4_4.

Load direction
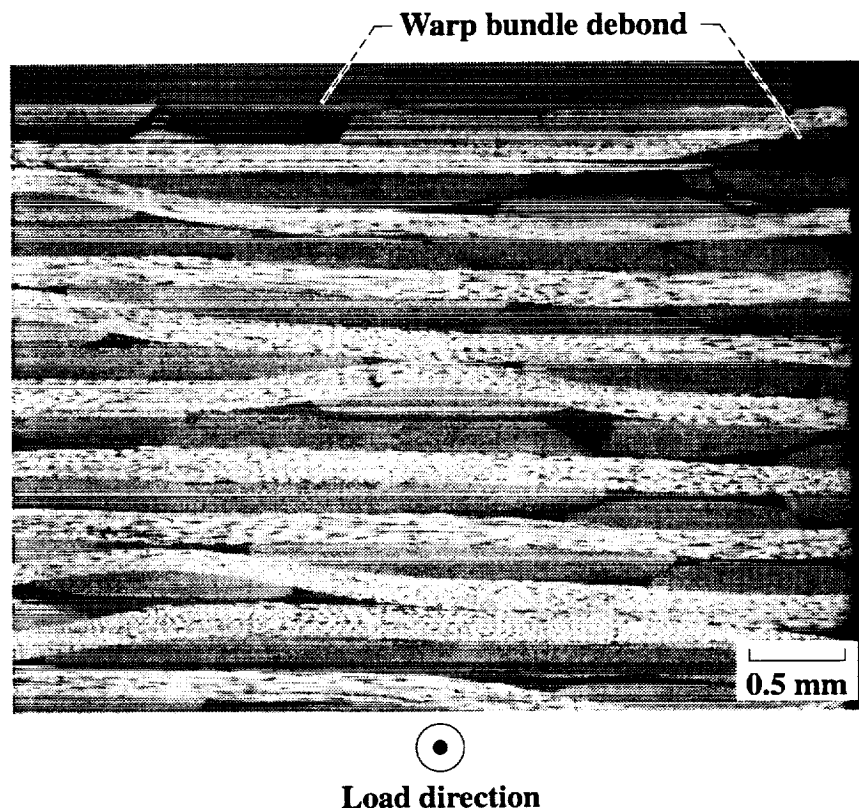
Figure 3.30 Bundle debonds along the face and edge at 25x magnification as seen from longitudinal loading axis (view #1) obtained from microstructural examination of 316 °C (600 °F) specimen with 5% stiffness reduction: $\sigma_{max} = 276$ MPa (40 ksi); $N_{interrupt} = 130000$; Specimen PC4_4.

due to buckling of the isolated bundles. All of these mechanisms initiated along the edge and face and then proceeded to propagate towards the midplane of the laminate. This indicated the start of Stage III (i.e., the drastic increase in degradation rate) behavior of the modulus curve. Failure occurred when the out-of-plane strain in the remaining intact plies caused massive debonding, delaminations, and bundle buckles. Figure 3.31 shows the sequence of events leading to failure observed by the in-situ edge view video. The above failure mechanisms are depicted in the post failure view presented in Figure 3.32.

3.9 Edge Effects

Because delaminations were observed in the woven coupons at both temperatures, the issue of out of plane stresses as a result of free edge effects needs to be discussed. The majority of the references in the following discussion are concerned with non-woven laminates. An attempt is made to use the available data for non-woven tape laminates to compliment the limited amount of data in the literature pertaining to edge effects in 2-D woven laminates. In such a way, a reasonable explanation can be put forth concerning the influence of edge effects on the initiation and progression of microscopic damage in woven coupons.

A boundary layer exists near the free edges of multidirectional tape (nonwoven) laminates where the state of stress may be three-dimensional. There are two mechanisms which induce the complex stress states at the free edges of these tape laminates. The first involves interlaminar stress transfer (as in the case of $\pm\theta$ angle-ply tape laminates) while the second mechanism entails the Poisson's mismatch of laminae (as in a (0/90) tape lay-up). The important feature of the of the angle plies is the mismatch of the shear coupling coefficients between the $\pm\theta$ layers. Classical laminate theory (pertaining to tape laminates) shows this mismatch to induce shear stresses opposite in sign in each of the $\pm\theta$ layers. Kedward and Whitney (1990) eloquently reassured that at free edges the shear stresses cannot exist. Thus, near free edges of the plies, shear strains are compensated for by the interlaminar shear
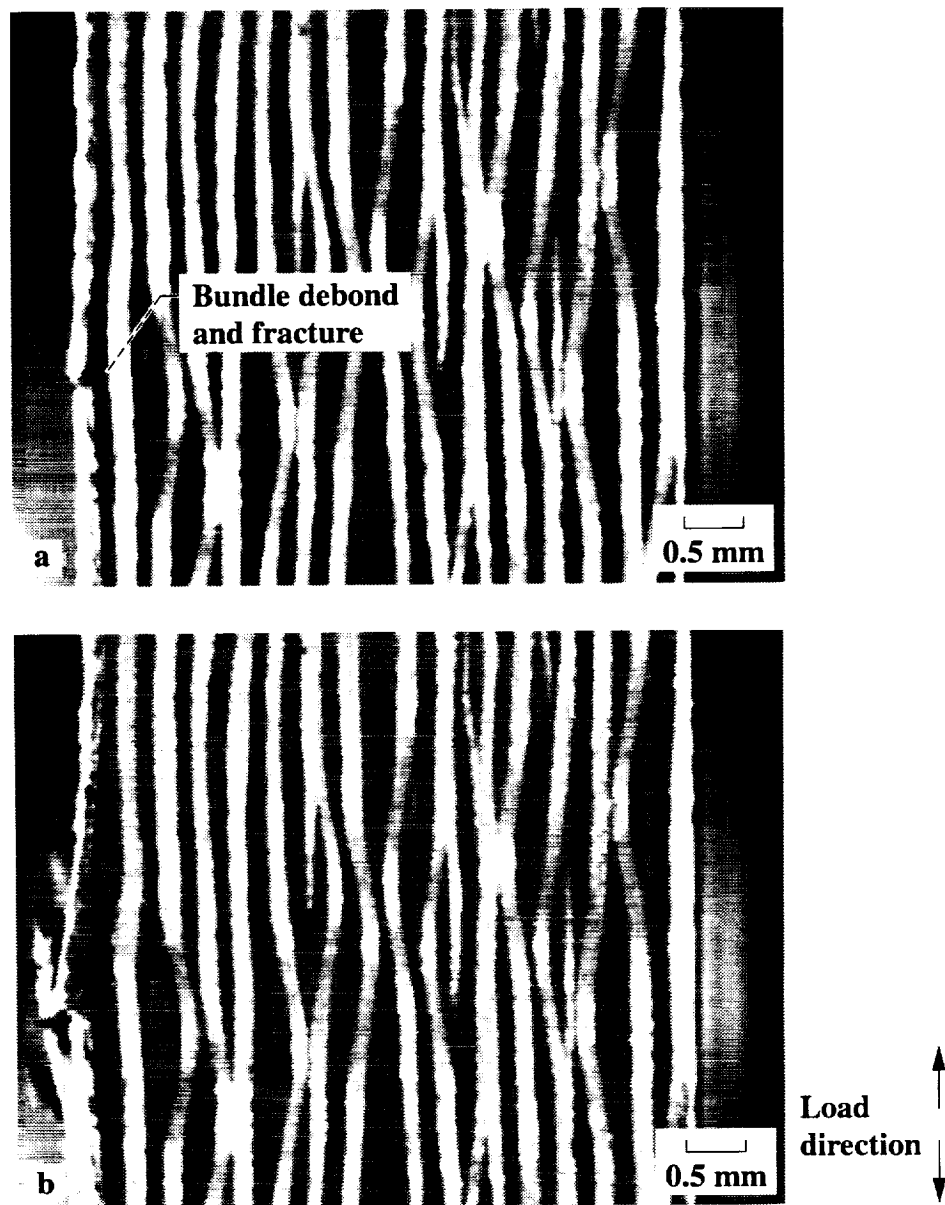
Figure 3.31 Damage progression as observed by in-situ edge view of 316 °C (600 °F) specimen at 15x magnification. (a) Warp bundle debond and fracture due to buckling at cycle 3200. (b) Interply delamination and inward growth of debonds at cycle 7200. (c) Failure due to massive bundle debonding and buckling: σ_{max} = 310 MPa (45 ksi); Specimen PC1_4; N_f = 7858.
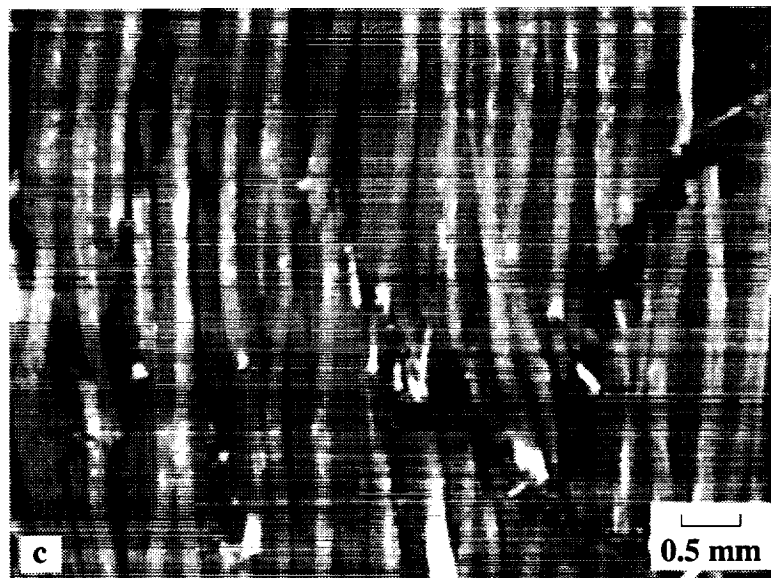
Figure 3.31 Continued.

Load direction
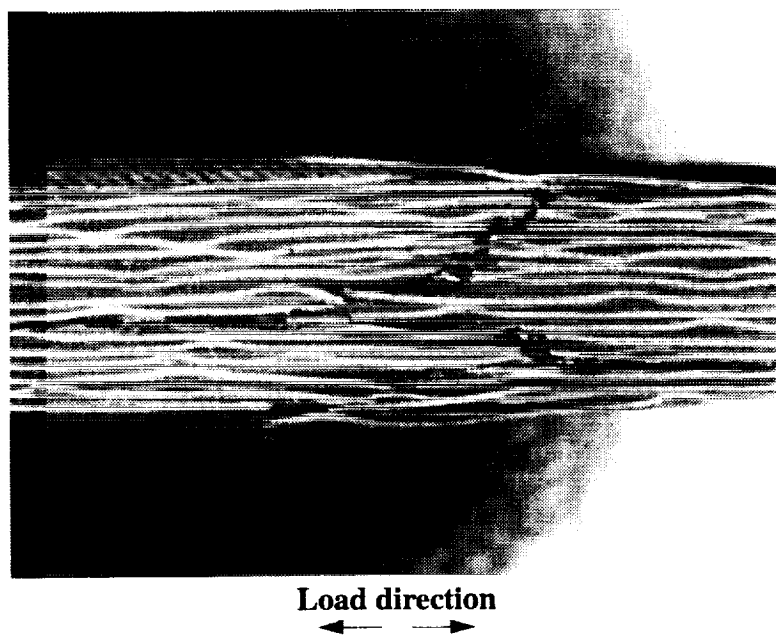
Figure 3.32 Post failure view of 316 °C (600 °F) specimen
at 7.5x magnification: Specimen PC3_20.

stresses, τ_{xz}, which can be relatively large (refer to Figure 1.2 for explanation of coordinate system).

The second mechanism which induces complex stresses at free edges is due to the mismatch in the Poisson's ratios as in the case of the 0° and 90° layers in cross-ply tape laminates. This mismatch in Poisson's ratios leads to equal but opposite signs for the transverse stresses. As is the case for the shear stress in the angle-ply laminates, these transverse stresses cannot exist at free edges of the 0/90 bi-directional tape laminate. As a free edge is approached, these stresses are compensated for by interlaminar shear stresses, τ_{yz}, and interlaminar normal stresses, σ_z, at the interface between the 0° and 90° layers. In addition, Rybicki (1971) showed the interlaminar normal stress, σ_z, is singular at the edge. Therefore, the interlaminar normal stress can produce delamination along the 0/90 interface. Finally, the width of the edge effect boundary layer in tape laminates is a function of the elastic properties of the laminae, the laminae fiber orientation, and laminate geometry. Pipes and Pagano (1970) proposed a simple rule of thumb stating that the boundary layer is equal to the laminate thickness.

For a balanced (0/90) weave, the material properties are equivalent in the longitudinal and transverse directions in each individual ply. As is the case for unidirectional tapes, the interlaminar edge effects are minimized in (0/90) weaves because of the equivalence in the shear coupling terms and the equivalent Poisson's ratios of each individual ply. While edge effects as discussed above are not an issue in (0/90) weaves, the material could experience interlaminar stresses as a result of the weave pattern of the single laminae. For satin weaves, each individual laminae is antisymmetric about the mid-plane. This is due to the fact that the majority of fibers on one side are composed of warp fibers while on the other side the majority of fibers are weft fibers. This asymmetry can cause warping and interlaminar stresses if the plies are fabricated using relatively low stiffness fibers (e.g., glass or aramid). Naik et al. (1991) attributed delaminations in (0/90) weaves to the interlaminar stresses resulting from this asymmetry. However, Bishop (1989) as well as Mitrovic and Carman (1996) stated

that in laminates fabricated with stiff carbon fibers, warping due to unbalanced laminae is hardly detectable because the fibers are so much stiffer than the resin. In this case, it is doubtful that warping contributes to interlaminar stresses and delaminations.

The woven laminates utilized in this effort were fabricated in an anti-symmetric fashion about the laminate midplane. This entailed having 8-plies of warp direction on one side of the midplane, and 8-plies of weft direction on the other. If delaminations were to occur as a result of warping induced interlaminar stresses, it would occur at the midplane. Experimental observations indicated that interlaminar delaminations initiated in the outside plies first. These events were assumed to be the result of crack branching initiating from debonded bundles, and not caused by warp induced interlaminar stresses.

3.10 Residual Compressive Strength

The dependence of strength on damage was studied by interrupting fatigue tests at various stages of degradation and conducting residual compressive strength tests at the corresponding temperature. As was discussed in Chapter I, the elastic modulus can be employed as a quantitative measure of damage. Here, the cyclic tests were stopped when a predefined level of stiffness reduction was achieved. For coupons tested at 22 °C (72 °F) damage was induced by cycling at the maximum stress of 310 MPa (45 ksi). To induce damage at 316 °C (600 °F) the coupons were cycled at a maximum stress of 276 MPa (40 ksi). The interruptions were at approximately the same points of damage as the sectioned coupons discussed earlier in this chapter (i.e., approximately 1, 5, and 10 percent stiffness reduction). Table XII summarizes the results for the residual compressive tests, while Figures 3.33 and 3.34 display the monotonic compressive deformation behavior. Room temperature specimens appeared to be more tolerant of damage quantified by stiffness degradation. Figure 3.35 shows the normalized residual compressive strength as a function of the normalized compressive modulus. Indicated in the figure is the fact that even a small amount of damage caused a significant reduction in strength at elevated temperature. For example, the damage

TABLE XII. RESIDUAL COMPRESSIVE STRENGTH
RESULTS FOR T650-35/PMR15 (0/90) WEAVE
AT 22°C (72°F) AND 316°C (600°F)

Specimen ID	Temperature °C (°F)	*$E_{comp. init,}$ GPa (Msi)	Damage E/E_o	$\sigma_{comp. ult,}$ MPa (ksi)	**$\sigma_{res}/\sigma_{init}$	$\varepsilon_{comp. ult,}$ %
PC2_20	22°C (72°F)	66.3 (9.6)	0.98	-648 (-94)	0.95	1.14
PC3_1	22°C (72°F)	70.5 (10.2)	0.95	-627 (-91)	0.93	1.04
PC3_16	22°C (72°F)	70.0 (10.2)	0.89	-476 (-69)	0.72	0.86
PC3_12	316°C (600°F)	66.4 (9.6)	0.98	-462 (-67)	0.74	0.75
PC2_3	316°C (600°F)	65.6 (9.5)	0.95	-441 (-64)	0.71	0.80
PC2_27	316°C (600°F)	67.2 (9.7)	0.89	-365 (-53)	0.59	0.75

*Initial compressive modulus obtained at test temperature.
**Initial and residual strengths were obtained at corresponding fatigue temperature.
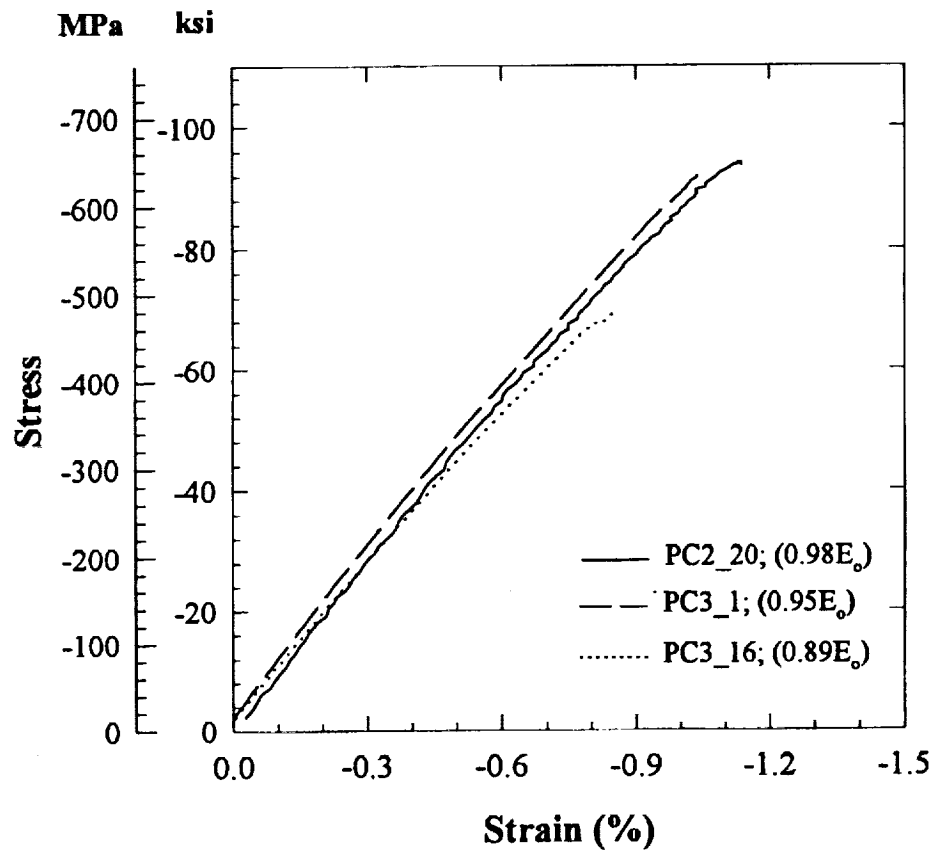
Figure 3.33 Residual compressive strength behavior for three damage levels. Fatigue and residual strength tests conducted at 22°C (72°F): Fatigued at σ_{max} = 310 MPa (45 ksi).
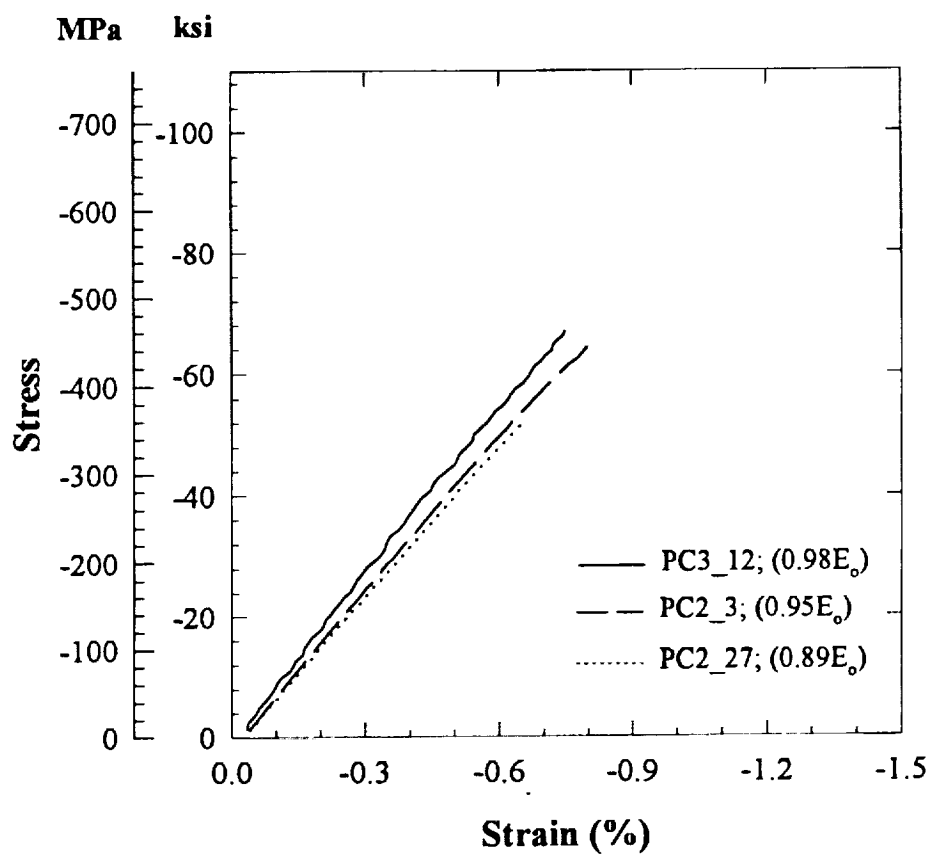
Figure 3.34 Residual compressive strength behavior for three damage levels. Fatigue and residual strength tests conducted at 316°C (600°F): Fatigued at σ_{max} = 276 MPa (40 ksi).
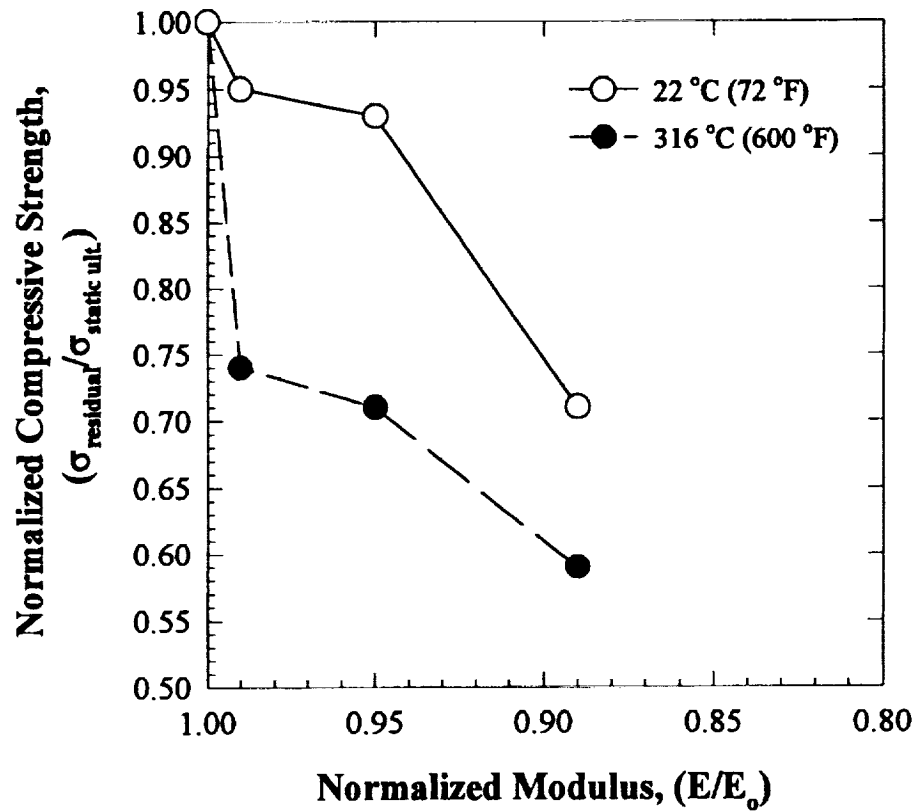
Figure 3.35 Residual compressive strength behavior as a function of damage (i.e., modulus degradation).

which induced a 1 percent loss in stiffness caused a 25 percent reduction in residual compressive strength. For the room temperature case, a relatively large amount of damage, on the order of a 10 percent stiffness degradation, was required to reduce the residual strength by 25 percent. As a final note, the residual strength curve of Figure 3.35 suggests a three stage pattern similar to that of the modulus degradation curves. However, there is insufficient data to make a conclusive statement. Future work that includes more residual compressive strenght data is indicated.

3.11 Microstructural Damage During Residual Compressive Strength Tests

The last topic to be discussed are the microscopic damage mechanisms observed during the residual compressive strength tests. As was the case for the undamaged specimens used in the monotonic compression tests reported on in Section 3.5, failure was instantaneous at both test temperatures. No growth of the initial microstructural damage state was observed prior to failure. Therefore, the edge views were similar to the undamaged specimens described in Section 3.5. Again, monotonic compressive failure at both temperatures appeared to be caused by massive bundle debonds and bundle buckling due to out of plane strains. Figure 3.36 depicts the failure sequence of a residual compressive strength specimen with an initial damage state represented by an 11 percent stiffness reduction induced by the fatigue cycling. The 22 °C (72 °F) specimen contained an interlaminar delamination prior to the monotonic compressive test as a result of the cyclic fatigue. The post failure edge views were identical to the figures of Section 3.5.
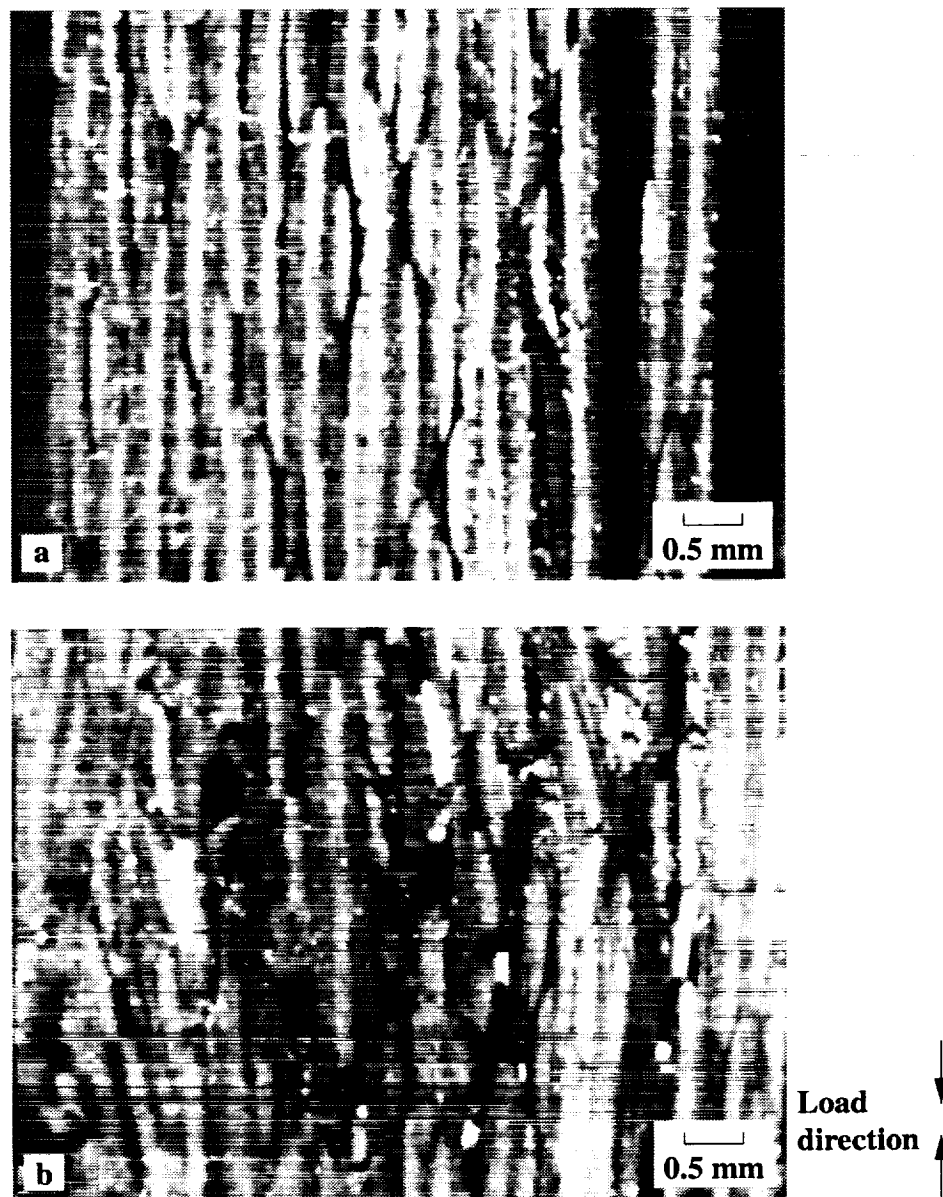
Figure 3.36 Residual compression strength coupon at 22 °C (72 °F) as observed using video images of monitored edge view with 15x magnification. Initial damage state included a delamination induced by the fatigue test. (a) Image taken at –462 MPa (–67 ksi) right before failure. (b) Failure at –483 MPa (–70 ksi): Damage = $0.89E_o$; Specimen PC3_16c.

CHAPTER IV

DAMAGE MODEL AND LIFE PREDICTION

4.1 Introduction

As discussed in the Chapter III, the basic damage mechanisms which occurred in the two dimensional woven PMC studied here are transverse cracks, bundle debonds, interlaminar delamination, buckling of the fiber bundles and fiber bundle breaks. Each mode of damage tended to spread until the material was saturated with damage, thus reaching the fatigue limit for the specimen. To assess the fatigue life of a component the design engineer must have a means to comprehensively predict the evolution of the aforementioned damage mechanisms as a result of cyclic loads. Ye (1989) stated that the ultimate accuracy and success of modeling damage accumulation in a composite material depends greatly on understanding the microscopic mechanisms that produce damage and affect the strength and life of the material. However, constructing life prediction models that account for every microstructural mechanism has not been a successful endeavor for researchers in the past. Even for simple geometries (e.g., unidirectional tapes) subjected to uniaxial loading the evolution of microscopic damage is complex and this leads to computationally intensive models. Models that account for microscopic damage must also account for the microstructure of a composite. Characterizing the properties of the individual constituents of a composite is not trivial. Interface properties are especially difficult to quantify. The majority of

microstructural models at this point in time ignore the contribution of the interface between the fiber and the resin, even though it is understood that the interface is an initiation point for many types of damage. Add to this the complexities associated with woven architectures and alternative approaches to modeling at the microstructural level become very appealing.

Historically phenomenological characterization of damage evolution has been successful because these models focus attention on design features important to the engineer. In effect, the microstructure is homogenized and accounted for macroscopically by tracking specific engineering properties. These models tend to be embodied in design codes and standards well ahead of microstructural models. In the absence of a general theory to describe the complex evolution of the microstructural fatigue damage in composites, a phenomenological approach to modeling was adopted here. This phenomenological model quantitatively measures the degree of damage by establishing a functional relationship between physical properties of the composite and the damage state of the laminate.

The two macroscopic properties most often utilized as a measure of damage for PMCs are residual strength and residual modulus. A detailed discussion of both was presented in Section 1.4. The primary advantage of residual modulus over residual strength is the ability to readily follow modulus degradation via interrupted fatigue tests. For obvious reasons the residual strength can only be measured once during the fatigue life of a specimen. In contrast, the various components of stiffness can be monitored continuously throughout a fatigue test. Moreover, residual strength degradation is not always uniquely related to the state of physical damage. Chou and Croman (1979) showed this to be the case for the sudden death syndrome where physical damage (transverse cracks, delaminations, etc.) occurs continuously but the residual strength of the material is constant until very near failure when the rate of strength degradation accelerates. Careful scrutiny of the residual strength data collected here points to the fact that this may not be as problematic for this material system when subjected to tension-compression cycling. However, due to cyclic data reported elsewhere for other PMC systems subjected to various R-ratios, the design engineer

is cautioned regarding the use of residual strength to predict the fatigue behavior of an individual component in service.

Wang and Chim (1983), Poursartip et al. (1982), Liu (1992), Ye (1989) as well as Lemaitre and Chaboche (1990) have focused on elastic moduli as a pertinent measure of the damage state. Poursartip et al. (1982) pointed out that elastic moduli are particularly attractive because as a fourth order tensor, elastic moduli offer the possibility of distinguishing and monitoring different components of damage. Yet, representing damage with a fourth order tensor has its drawbacks, which is pointed out in the next section. Because of these limitations, the fatigue damage accumulation law proposed here incorporates a scalar representation for damage, but admits an anisotropic evolutionary law. The model predicts the current damage state (as quantified by residual stiffness) and remnant life of a composite that has undergone a known cyclic load at temperature. The damage/life model is dependent on the applied multiaxial stress state. The model is also a function of the applied maximum fatigue stresses, the applied mean stresses, and temperature. The model is characterized using the uniaxial life data and stiffness degradation data of the woven PMC employed in this study.

The following section discusses the damage mechanics formulation concerning stiffness degradation as a damage variable. Afterwards, a section describing the damage evolutionary law is presented. In the subsequent section, characterization is accomplished by utilizing the fatigue data of the previous chapter. Finally, the last section compares predicted results with experimental data.

4.2 Stiffness as a Measure of Damage

It goes without question that the evolution of the microdefects represents an irreversible thermodynamic process. The modeling approach presented here does not allow for flaw healing mechanisms that can take place in certain materials (e.g., ceramics and glasses) at elevated temperatures. At the continuum level, this irreversible process requires the introduction of an internal state variable that serves as a measure of accumulated damage. Here

the development by Duffy and Gyekenyesi (1995) is utilized to present fundamental concepts associated with continuum damage mechanics. Note that in what follows, a physical argument will be made for a specific form of the damage parameter. This parameter will then be related to the elastic moduli of the material.

Consider a uniaxial test specimen depicted in Figure 4.1 and let A_o represent the cross-sectional area in an undamaged state. Denote A as the current cross-sectional area in a damaged state where material defects exist in the cross section. The macroscopic damage associated with this specimen is represented by the scalar

$$D = \frac{(A_o - A)}{A_o} \tag{4.1}$$

or alternatively by $\eta = (1 - D)$. The variable η represents the fraction of cross-sectional area not occupied by voids. Note that a material is undamaged when $D = 0$ or $\eta = 1$. It is somewhat natural to associate the thermodynamic state variable representing damage with a decrease in material integrity.

As it appears above, D is a scalar quantity (i.e., a zero order tensor). With a scalar representation damage must be considered isotropic. This implies that the microstructure with microdefects are randomly oriented and randomly distributed. A number of authors have alternatively treated the damage state variable as a vector (first order tensor), a second order tensor, a fourth order tensor, or an eighth order tensor. Representing the damage state variable as a vector admits information relative to microcrack area and orientation, but anomalies arise in transforming this first order tensor relative to a general multiaxial state of stress. Other authors have proposed using second-order tensors to model damage, but problems occur in representing anisotropic damage in general. Using fourth order tensors is appealing since an analogy can be made to the reduction (evolution) in stiffness properties that occurs in a damaged material.
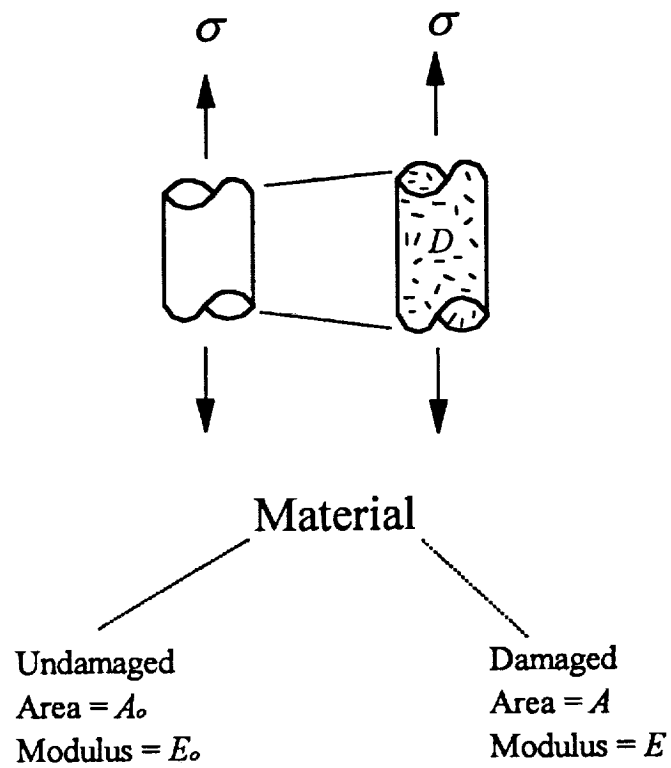
Figure 4.1 Schematic of specimen with reduced stiffness as a result of damage.

The association of the damage parameter defined above with elastic moduli is based, in part, on the assumed existence of an elastic potential energy function that admits damage state variables. As Duffy and Gyekenyesi (1995) showed, this function is a scalar valued function and is defined by the expression

$$\Omega^e = \left(\frac{1}{2}\right)\eta\varepsilon_{ij}C^o_{ijkl}\varepsilon_{kl} \tag{4.2}$$

where C^o_{ijkl} is the undamaged (or reference) fourth order elastic stiffness tensor, ε_{ij} is the second order elastic strain tensor, and η is initially taken as a scalar quantity. The deficiency associated with the scalar representations will be illustrated momentarily. Based on the assumed existence of Ω^e, and the Clausius Duhem inequality, a homogenized stress tensor can be derived such that

$$\sigma_{ij} = \eta C^o_{ijkl}\varepsilon_{kl} \tag{4.3}$$

or

$$\sigma_{ij} = C^d_{ijkl}\varepsilon_{kl} \tag{4.4}$$

where

$$C^d_{ijkl} = \eta C^o_{ijkl} \tag{4.5}$$

Thus C^d_{ijkl} is a damaged stiffness tensor. The result of a scalar damage assumption is that the elements of the damaged stiffness tensor are equal to the elements of the reference stiffness tensor reduced by a common factor η. Note that these stiffness properties are macrovariables, and no assumption was imposed at this point regarding the original material symmetry. Thus, the undamaged material can be elastically isotropic or elastically aniso-

tropic. The method admits either. Also, keep in mind that materials that are originally iso-tropic can damage in an anisotropic fashion. The result is an anisotropic material.

There are deficiencies in associating a scalar damage variable with a three dimensional stress state. Krajcinovic (1989) stated that a damage field is seldom isotropic due to the nature of typical microstructural damage events. Also, Ju (1991) has pointed out that a scalar damage variable will reduce the bulk and the shear moduli by an equal amount, that is

$$G^d = \eta G^o \qquad (4.6)$$

and

$$K^d = \eta K^o \qquad (4.7)$$

where G^d and K^d are damaged shear and bulk moduli, respectively. This leads to

$$\frac{G^d}{K^d} = \frac{G^o}{K^o} \qquad (4.8)$$

which implies that Poisson's ratio does not evolve (i.e., $v^d = v^o$). Talreja (1987) points out that this is a rather strong restriction which has limited experimental support.

Although a scalar damage variable may not agree with physical observations concerning the Poisson's ratio, it does admit certain mathematical restrictions imposed on the elastic moduli concerning basic physical principles. As an example of a physical principle, a tensile force should produce an extension in the direction of the force. In addition, a hydrostatic pressure should not cause an expansion of the material. These physical principles require that for a composite material E_L, E_T, $G_{LT} > 0$, where the constants represent the normal and shear moduli in respect to the longitudinal and transverse directions. If the initial elastic constants of a material system satisfy these restrictions, then the damaged constants will also satisfy the restrictions since $0 \leq \eta \leq 1$. The complete list of restrictions imposed on elastic constants for an orthotropic material was presented by Agarwal and

Broutman (1990) and will not be repeated here. It is sufficient to note that these restrictions on the elastic moduli will not be violated using a scalar representation of damage.

In order to circumvent the difficulties associated with a scalar representation of damage, one might consider higher order tensors. It was mentioned earlier that difficulties also arise when representing damage with first and second rank tensors. However, a fourth order tensor can be used to circumvent these difficulties. To illustrate the use of a fourth order damage tensor, once again assume the existence of an elastic potential energy function that admits a damage state variable. This function can be expressed as

$$\Omega^e = \left(\frac{1}{2}\right)\varepsilon_{ij}\eta_{ijkl}\left(D_{mnop}\right)C^o_{klrs}\varepsilon_{rs} \tag{4.9}$$

where η_{ijkl} is a fourth order tensor valued function that is dependent on a fourth order damage state variable D_{mnop}. Note that the term $\eta_{ijrs}(D_{mnop})$ should be interpreted as "η is a function of D." This term should not be interpreted as a tensor operation between η and D. Now, the Cauchy stress is given by the expression

$$\sigma_{ij} = \eta_{ijkl}\left(D_{mnop}\right)C^o_{klrs}\varepsilon_{rs} \tag{4.10}$$

The simplest form of this transformation tensor is

$$\eta_{ijrs} = I_{ijrs} - D_{ijrs} \tag{4.11}$$

where I_{ijrs} is the fourth order identity tensor. This is analogous to the scalar relationship $\eta = (1 - D)$. Other expressions could be considered, but at this point in time the lack of experimental data discourages this endeavor.

Even though many authors have advocated the use of fourth order representation for damage, most of these same authors have recognized the complexity in tracking all the

necessary components in order to characterize damage with this approach. The testing would involve multiaxial load application while concurrently monitoring all the elastic constants. The experimental program necessary to accomplish multiaxial load application is difficult and expensive. Thus, the data base of degraded moduli for materials subjected to multiaxial load conditions is non-existent. For these reasons the focus of the discussion returns to the utilization of a scalar damage variable.

4.3 Scalar Damage Variable

Because of the complexities involved with a higher order representations of damage, the current study focused on defining the damage variable as a scalar (i.e., a zero order tensor). Krajcinovic (1987) stated that even though few would steadfastly deny the directional nature of damage resulting from flat crack-like defects such as transverse cracks and delaminations, the undeniable simplicity of the scalar representation has a certain level of merit deserving the appropriate attention. Furthermore, the majority of current experimental programs monitor properties related to the uniaxial application of load, thereby limiting the ability to characterize higher order representations of damage. Similar reasoning was utilized by Arnold and Kruch (1991) concerning the use of a scalar damage variable for modeling damage evolution in a unidirectional metal matrix composites (MMC's). Although the damage measure is a scalar, damage evolution is anisotropic. This anisotropic facet of the proposed model is presented in the next section.

The measurement of damage is not directly accessible. Its quantitative evaluation, as with many properties, is linked to the definition of the variable chosen to represent the phenomenon. The inferred relationship is based on a link between deformation and damage, i.e., to the modification of the mechanical properties characterized. The following uniaxial stress strain relationships

$$\sigma = E\varepsilon \tag{4.12}$$

and

$$\sigma = \eta E_o \varepsilon \qquad (4.13)$$

are adopted from the previous discussion. Here E_o is the initial longitudinal stiffness and E is the current longitudinal stiffness. Alternatively,

$$\sigma = (1 - D)E_o \varepsilon \qquad (4.14)$$

can be used. Thus, a relationship between the damage variable and stiffness can be expressed as

$$(1 - D)E_o = E \qquad (4.15)$$

Rearranging the terms of Equation (4.15), damage is defined as

$$D = 1 - \frac{E}{E_o} \qquad (4.16)$$

Thus, if the initial Young's modulus E_o is known, any measurement of the residual elastic stiffness can be used to determine the damage. Note that because of the scalar representation of damage, any of the elastic moduli can be implemented in Equation (4.16). However, in the testing program presented here, data relative to Young's modulus in the longitudinal fiber direction, i.e., E_L, was obtained. Now that the scalar damage parameter D has been associated with an engineering property that was readily measured, the next task involves describing how this parameter evolves under cyclic load.

4.4 Damage Evolutionary Law

To describe the evolution of damage, a power law relationship is employed in a fashion similar to work by Wang and Chim (1983), Hwang and Han (1989) as well as Ye (1989).

The evolutionary laws in those studies were developed for the case of uniaxially applied stresses with fixed R-ratios. Here, the general form of the evolutionary law is expressed as a power function in terms of Φ which is a function that accounts for multiaxial cyclic stress states. The evolutionary law is also a function of the current state of damage. The function Φ is dependent on the maximum cyclic stress and the cyclic mean stress. The damage rate is expressed as

$$\frac{dD}{dN} = A \frac{\Phi^C}{B(D + D_o)^{B-1}} \qquad (4.17)$$

where D_o is the initial damage state and A, B, and C are material constants. The functional dependence of Φ is stipulated as the difference between a function F (defined momentarily) evaluated at two different stress states, i.e.,

$$\Phi = \left[F\left(S^*_{max}, \sigma^*_U\right) - F\left(S^*_{mean}, \sigma^*_U\right) \right]^{\frac{1}{2}} \qquad (4.18)$$

where S^*_{max} and S^*_{mean} are vectors with stress components defined as

$$S^*_{max} = \left\{ \begin{array}{c} \sigma_{Lmax} \\ \sigma_{Tmax} \\ \tau_{LTmax} \end{array} \right\} \qquad (4.19)$$

and

$$S^*_{mean} = \left\{ \begin{array}{c} \sigma_{Lmean} \\ \sigma_{Tmean} \\ \tau_{LTmean} \end{array} \right\} \qquad (4.20)$$

Thus, S^*_{max} and S^*_{mean} are vectors with components dependent on the maximum cyclic stresses (σ_{Lmax}, σ_{Tmax}, and τ_{LTmax}) and cyclic mean stresses (σ_{Lmean}, σ_{Tmean}, and τ_{LTmean}), respectively. Therefore, a functional dependence upon the R-ratio is introduced through the use of S^*_{max} and S^*_{mean}. Note that the components are referenced to the local L-T axis (i.e., longitudinal and transverse axis of the material). The vector σ^*_U is composed of ultimate strengths, i.e.,

$$\sigma^*_U = \begin{Bmatrix} \sigma_{LU} \\ \sigma_{TU} \\ \tau_{LTU} \\ \sigma_{ZU} \end{Bmatrix} \qquad (4.21)$$

The values σ_{LU}, σ_{TU}, σ_{ZU} and τ_{LTU} are the ultimate monotonic failure loads in the longitudinal and transverse fiber directions as well as the normal strength in the out of plane direction, respectively.

The function Φ is a measure of the intensity of the applied multiaxial stress state with respect to the ultimate failure envelope of the anisotropic composite. The ultimate strength values are defined by monotonic tests. The function F in Equation (4.18) defines the monotonic failure surface for a two dimensional laminae. Although there are many monotonic failure functions, this study employs a derivative of the Hill failure theory for anisotropic materials due to its acceptance and wide use. The Hill failure surface, assuming plane stress conditions, is expressed as

$$\left(\frac{\sigma_L}{\sigma_{LU}}\right)^2 + \left(\frac{\sigma_T}{\sigma_{TU}}\right)^2 - \left(\frac{1}{\sigma^2_{LU}} + \frac{1}{\sigma^2_{TU}} - \frac{1}{\sigma^2_{ZU}}\right)\sigma_L\sigma_T + \left(\frac{\tau_{LT}}{\tau_{LTU}}\right)^2 = 1 \qquad (4.22)$$

Making use of this definition for multiaxial failure, the function F is defined as

$$F = \left(\frac{\sigma_L}{\sigma_{LU}}\right)^2 + \left(\frac{\sigma_T}{\sigma_{TU}}\right)^2 - \left(\frac{1}{\sigma_{LU}^2} + \frac{1}{\sigma_{TU}^2} - \frac{1}{\sigma_{ZU}^2}\right)\sigma_L\sigma_T + \left(\frac{\tau_{LT}}{\tau_{LTU}}\right)^2 \qquad (4.23)$$

The Hill theory stipulates that for a plane stress environment the monotonic failure initiates when the equality of Equation (4.22) is met. Note that when the applied normal stresses are compressive, ultimate compressive strengths are used Equations (4.22) and (4.23).

Alternatively, the Tsai-Hill failure criterion can be used. The Tsai-Hill criteria is a simplification of the Hill theory based on the assumption that $\sigma_{TU} = \sigma_{ZU}$. This assumption is relevant for transversely isotropic unidirectional tape laminae. However, the woven composite studied here is an orthotropic material where strengths in the longitudinal and transverse direction are equal. Therefore, the Hill criterion can be modified for this material system by stipulating

$$\sigma_{LU} = \sigma_{TU} \qquad (4.24)$$

Thus, the form of F used here is obtained by substituting Equation (4.24) into Equation (4.23). Therefore

$$F = \left(\frac{\sigma_L}{\sigma_{LU}}\right)^2 + \left(\frac{\sigma_T}{\sigma_{LU}}\right)^2 - \left(\frac{2}{\sigma_{LU}^2} - \frac{1}{\sigma_{ZU}^2}\right)\sigma_L\sigma_T + \left(\frac{\tau_{LT}}{\tau_{LTU}}\right)^2 \qquad (4.25)$$

The value of σ_{ZU} presents a difficulty since no out of plane data was gathered in this effort. An estimation of the out of plane strength, $\bar{\sigma}_{ZU}$, can be obtained by the use of monotonic strength data of a unidirectional tape in the transverse direction (i.e., perpendicular to the fiber direction). This is a valid comparison since both the transverse strength of a unidirectional tape and the out of plane strength of a 2-D weave are obtained in a direction perpendicular to the fibers. As it turns out, this study did not require the evaluation of multiaxial data, so this strength parameter was not required.

Damage evolution can be achieved by integrating Equation (4.17) and by assuming that $D = D_o$ when $N = 0$. Therefore, damage as a function of fatigue cycles is

$$D = \left[A\Phi^C N + \left(2D_o\right)^B \right]^{\frac{1}{B}} - D_o \tag{4.26}$$

Modeling of property degradation is achieved by combining Equations (4.16) and (4.26). Here, the residual modulus as a function of accumulated cycles is expressed as

$$E = E_o \left\{ 1 - \left[A\Phi^C N + \left(2D_o\right)^B \right]^{\frac{1}{B}} + D_o \right\} \tag{4.27}$$

where E_o is the initial modulus value corresponding to $D = 0$. To underscore the point that E_o corresponds to $D = 0$, and not to $D = D_o$, assume the case of $B = 1$ and $N = 0$. As a result of this assumption, the residual modulus at the beginning of a test (i.e., $N = 0$) is expressed as

$$E = \left(1 - D_o\right)E_o \tag{4.28}$$

Note that the residual modulus, E, is less than E_o since the material is assumed to have some initial damage prior to testing (e.g., as a result of processing). Thus, E_o is a modulus value corresponding to a specimen with no damage, i.e., $D = 0$.

At the end of the fatigue life of a specimen, where $N = N_f$, the damage parameter reaches a critical value defined as

$$D = D_o + D_{critical} \tag{4.29}$$

Combining equations (4.29) and (4.26) and solving for the number of cycles (N_f) associated with $D_{critical}$, the life model is expressed as follows

$$N_f = \frac{\left(D_{critical} + 2D_o\right)^B - \left(2D_o\right)^B}{A\Phi^C} \tag{4.30}$$

In the next section the cyclic fatigue data presented in Chapter III will be used to characterize the constants A, B, and C.

4.5 Characterizing the Damage Evolution Law

In this section the model is characterized utilizing the uniaxial, fully-reversed (zero mean stress), cyclic fatigue data of the previous chapter at the temperatures of 22 °C (72 °F) and 316 °C (600 °F). The initial step in defining the constants required studying the compressive modulus degradation curves as a function of accumulated cycles at various maximum cyclic stresses. Although the results presented in Chapter III indicated equivalent degradation rates for both tensile and compressive moduli (see Figures 3.17 and 3.18), the compressive modulus was chosen to characterize the model due to the fact that under fully reversed conditions failure of the tested coupons occurred in the compressive regime.

The stiffness degradation curves presented in the previous chapter (see Figures 3.16 to 3.19) indicate that the damage accumulation as a function maximum cyclic stress involved three stages. The stages consisted of an initial stage where a high degradation rate dominates (Stage I - which accounted for 1 percent of the life); a linear regime (Stage II - composing the majority of life); and an increased rate of degradation as the fatigue life of the specimen was approached (Stage III - occurring in the last few cycles before failure). As was explained in Chapter III, Stage II involved a stable accumulation in crack density. Since the linear portion of the damage accumulation curves accounted for the majority of fatigue life for this PMC, it was reasonable to model damage for this stage. A similar approach of modeling only certain portions of the degradation curve was taken by Ye (1989).

The following observations obtained from the fatigue data were used to simplify the

characterization process. First, since the degradations were linear (i.e., constant rates regardless of the current level of damage), Equation (4.17) was assumed to be dependent only on the cyclic stress state, Φ. Thus, the current level of damage was not altering the rate of damage accumulation. To eliminate the dependence on the current level of damage, the constant B was taken equal to 1 in Equations (4.17), (4.26), (4.27) and (4.30). Second, Figure 3.16 indicates that the modulus degradation rates were independent of temperature. Therefore, the room temperature and elevated temperature results were pooled for the characterization of the damage rate constants A, B, and C in Equation (4.17).

The damage rate for an individual specimen was calculated by fitting a linear regression curve to the Stage II segment of the compressive modulus degradation curve as depicted in Figure 4.2. The modulus degradation rate was obtained from the regression line. Next, the modulus degradation rate was transformed to a damage rate by employing the derivative of Equation (4.16) with respect to N, i.e.,

$$\frac{dD}{dN} = -\frac{1}{E_o}\left(\frac{dE}{dN}\right) \tag{4.31}$$

A summary of damage rates, dD/dN, for various specimens as a function of Φ and temperature is presented in Table XIII. As a result of the uniaxial stress conditions for the fatigue tests conducted here, the only strength value required to calculate Φ was the longitudinal tensile strength, σ_{LU}. From Chapter III it was shown that $\sigma_{LU} = 855$ MPa (124 ksi).

The log of the damage rates (both room temperature and elevated temperature) were plotted as a function of the log of the multiaxial cyclic stress state Φ as shown in Figure 4.3. Linear regression was used to construct the line depicted in Figure 4.3. The constant A represents the inverse log of the intercept and the constant C represents the slope of the line. From the regression analysis, the model constants for the current material system were

$$A = 0.1257 \tag{4.32}$$
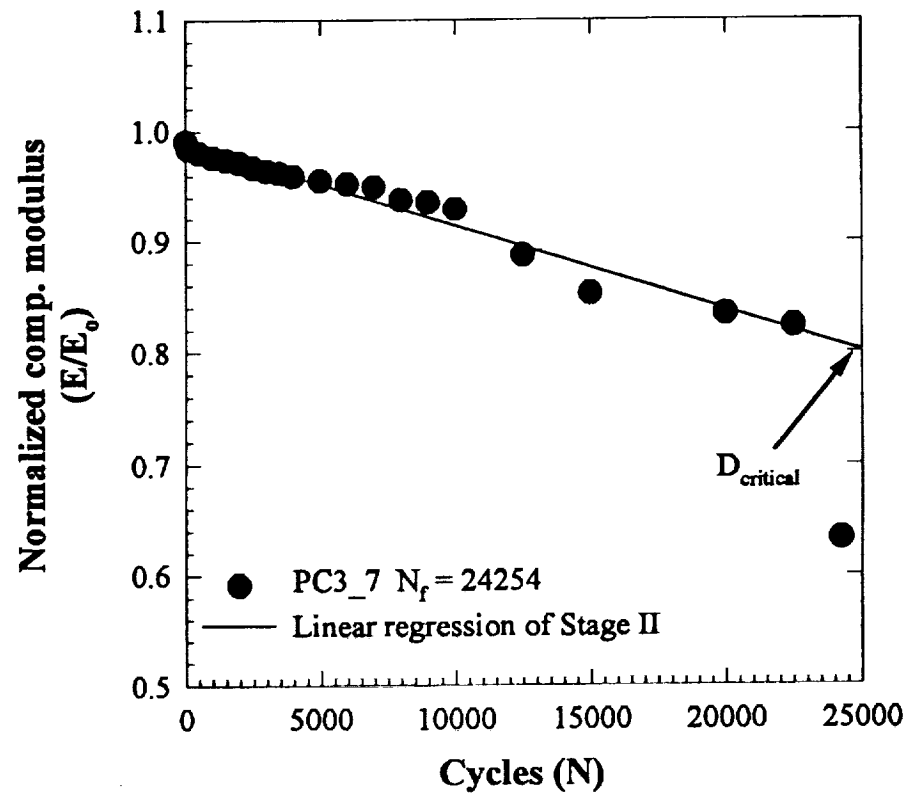
Figure 4.2 Stage II linear regression curve fit for a typical compressive modulus plot at 22°C (72°F): σ_{Lmax} = 345 MPa (50 ksi); Φ = 0.403.

TABLE XIII. FATIGUE DATA FOR CHARACTERIZING MODEL

Specimen ID	Temperature T °C (°F)	Max. stress σ_{Lmax} MPa (ksi)	Stress state Φ	Cycles to failure N_f	Damage rate dD/dN	Critical damage $D_{critical}$
PC3_32	22 (72)	414 (60)	0.484	2426	5.840×10^{-5}	0.142
PC2_30	22 (72)	379 (55)	0.444	3552	4.184×10^{-5}	0.149
PC3_17	22 (72)	379 (55)	0.444	3721	4.792×10^{-5}	0.178
PC2_24	22 (72)	379 (55)	0.444	8429	1.888×10^{-5}	0.159
PC2_6	22 (72)	345 (50)	0.403	21804	8.905×10^{-6}	0.194
PC3_7	22 (72)	345 (50)	0.403	24254	7.650×10^{-6}	0.186
PC3_9	22 (72)	345 (50)	0.403	26884	6.718×10^{-6}	0.181
PC2_13	22 (72)	310 (45)	0.363	160423	1.542×10^{-6}	0.247
PC2_31	22 (72)	310 (45)	0.363	111245	2.232×10^{-6}	0.248
PC2_32	22 (72)	310 (45)	0.363	61231	3.814×10^{-6}	0.234
PC2_12	22 (72)	276 (40)	0.323	1367095	2.012×10^{-7}	0.275
PC2_28	316 (600)	310 (45)	0.363	5678	3.450×10^{-6}	0.0196
PC1_4	316 (600)	310 (45)	0.363	7858	8.672×10^{-6}	0.0685
PC3_8	316 (600)	276 (40)	0.323	38164	3.814×10^{-6}	0.146
PC1_8	316 (600)	276 (40)	0.323	134100	5.842×10^{-7}	0.0783
PC2_16	316 (600)	241 (35)	0.282	432943	2.513×10^{-7}	0.109
PC1_5	316 (600)	241 (35)	0.282	354440	3.490×10^{-7}	0.124
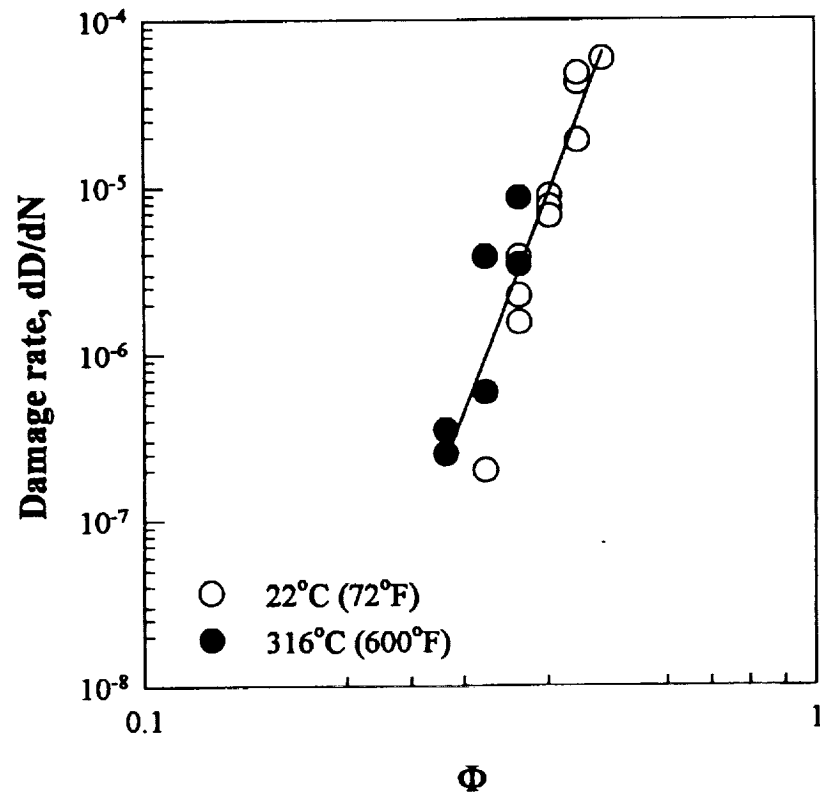
Figure 4.3 Damage rate as a function of stress state, Φ.

$$B = 1.000 \tag{4.33}$$

and

$$C = 10.436 \tag{4.34}$$

4.6 Defining Critical Damage

The fatigue life data (but not the damage rates) presented in Chapter III showed a significant decrease in cycles to failure as a result of the elevated temperature. This temperature dependence was a result of the material's lower tolerance to damage at elevated temperature. Although the specimens damage accumulation rates at a given maximum cyclic stress were approximately the same at either 22 °C (72 °F) or 316 °C (600 °F), the elevated temperature coupons failed at a much lower critical damage state. Thus in order to model the fatigue life of this composite material, a damage rate equation and a critical damage state must be defined. In utilizing continuum damage mechanics failure is typically associated with $D = 1$. This does not work here. Thus in this section a critical damage state is carefully defined such that it is temperature dependent, as well as dependent on the applied stress state.

The critical damage values were defined as the lowest stiffness value on the Stage II portion of the modulus degradation curves. For example, the critical damage state for a specimen at room temperature and a maximum cyclic stress of 345 MPa (50 ksi) is identified in Figure 4.2. A systematic approach for calculating $D_{critical}$ for individual specimens was accomplished by utilizing the linear regression curves fitted to Stage II. The critical residual moduli were obtained from the regression curves by inputting the cycles to failure, N_f of the respective specimen. This value of residual modulus was transformed to $D_{critical}$ utilizing Equation (4.16). The $D_{critical}$ results are presented in Table XIII. The discussions in Sections 3.7 and 3.10 as well as the information presented in Table XIII show that $D_{critical}$ was extremely sensitive to temperature. Based on these observations, the critical damage

variable was formulated as a function of both the applied stress state, Φ, and temperature, T.

A linear relationship was obtained by plotting $D_{critical}$ versus Φ as shown in Figure 4.4. The two lines depicted in the figure were obtained by fitting linear regression curves to the data sets corresponding to room temperature and elevated temperature. One can easily discern that the slopes from both temperature regimes were approximately equal. Only the intercepts along the $D_{critical}$ axis were different. Thus

$$D_{critical} = P(T) + Q \cdot \Phi \qquad (4.35)$$

The constant Q is taken as an average of the slopes of two lines in Figure 4.4. It is assumed that the parameter $P(T)$ is linearly dependent on temperature since only two temperature conditions were used to characterize $D_{critical}$. Based on the data, the constants are calculated as

$$P = \left(-6.510 \times 10^{-4}\right) \cdot T + 0.5776 \qquad (4.36)$$

$$Q = -8.877 \times 10^{-1} \qquad (4.37)$$

for metric units (°C), and

$$P = \left(-3.625 \times 10^{-4}\right) \cdot T + 0.5894 \qquad (4.38)$$

$$Q = -8.877 \times 10^{-1} \qquad (4.39)$$

for English units (°F). The expression for $P(T)$ allows for a family of $D_{critical}$ curves between the two test temperatures. With the damage evolutionary law and $D_{critical}$ defined, the focus is now turned to a comparison with experimental data.
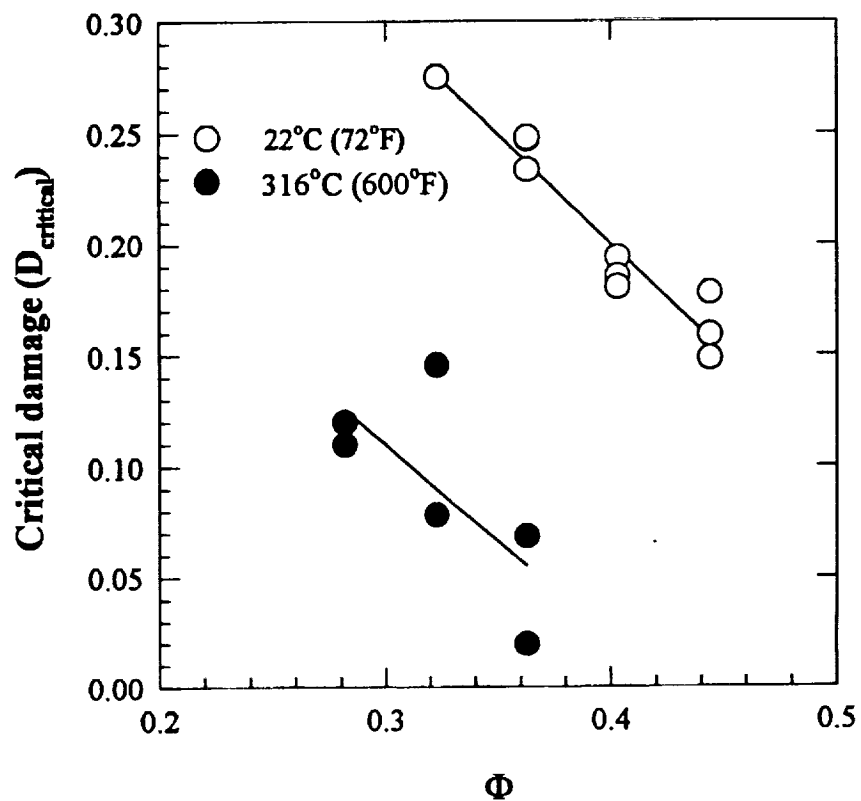
Figure 4.4 Critical damage as a function of stress state, Φ, and temperature, T.

4.7 Comparison of Model with Experimental Data

Substituting Equations (4.32) through (4.35) into (4.30), the fatigue life can be expressed as

$$N_f = \frac{\left[\left(-6.510 \times 10^{-4}\right) \cdot T + 0.5776\right] - 8.877 \times 10^{-1}(\Phi)}{0.1257(\Phi)^{10.436}} \tag{4.40}$$

for metric units (°C), or

$$N_f = \frac{\left[\left(-3.625 \times 10^{-4}\right) \cdot T + 0.5894\right] - 8.877 \times 10^{-1}(\Phi)}{0.1257(\Phi)^{10.436}} \tag{4.41}$$

for English units (°F). The residual modulus as a function of accumulated cycles is as follows:

$$E = E_o\left\{1 - (0.1257)\left[\Phi^{10.436}\right]N - D_o\right\} \tag{4.42}$$

Note that the cycles to failure (N_f) is explicitly temperature dependent. The residual modulus is implicitly temperature dependent since E_o is temperature dependent. It is assumed that the initial damage, D_o, is very small in respect to the damage which is induced during fatigue cycling. Therefore, D_o is equated to 0. As a result (see Equation 4.28), E_o is equal to the initial modulus prior to cyclic fatigue. The residual modulus in a normalized form is expressed as

$$\frac{E}{E_o} = 1 - (0.1257)\left[\Phi^{10.436}\right]N \tag{4.43}$$

In addition to the data at 22 °C (72 °F) and 316 °C (600 °F), three coupons were tested at the intermediate temperature of 204 °C (400 °F) to further substantiate the predictive

capabilities of the model. Tables XIV through XVI as well as Figure 4.5 show the life prediction results in comparison to the experimental data. Recalling that the model characterization was achieved using 22 °C (72 °F) and 316 °C (600 °F) data, the theoretical predictions at those temperatures show good agreement with the data which is expected. The model also shows good agreement with the 204 °C (400 °F) cyclic fatigue data.

Note the plateau behavior in all three curves at the high maximum stress levels. This is indicative of stress levels at which no stiffness loss is apparent prior to failure. Because there is no propagation of measurable damage at maximum cyclic stresses above the plateau, the model cannot be applied at those high stresses. This circumstance is only minimally detrimental since the model allows maximum stresses which produce lives in the 100 cycle range. Usually a design engineer is interested in lives ranging from 10^4 to 10^7 cycles to failure.

The available cyclic fatigue data at the three temperatures appears to support the asymptotic behavior of the model. For the room temperature data, no stiffness degradation was observed at the 483 MPa (70 ksi) maximum cyclic stress. This stress level is located just below 538 MPa (78 ksi) plateau of the model. Thus from the experimental data one would not expect stiffness degradation above the 483 MPa (70 ksi) level. At 316 °C (600 °F) the model's plateau occurs at the maximum cyclic stress of 359 MPa (52 ksi). This also agrees with the available experimental data. For both the 345 MPa (50 ksi) and the 379 MPa (55 ksi) maximum cyclic stress levels at 316 °C (600 °F), no degradation of the moduli were recorded prior to failure. Finally, at 204 °C (400 °F) the model's plateau occurs at a maximum cyclic stress of 428 MPa (62 ksi). The cyclic fatigue data at 448 MPa (65 ksi) maximum cyclic stress revealed no modulus reduction prior to failure, once again showing agreement with the model.

A comparison between the predicted residual compressive stiffness using Equation (4.43) and the experimental data at 204 °C (400 °F) is displayed in Figure 4.6. Equation (4.40) was utilized to define the total number of cycles to failure for the stiffness prediction at the

TABLE XIV. COMPARISON BETWEEN EXPERIMENTAL DATA AND THEORY AT 22°C (72°F)

σ_{Lmax}, MPa (ksi)	Φ	Number of repeats	Average N_{fave}	Stnd Dev of N_f	Model prediction
483 (70)	0.565	1	100	—	194
414 (60)	0.484	1	2426	—	2079
379 (55)	0.444	3	5234	2768	6535
345 (50)	0.403	3	24314	2540	21401
310 (45)	0.363	3	110966	49596	75474
276 (40)	0.323	1	1367095	—	296351

TABLE XV. COMPARISON BETWEEN EXPERIMENTAL DATA AND THEORY AT 316°C (600°F)

σ_{Lmax}, MPa (ksi)	Φ	Number of repeats	Average N_{fave}	Stnd Dev of N_f	Model prediction
379 (55)	0.444	3	158	93	—
345 (50)	0.403	3	353	217	1453
310 (45)	0.363	3	6225	1439	15548
276 (40)	0.323	3	68731	56650	91392
241 (35)	0.282	2	393691	55510	522327

TABLE XVI. COMPARISON BETWEEN EXPERIMENTAL DATA AND THEORY AT 204°C (400°F)

σ_{Lmax}, MPa (ksi)	Φ	Number of repeats	N_{fave}	Model prediction
448 (65)	0.524	1	78	—
379 (55)	0.444	1	952	1950
310 (45)	0.363	1	40740	38204
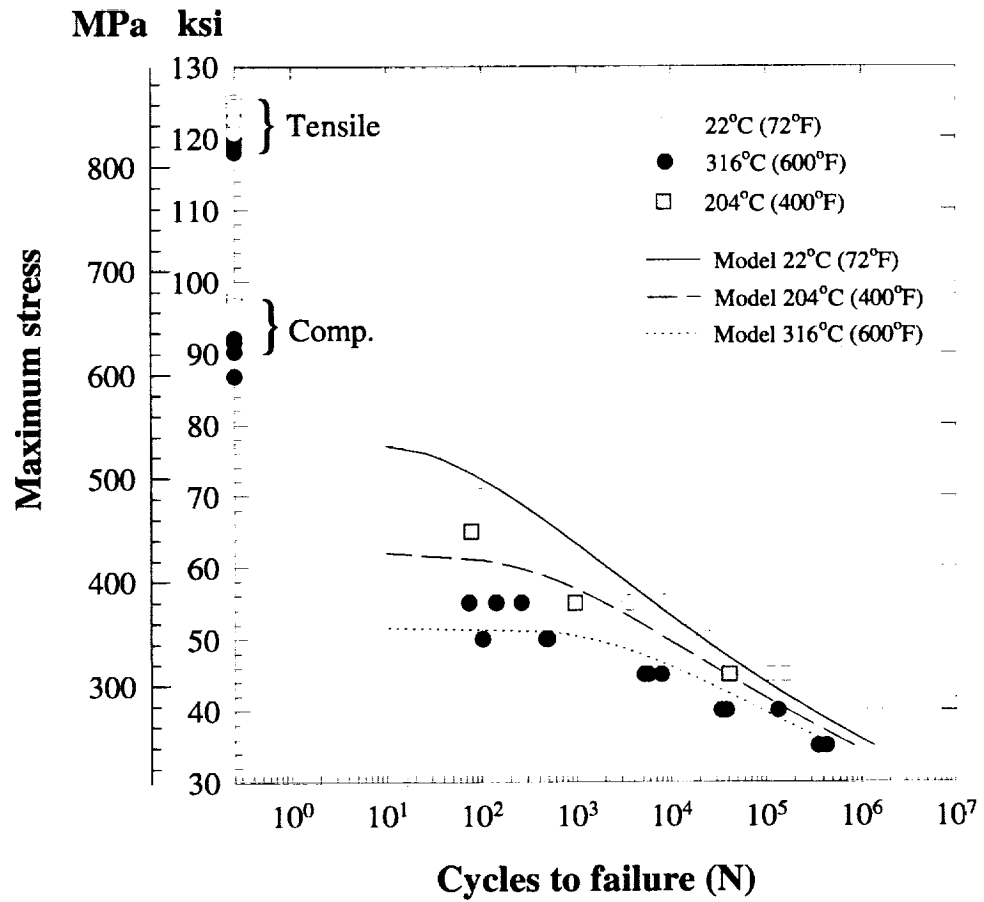
Figure 4.5 Stress based isothermal fatigue life comparison between experimental data and analytical predictions.
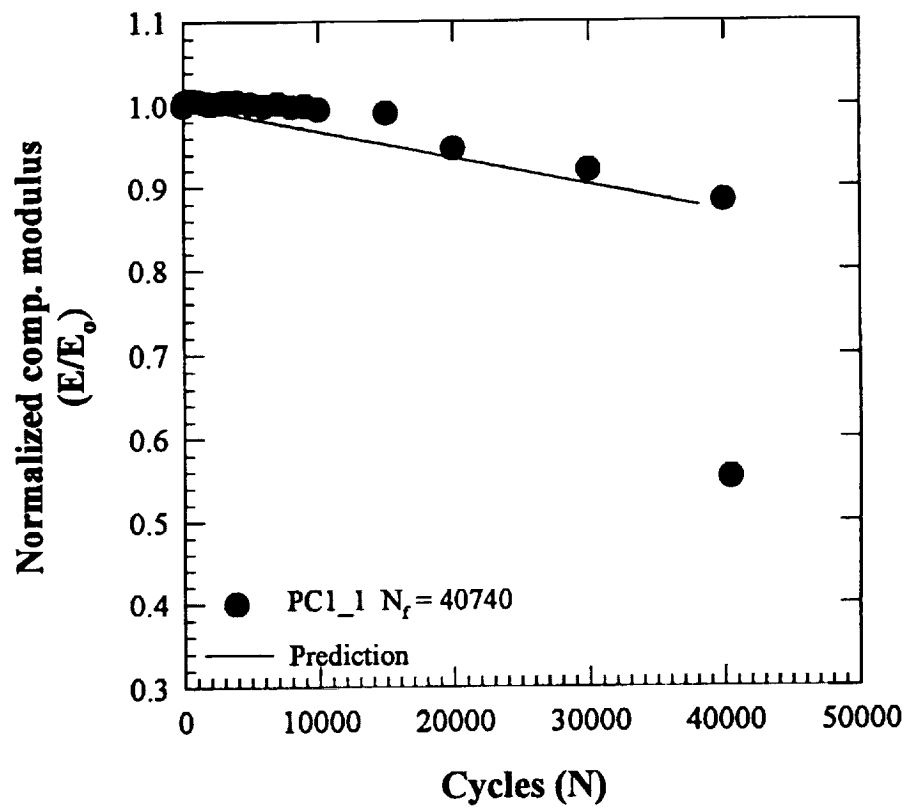
Figure 4.6 Model versus data comparison of normalized compressive modulus as a function of cycles at 204°C (400°F): σ_{Lmax} = 310 MPa (45 ksi); Φ = 0.363.

respective stress and temperature. As Figure 4.6 depicts, the agreement was good concerning both the slope of the line and cycles to $D_{critical}$.

CHAPTER V

SUMMARY, CONCLUSIONS AND FUTURE DIRECTIONS

5.1 Summary

The use of polymer matrix composites (PMCs) has been expanded to load bearing structures exposed to elevated temperatures. As a result, it is essential that quality experimental data be acquired at test conditions approaching the service conditions of the component. Furthermore, a dependable methodology for life prediction needs to be established for the successful and cost effective commercialization of PMCs. To help meet these requirements, it was the intention of this work to investigate the monotonic tensile, monotonic compressive, and fully reversed fatigue behavior exhibited by a carbon fiber/polyimide resin, woven laminate at room (22 °C/72 °F) and elevated (316 °C/600 °F) temperatures. This particular (0/90) weave was designated as T650-35/PMR15. The effects of mechanical cycling and temperature on the macroscopic properties and microscopic damage behavior were studied. The macroscopic properties of interest included the longitudinal stiffness and the residual compressive strength. The accumulation of microscopic damage was studied by destructive sectioning and video monitoring of the coupon edge. In addition, a model based on a measurable damage variable was developed and characterized utilizing the fully reversed fatigue data. The model predicts property degradation and life as a function of multiaxially applied

cyclic stresses and temperature. A scalar representation of damage (i.e., isotropic damage) is employed in the model.

The following sections discuss the accomplishments, results, and conclusions of the experimental and modeling efforts. Presented first is a section focusing on the experimental segment of the research. This is followed by a discussion concerning the analytical model. In the final section, suggestions for future research are presented.

5.2 General Discussion of the Experimentation

To achieve the experimental goals of this study, unique experimental techniques were developed and employed for the isothermal tests. This included designing tensile coupon geometry and unsupported compressive coupon geometry, developing accurate methods of temperature control and measurement for quartz lamp heating, as well as programming advanced software to drive the hydraulic load frame. Experimental testing procedures and techniques were specified that resulted in closely controlled isothermal tests performed in a uniaxial, monotonic and fully reversed fatigue load conditions. Detailed discussions for each of the experimental accomplishments are presented in Chapter II.

Upon completing the monotonic and fatigue tests, the isothermal response was compared and analyzed from both phenomenological and microstructural viewpoints. The conclusions based on the results of Chapter III are as follows:

- Due to the fiber dominated nature of the weave, the monotonic tensile properties were relatively unaffected by temperature. The stiffness, ultimate strength and ultimate strain each showed reductions of less than 3 percent. Concerning microstructural damage, transverse cracks appeared first. They were followed by bundle debonds which in turn propagated into interlaminar delaminations. Coupons failed as a result of isolated debonded warp bundles fracturing.

- Elevated temperature had a more pronounced affect on the monotonic compressive properties of the composite. Although the stiffness of the coupons were relatively

unaffected, the ultimate strength and ultimate strain were reduced by approximately 7 percent. The microstructural observations indicated that there was no observable damage prior to failure at either temperature. For both room temperature and elevated temperature the instantaneous occurrence of massive bundle debonds and bundle buckling caused failure.

- For the fully reversed fatigue results, the elevated temperature data showed a significant reduction in cycles to failure when compared to room temperature data tested at the same maximum stress level. The residual compressive strength (which is heavily dependent on the resin, and therefore also sensitive to temperature) played a significant role in fatigue life for reversed loads. To underscore this issue note that failure always occurred during the compressive portion of the cycle.

- At both room temperature and elevated temperature, the stiffness as a function of accumulated cycles displayed a three stage degradation behavior. The first stage occurred during the initial 1 percent of life. This was followed by a linear second stage (constant degradation rate) which constituted the majority of life. As failure approached, a dramatic increase in the damage rate occurred. Comparisons between room temperature and elevated temperature stiffness behavior for equivalent maximum cyclic stresses showed equivalent degradation rates. Although the degradation rates were equivalent, elevated temperature coupons failed much earlier than the room temperature coupons.

- The microstructural damage due to the fully reversed fatigue was different at the two test temperatures used in this study. At room temperature transverse cracks occurred early in life. After saturation of the transverse cracks, bundle debonds were initiated. With further cycling, the debonds branched off to cause interlaminar delaminations. Delaminations first occurred at the interfaces of the outer plies. As cycling continued, delaminations were seen at the interfaces of interior plies. Isolated warp bundles debonded along the edge of the coupons fractured due to bundle buckling at the

onset of failure. Failure at room temperature was a result of massive debonding and bundle buckling in the remaining intact plies. At elevated temperature, bundle debonds and bundle fractures occurred early, along the face and edge of the coupons. These events had minimal influence on the modulus since they occurred at the surface. Subsequent to bundles debonding, transverse cracks were initiated. These cracks showed higher concentrations near the edge of the coupon. Delaminations at the outermost laminae occurred as failure was approached. Progressively, the delaminations grew through the thickness. Failure at elevated temperature was a result of resin shear failure, bundle debonding, and bundle fracture due to buckling in the remaining intact plies.

• Residual compressive strength tests were conducted on specimens at various stages of damage. However, the level of damage induced by mechanical cycling was more easily measured by stiffness degradation. The room temperature coupons appeared more tolerant of damage than the elevated temperature coupons. For example, at room temperature and 1 percent stiffness loss, the coupon retained 95 percent of its initial compressive strength. At elevated temperature and 1 percent stiffness loss, the coupon retained only 75 percent of its initial compressive strength.

These experimental findings helped guide the development of the fatigue life model which is high-lighted in the next section.

5.3 General Discussion of the Damage Model

The damage model quantitatively measures the degree of damage by establishing a functional relationship between the current stiffness and the damage state of the laminate. The damage evolution law employs a power law relationship to model the damage rate as a function of the multiaxial cyclic stress environment and the current level of damage. The critical damage, which defines the level of damage at the time of failure, is dependent on the multiaxial cyclic stress environment and the temperature. Characterization of the model in

respect to the T650-35/PMR15 (0/90) weave was achieved by the utilization of the fully reversed fatigue life data and stiffness data. After defining the model and comparing it with data the following conclusions were realized:

- For the current material system, the damage was found to have a constant degradation rate dependent on the maximum cyclic stress and cyclic mean stress. Because the stiffness data showed the degradation rates to be independent of temperature, the room and elevated temperature data were pooled in the characterization of the damage rate equation. However, the critical damage state was dependent on the both the cyclic stress level and temperature.

- Comparisons between predicted life and S-N data indicated good agreement between the model and experiment at 22 °C (72 °F) and 316 °C (600 °F). The predictive capabilities of the model were further substantiated by comparing the model to fully reversed fatigue data produced at an intermediate temperature of 204 °C (400 °F). The agreement at this intermediate temperature was good concerning both the modulus behavior and cycles to failure.

This fatigue life model represents a nascent effort in developing a predictive method for this class of composites. The following section points to further work that would strengthen the capability of the model.

5.4 Future Directions

To achieve a fuller understanding of the physical characteristics of the woven material, experimentation under various conditions is required. This includes the influence of mean stress, temperature, and moisture on the life and microstructural behavior. Because structural components experience off-axis and multiaxial stresses, it is recommended that off-axis uniaxial tests as well as multiaxial fatigue tests be conducted. Also, to simulate true component conditions thermomechanical fatigue (TMF) needs to be explored. TMF involves simultaneously cycling both load and temperature. In-phase loading dictates that

load and temperature reach there maximums and minimums simultaneously. In contrast, out-of-phase conditions dictate that the load is at its maximum while the temperature is at its minimum, and for the minimum load the temperature is at its maximum. In the future, both cyclic regimens should be examined carefully.

Due to the many assumptions incorporated into the damage model, the above experimental recommendations can be used to verify the model. Also, expansion of the phenomenological model can be explored concerning moisture and TMF. Variables can be added to the damage rate equation or critical damage term which allow model characterization for the above conditions. These variables can be functions of maximum temperature, temperature range as well as moisture content. However, before such implementations are made a thorough experimental data base is required.

REFERENCES

Adam, T., Gathercole, N.,Harris, B., and Reiter H. , "The Fatigue Behavior of a CFRP Laminate Subjected to Load Cycling at R-Ratios From Pure Tension to Pure Compression," *Proceedings 8th International Conference on Composite Materials*, S.W. Tsai and G.S. Springer, editors, Society for the Advancement of Materials and Process Engineering, Covina, Ca., Vol. 4, No. 38, 1991, pp. 1–7.

Agarwal, B.D. and Broutman, L.J., *Analysis and Performance of Fiber Composites*, John Wiley & Sons, Inc., New York, 1990.

The Annual Book of ASTM Standards, Vol. 15.03, 1994.

Arnold, S.M. and Kruch, S., "Differential Continuum Damage Mechanics Models for Creep and Fatigue of Unidirectional Metal Matrix Composites," NASA TM–105213, November, 1991.

Bishop, S.M., "Strength and Failure of Woven Carbon-Fiber Reinforced Plastics for High Performance Applications," *Textile Structural Composites*, T.W. Chou and F.K. Ko, editors, Elsevier Science Publishing Company Inc., New York, NY, 1989.

Bowles, K.J., Roberts, G.D., and Kamvouris, J.E., "Long Term Isothermal Aging Effects on Carbon Fabric Reinforced PMR-15 Composites: Compression Strength," NASA TM-107129, March, 1996.

Broek, D., *Elementary Engineering Fracture Mechanics*, Martinus Nijhoff, Hingham, Massachusetts, 1986.

Broutman, I.J. and Sahu, H., "A New Theory to Predict Cumulative Fatigue Damage in Fiber Glass Reinforced Plastics," *Composite Materials: Testing and Design*, ASTM STP 497, H.T. Corten, editor, 1972, pp. 170–188.

Burr, S.T. and Morris, D.H., "Characterization of Two-Dimensional Braided Composites Subject to Static and Fatigue Loading," *Mechanics of Textile Composites Conference*, Hampton, Virginia, Dec. 6-8, 1994.

Butkis, L.M., "Thermomechanical Fatigue Behavior of a Silicon Carbide Fiber-Reinforced Calcium Aluminasilicate Glass-Ceramic Matrix Composite," Master's Thesis, The University of Michigan, 1991.

Cantwell, W.J. and Morton J., "The Significance of Damage and Defects and Their Detection in Composite Materials: A Review," *Journal of Strain Analysis*, Vol. 27, No. 1, 1992.

Carlson, R.L. and Kardomateas, G.A., *An Introduction to Fatigue in Metals and Composites*, Chapman & Halls, New York, NY, 1996.

Castelli, M.G., Bartolotta, P.A., and Ellis, J.R., "Thermomechanical Testing of High Temperature Composites: Thermomechanical Fatigue (TMF) Behavior of SiC (SCS-6)/Ti-15-3," *Composite Materials Testing and Design (Tenth Volume)*, ASTM STP 1120, Glenn C. Grimes, editor, American Testing and Materials, Philadelphia, 1992, pp. 70–86.

Chou, P.C. and Croman, R., "Degradation and Sudden-Death Models of Fatigue of Graphite/Epoxy Composites," *Proceedings 5th Conference on Composite Materials: Testing and Design*, ASTM STP 674, S.W. Tsai, editor, 1979, pp. 431–454.

Curtis, P.T. and Bishop, S.M., "Assessment of the Potential of Woven Carbon Fiber Reinforced Plastics for High Performance Use," *Composites*, Vol. 15, 1984, pp. 259–265.

Curtis, P.T. and Moore, B.B., "A Comparison of the Fatigue Performance of Woven and Non-Woven CFRP Laminates," RAE Technical Report 85059, June, 1985.

Duffy, S.F. and Gyekenyesi, J.P., "Reliability and Life Prediction of Ceramic Composite Structures at Elevated Temperatures," *High Temperature Mechanical Behavior of Ceramic Composites*, Nair S.V. and Jakus K., editors, Butterworth-Heinemann, Newton, MA, 1995.

Fujii, T. and Amijima, S., "Microscopic Fatigue Processes in a Plain-Weave Glass-Fiber Composite," *Composite Science and Technology*, Vol. 49, 1993, pp. 327–333.

Golfman, Y., "Ultrasonic Non-Destructive Method to Determine Modulus of Elasticity of Turbine Blades," *SAMPE Journal*, Vol. 29, No. 4, July/August, 1993.

Gyekenyesi, A.L., "Crack Development in Cross-Ply Laminates Under Uniaxial Tension," NASA CR-195464, January, 1996.

Gyekenyesi, A.L., Castelli, M.G., Ellis, J.R., and Burke, C.S., "A Study of Elevated Temperature Testing Techniques for the Fatigue Behavior of PMCs: Application to T650-35/AMB21," NASA TM–106927, July, 1995.

Hahn, H.T., "Fatigue of Composites: Environmental Effects," *Proceedings of the 3rd Riso International Symposium on Metallurgy and Materials Science*, September 6-10, 1982, Roskilde, Denmark.

Hahn, H. and Kim, R.Y., "Proof Testing of Composite Materials," *Journal of Composite Materials*, Vol. 9, 1975, pp. 297–311.

Hahn, H. and Kim, R.Y., "Fatigue Behavior of Composite Laminates," *Journal of Composite Materials*, Vol. 10, 1976, pp. 150–180.

Hahn, H. and Lorenzo, L., "Fatigue Failure Mechanisms in Composite Laminates," *Advances in Fracture Research (Fracture 84)*, Vol. 1, Oxford and New York, Pergamon Press, 1986, pp. 549–568.

Harris, C.E. and Gates, T.S., editors, *High Temperature Effects on Polymeric Composites*, ASTM STP 1174, 1993.

Hemann, J.H., Bowles, K.J., Kautz, H., and Cavano, P., "Transply Crack Density Detection by Acousto-Ultrasonics," NASA TM–100224, 1987.

Highsmith, A., "Damage Induced Stress Redistribution in Composite Laminates," Ph.D. Dissertation, Virginia Polytechnic Institute and State University, December, 1984.

Hwang, W. and Han, K.S., "Fatigue of Composite Materials: Damage Model and Life Prediction," *Composite Materials: Fatigue and Fracture, Second Volume*, ASTM STP 1012, P.A. Lagace, editor, American Society for Testing and Materials, Philadelphia, 1989, pp. 87–102.

Ishikawa, T. and Chou, T.W., "Elastic Behavior of woven Hybrid Composites," *Journal of Composite Materials*, Vol. 16, 1982, pp. 2–19.

Jamison, R.D., "On the Interrelationship Between Fiber Fracture and Ply Cracking in Graphite/Epoxy Laminates," *Composite Materials: Fatigue and Fracture*, ASTM STP 907, H.T. Hahn, editor, American Society for Testing and Materials, 1986, pp. 252–273.

Ju, J.W., "Damage Mechanics of Composite Materials: Constitutive Modeling and Computational Algorithms," Final technical report prepared for the Air Force Office of Scientific Research, Washington, DC, 1991.

Kedward, K.T. and Whitney, J.M., *Delaware Composites Design Encyclopedia-Volume 5: Design Studies*, Technomic Publishing Company, Inc., Lancaster, PA, 1990.

Krajcinovic, D., "Damage Mechanics," *Mechanic of Materials*, Vol. 8, 1989, pp. 117–197.

Lee, J., "Damage Development, Property Degradation and Fatigue Life Prediction in Composite Laminates," Ph.D. Dissertation, Northwestern University, August, 1988.

Lemaitre, J. and Chaboche, J.L., *Mechanics of Solid Materials*, Cambridge University Press, New York, NY, 1990.

Liu, B.Y., "Fatigue and Damage Tolerance Analysis of Composite Laminates: Stiffness Loss, Damage Modeling, and Life Predictions," Master's Thesis, Dept. of Mech. Engineering, McGill University, Montreal, Quebec, Canada, Feb., 1992.

Liu, B and Lessard, L.B., "Fatigue and Damage Tolerance Analysis of Composite Laminates: Stiffness Loss, Damage Modeling, and Life Prediction," *Composite Science and Technology*, Vol. 51, 1994, pp. 43–51.

Meskini, A., "Prediction of Stiffness Degradation of Composite Laminates Under Fatigue Loading," Ph.D. Dissertation, George Washington University, Washington, D.C., May, 1986.

Mitrovic, M. and Carman, G.P., "Effect of Fatigue Damage in Woven Composites on Thermo-Mechanical Properties and Residual Compressive Strength," *Journal of Composite Materials*, Vol. 30, 1996, pp. 164–188.

Naik, N.K., Shembekar, P.S., and Hosur, M.V., "Failure Behavior of Woven Fabric Composites," *Journal of Composite Technology and Research*, Vol. 13, 1991, pp. 107–116.

O'Brien, T.K., "An Evaluation of Stiffness Reduction as a Damage Parameter and Criterion for Fatigue Failure in Composite Materials," Ph.D. Dissertation, Virginia Polytechnic Institute and State University, October, 1978.

Odom, E.M. and Adams, D.F., "Stiffness Reductions During Tensile Fatigue Testing of Graphite/Epoxy Angle Ply Laminates," Contract No. NAS1–16557, NASA Langley Research Center, November, 1982.

Pipes, R.B. and Pagano, N.J., "Interlaminar Stresses in Composite Laminates Under Uniform Axial Extension," *Journal of Composite Materials*, Vol. 4, 1970, pp. 538–548.

Poursartip, A., Ashby, M.F., and Beaumont, P.W.R., "Damage Accumulation During Fatigue of Composites," *Proceedings of International Conference on Composite Materials IV*, Tokyo, 1982.

Reifsnider, K.L., "The Critical Element Model: A Modeling Philosophy," *Engineering Fracture Mechanics*, Vol. 25, 1986, pp. 739–749.

Riefsnider, K.L. and Stinchcomb, W.W., "A Critical-Element Model of the Residual Strength and Life of Fatigue Loaded Composite Coupons," *Composite Materials: Fatigue and Fracture*, ASTM STP 907, 1986, pp. 298–313.

Reifsnider, K.L., editor, *Fatigue of Composite Materials*, Elsevier Science Publishers B.V., Amsterdam, The Netherlands, 1991.

Rotem, A. and Nelson, H.G., "Failure of a Laminated Composite Under Tension-Compression Fatigue Loading," *Composite Science and Technology*, Vol. 36, 1989, pp. 45–62.

Rybicki, E.F., " Approximate Three-Dimensional Solutions for Symmetric Laminates Under In-Plane Loading," *Journal of Composites Materials*, Vol. 5, 1971, p. 354.

Ryder, J.T. and Walker, E.K., "The Effect of Compressive Loading on the Fatigue Lifetime of Graphite/Epoxy Laminates," AFML-TR-79-4128, Final Technical Report, October, 1979.

Shulte, K., "Fatigue Damage Development in Carbon Fiber Reinforced composites," *International Conference on Fatigue of Engineering Materials and Structures*, Vol. 2, Sheffield, England, Sept. 15–19, 1986, pp. 321–327.

Schulte, K., Reese, E. and Chou, T.W., "Fatigue Behavior and Damage Development in Woven Fabric Composites," *Proceedings of the 6th International Conference on Composite Materials ICCM & ECCM Second European Conference on Composite Materials*, Vol. 4, Imperial College of Science and Materials, London, UK, July 20–24, 1987.

Shultz, R.W. and Reifsnider, K.L., "Fatigue of Composites Laminates Under Mixed Tension-Compression Loading," *Proceedings of 2nd International Conference on Fatigue and Fatigue Thresholds*, C.J. Beevers, editor, EMAS, Warley, UK, 1984, pp.1102–12.

Springer, G.S., editor, *Environmental Effects on Composite Materials*, Technomic Publishing Company, Inc., Westport, CT, 1981.

Stinchcomb, W.W. and Bakis, C.E., "Fatigue Behavior of Composite Laminates," in *Fatigue of Composite Materials*, K.L. Reifsnider, editor, Elsevier Science Publishers B.V., Amsterdam, The Netherlands, 1991.

Stinchcomb, W.W. and Reifsnider, K.L., "Fatigue Damage Mechanisms in Composite Materials: A Review," *Fatigue Mechanisms*, ASTM STP 675, J.T. Fong, editor, 1979, p. 762.

Tai, N.H., Ma, C.C.M. and Wu, S.H., "Fatigue Behavior of Carbon Fiber/Peek Laminate Composites," *Composites*, Vol. 26, Number 8, 1995.

Talreja, R., *Fatigue of Composite Materials*, Technomic Publishing Company, Inc., Lancaster, Pennsylvania, 1987.

Vinson, J.R., editor, *Advanced Composite Materials-Environmental Effects*, ASTM STP 658, 1977.

Wang, S.S. and Chim, E.S.M., "Fatigue Damage and Degradation in Random Short-Fiber SMC Composites," *Journal of Composite Materials*, Vol. 17, 1983, p. 114.

Wang, A.S.D., Chou, P.C. and Lei, C.S., "Cumulative Damage Model for Advanced Composite Materials: Phase II," Final Report, AFWAL-TR-84-4004, March, 1984.

Weinberger, R.A., Somoroff, A.R., and Riley, B.L., "US Navy Certification of Composite Wings for the F-18 and Advanced Harrier Aircraft," *AIAA Journal*, Vol. 17,1977, p. 477.

Worthem, D.W., "Flat Tensile Specimen Design for Advanced Composites," NASA CR-185261, Nov., 1990.

Wyoming Test Fixtures Inc. Product Catalog No. 104, 421 South 19th Street, Laramie, Wyoming 82070, Tel. (307) 742-8641.

Yang, J.N., "Fatigue and Residual Strength Degradation for Graphite/Epoxy Composites Under Tension-Compression Cyclic Loadings," *Journal of Composite Materials*, Vol. 12, Jan., 1978, p. 19.

Yang, J.N. and Liu, M.D., "Residual Strength Degradation Model and Theory of Periodic Proof Tests for Graphite/Epoxy Laminates," *Journal of Composite Materials*, Vol. 11, April, 1977, p. 176.

Yang, J.N., Yang, S.H., and Jones, D.L, "A Stiffness-Based Statistical Model for Predicting the Fatigue Life of Graphite/Epoxy Laminates," *Journal of Composites Technology & Research*, Vol. 11, No. 4, Winter, 1989, pp. 129–134.

Ye, L., "On Fatigue Damage Accumulation and Material Degradation in Composite Materials," *Composite Science and Technology*, Vol. 36, 1989, pp. 339-350.

REPORT DOCUMENTATION PAGE

Public reporting burden for this collection of information is estimated to average 1 hour per response, including the time for reviewing instructions, searching existing data sources, gathering and maintaining the data needed, and completing and reviewing the collection of information. Send comments regarding this burden estimate or any other aspect of this collection of information, including suggestions for reducing this burden, to Washington Headquarters Services, Directorate for Information Operations and Reports, 1215 Jefferson Davis Highway, Suite 1204, Arlington, VA 22202-4302, and to the Office of Management and Budget, Paperwork Reduction Project (0704-0188), Washington, DC 20503.

1. AGENCY USE ONLY (Leave blank)	2. REPORT DATE March 1998	3. REPORT TYPE AND DATES COVERED Final Contractor Report

4. TITLE AND SUBTITLE

Isothermal Fatigue, Damage Accumulation, and Life Prediction of a Woven PMC

5. FUNDING NUMBERS

WU–523–22–13–00
NAG3–1543

6. AUTHOR(S)

Andrew L. Gyekenyesi

7. PERFORMING ORGANIZATION NAME(S) AND ADDRESS(ES)

Cleveland State University
Cleveland, Ohio 44115

8. PERFORMING ORGANIZATION REPORT NUMBER

E–10971

9. SPONSORING/MONITORING AGENCY NAME(S) AND ADDRESS(ES)

National Aeronautics and Space Administration
Lewis Research Center
Cleveland, Ohio 44135–3191

10. SPONSORING/MONITORING AGENCY REPORT NUMBER

NASA CR—1998-206593

11. SUPPLEMENTARY NOTES

This report was submitted as a dissertation in partial fulfillment of the requirements for the degree of Doctor of Engineering, Cleveland State University, Cleveland, Ohio 44225 in 1997. Project Manager, John R. Ellis, Structures and Acoustics Division, NASA Lewis Research Center, organization code 5920, (216) 433–3340.

12a. DISTRIBUTION/AVAILABILITY STATEMENT

Unclassified - Unlimited
Subject Category: 24   Distribution: Standard

This publication is available from the NASA Center for AeroSpace Information, (301) 621–0390.

12b. DISTRIBUTION CODE

13. ABSTRACT (Maximum 200 words)

This dissertation focuses on the characterization of the fully reversed fatigue behavior exhibited by a carbon fiber/polyimide resin, woven laminate at room and elevated temperatures. Nondestructive video edge view microscopy and destructive sectioning techniques were used to study the microscopic damage mechanisms that evolved. The residual elastic stiffness was monitored and recorded throughout the fatigue life of the coupon. In addition, residual compressive strength tests were conducted on fatigue coupons with various degrees of damage as quantified by stiffness reduction. Experimental results indicated that the monotonic tensile properties were only minimally influenced by temperature, while the monotonic compressive and fully reversed fatigue properties displayed noticeable reductions due to the elevated temperature. The stiffness degradation, as a function of cycles, consisted of three stages; a short-lived high degradation period, a constant degradation rate segment composing the majority of the life, and a final stage demonstrating an increasing rate of degradation up to failure. Concerning the residual compressive strength tests at room and elevated temperatures, the elevated temperature coupons appeared much more sensitive to damage. At elevated temperatures, coupons experienced a much larger loss in compressive strength when compared to room temperature coupons with equivalent damage. The fatigue damage accumulation law proposed for the model incorporates a scalar representation for damage, but admits a multiaxial, anisotropic evolutionary law. The model predicts the current damage (as quantified by residual stiffness) and remnant life of a composite that has undergone a known load at temperature. The damage/life model is dependent on the applied multiaxial stress state as well as temperature. Comparisons between the model and data showed good predictive capabilities concerning stiffness degradation and cycles to failure.

14. SUBJECT TERMS

Fatigue; Damage accumulation; Compression; Elevated temperature; Polymer matrix composites; Test methods; Stiffness degradation; Residual strength; Continuum mechanics; Life prediction

15. NUMBER OF PAGES
164

16. PRICE CODE
A08

17. SECURITY CLASSIFICATION OF REPORT	18. SECURITY CLASSIFICATION OF THIS PAGE	19. SECURITY CLASSIFICATION OF ABSTRACT	20. LIMITATION OF ABSTRACT
Unclassified	Unclassified	Unclassified	